Incorporation of Hydride Nuclear Fuels in Commercial Light Water Reactors

by

Kurt Amir Terrani

A dissertation submitted in partial satisfaction of the
requirements for the degree of
Doctor of Philosophy

in

Engineering-Nuclear Engineering

in the

Graduate Division
of the
University of California, Berkeley

Committee in charge:

Professor Donald Olander, Chair
Professor A Brian Wirth
Professor Ronald Gronsky

Fall 2010

Incorporation of Hydride Nuclear Fuels in Commercial Light Water Reactors

Copyright 2010
by
Kurt Amir Terrani

Abstract

Incorporation of Hydride Nuclear Fuels in Commercial Light Water Reactors

by

Kurt Amir Terrani
Doctor of Philosophy in Engineering-Nuclear Engineering

University of California, Berkeley

Professor Donald Olander, Chair

This dissertation intends to examine basic materials properties, identify optimized fabrication techniques, model behavior under relevant environments, and experimentally quantify kinetic phenomena associated with hydride nuclear fuels. Hydride fuels have been examined extensively for application in light water reactors (LWR) from the neutronics and thermal hydraulic standpoints, the benefits of this fuel have been underscored through such studies. This manuscript provides the background for understanding materials aspects of hydride fuel incorporation in LWR environments.

The proposed LWR hydride fuel concept consists of uranium-zirconium hydride pellets clad in Zircaloy and bonded with a lead-bismuth alloy. The fuel material consists of metallic uranium particles dispersed in a zirconium hydride matrix, although thorium and/or other minor actinide hydride matrices could be utilized. The eutectic lead-bismuth alloy is liquid during reactor operating temperatures and replaces the conventionally-used helium gas in the fuel-cladding gap, thereby providing a thermal conductivity increase of two orders of magnitude. Initially uranium-thorium-zirconium hydrides were fabricated and extensively characterized. This provided detailed insight into fuel properties and the influence of fabrication methodology. A modeling approach was undertaken to examine hydride fuel behavior under steady-state and transient-power conditions in a typical LWR. This study outlined the operating parameters and fuel-response characteristics under various reactor operating conditions that support the feasibility of hydride fuel incorporation into LWRs. The kinetics of hydrogen release from the fuel, associated with one of the most severe accident scenarios, was investigated in detail. Mechanisms were identified for hydrogen desorption from and adsorption on zirconium hydride and the rates associated with each process were quantified. Hydrogen diffusivity in the thorium-zirconium hydride matrix, which is one of the critical parameters affecting fabrication and in-reactor fuel behavior, was experimentally determined by the means of incoherent quasielastic neutron scattering. Finally experiments were conducted to examine compatibility of hydride fuel with Zircaloy cladding when bonded by liquid-metal. A thin oxide grown on the surface of the cladding coupled with liquid metal was tentatively identified as adequate

to limit hydrogen transport form the fuel to the cladding. Recognizing the necessity of a shift from laboratory scale experiments to more relevant fuel-operating environments, an irradiation experiment was conceived to examine the liquid-metal-bonded LWR hydride fuel concept.

To Effie, Asdolla, and Leila

Contents

List of Figures

List of Tables

Acknowledgments

I feel privileged to have worked under the supervision of my advisor, Professor Donald Olander. I have benefitted greatly from his concise, objective, and insightful advice based on his tremendous experience in the nuclear fuels field. I am also extremely grateful to my other advisor, Professor Brian Wirth, who has supported and motivated me through every step of my graduate studies. His advice will have a lasting impact throughout my professional career and I will be forever grateful for his mentorship.

I am also very indebted to Dr. Mehdi Balooch who has worked with me side-by-side and from whom I have gained great knowledge in the experimental materials science field. I would also like to acknowledge Professors Ronald Gronsky, Eric Norman, and Thomas Devine, from whose courses I have learned a great deal. Each have been very kind and have helped me considerably throughout my graduate career and offered great advice.

I also had the pleasure to work with Dr. Mitchell Meyer of Idaho National Laboratory. I have benefitted continuously from his pragmatic advice and his critical role in enabling much of the experimental effort presented in this manuscript. Finally, I take this opportunity to show my deepest gratitude to my parents, Effie and Asdolla, and my sister Leila, for their continuous support and encouragement.

Chapter 1

Introduction

The United States is on the brink of a historic transformation of energy generation, transportation and distribution. This transformation is in response to the prospects of severe climate change as well as to economic and global security threats, both of which are brought on by excessive fossil fuel consumption. In the U.S., almost all of the energy needs for the transportation sector, as well as roughly 70% of electricity production are met through consumption of fossil fuels [2]. Although fossil fuels will play a significant role in addressing the nation's energy needs in the near future, deployment of other technologies that could reduce this country's dependence on fossil resources is necessary. The ever-increasing national population and the emergence of electric-vehicle technologies present an opportunity to begin transforming the transportation energy structure and to implement significant changes in the electricity production industry. Correspondingly, the expected surge in electricity demand needs to be met with carbon-free and commercially-feasible technologies.

Nuclear energy is currently second to coal as one of the cheapest sources of electricity production in the United States [2]. Stable fuel prices, exceptional operating efficiency, and large baseload capacity make nuclear power the most valuable of all electricity sources. Figure1.1 shows the evolution in the fraction of nuclear electricity generated and the operating efficiency of nuclear plants in the past decades. Nuclear electricity generation is a carbon-free process. Even when taking into account carbon emission during construction, the carbon equivalent of nuclear power is less than that of solar energy [43]. Although no carbon-control legislation is currently in place, the cost of carbon regulation will only enhance the economics of nuclear power plants. In addition, the long experience in utilizing nuclear resources places their viability and efficacy far ahead of the other renewable concepts currently being explored.

Unlike permanent nuclear reactor core components, nuclear fuel-element design has been constantly evolving in response to demands for higher operating efficiency, higher power level, and enhanced reliability. Although many decades have passed since construction of the first nuclear reactors, commercial nuclear fuel still consists of uranium dioxide clad in a zirconium-based alloy. Meanwhile, the design and performance of this fuel has experienced major improvements achieved by a combination of enhanced processing of the fuel, cladding-alloy optimization, and improved neutronic and thermal hydraulic design. In the meantime the impact of fuel on utility's operational efficiency and revenue, intrinsic character of the fuel fabrication industry, and the culture amongst the nuclear power operators have all been essential factors in laying the ground for more advance fuel designs. Nuclear fuel constitutes approximately a quarter of the variable cost of power generation [31]; a fraction much lower than is the case for fossil plants. A reliable fuel that can be operated at higher power and be pushed to higher burnups significantly enhances the profit outlook during the power cycle. On the other hand, defective fuel can bring upon significant costs to the operator. The maintenance costs during a refueling outage, not accounting for the cost of replacement power and margins lost from off-line units, are close to $1M per day for a typical light water reactor (LWR) [51]. Relatively low marginal cost of the fuel

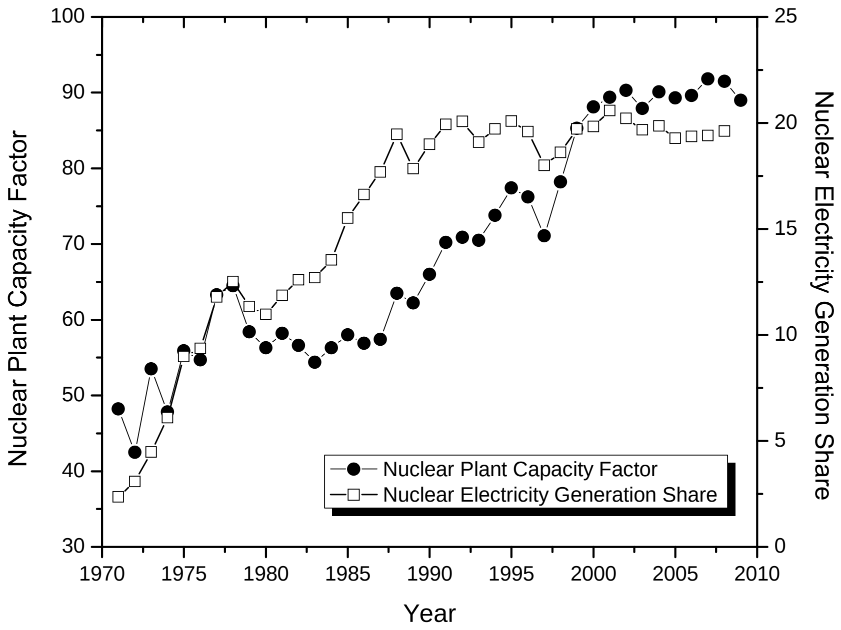

Figure 1.1: Evolution of electricity generation capacity and operating efficiency of nuclear plants [31, 14].

and the strong feedback on the operating profits that are associated with fuel performance emphasize why investments in more advanced fuel with higher power density and enhanced reliability are extremely cost-effective and heavily pursued by nuclear utilities. The fuel fabrication industry typically consists of divisions within the nuclear vendors or spun-off units of these organizations. The fuel manufacturing process is very versatile; fuel production for both domestic and foreign pressurized-water reactor (PWR) and boiling-water reactor (BWR) designs typically occur within a single fuel-fabrication facility is typical. In the United States, the fuel manufacturer rarely owns the uranium inventory (75% of the fuel cost) and fabricates full fuel bundles directly from UF_6 gas [31]. The uranium is purchased by the utility from the enrichment facility with a customized enrichment specification and is supplied to the fuel manufacturer. The fuel fabrication process is also highly adaptable and is tailored to meet the reactor operator's specific needs. These characteristics of the fuel manufacturing industry are designed to accommodate the rapidly evolving nature of commercial nuclear fuel and provide flexibility to the utilities so that they enhance their operation capabilities by making moderate changes in fuel design. Finally, the willingness of the utilities to share their experiences and best practices, as well as the unparalleled operational efficiency of this sector, provide the momentum for further enhancing fuel designs.

Evolution in fuel design and deployment will continue in the current and Gen III+

light-water reactors. This trajectory also underscores the potential for introduction of advanced fuels. Advanced fuels potentially offer better performance by replacing uranium oxide fuels in the current and upcoming fleet of nuclear reactors. The barriers for transforming current fuel materials and designs are much smaller than those facing the combination of both new reactors and new fuels. In other words, the timelines and costs associated with introduction of new fuel types that could be directly deployed into the current LWRs are much smaller than that of new reactor design and development. Still, however, fuel development and qualification timelines are long; on the order of 20+ years. The underlying challenge in fuel development is the need for research to provide solutions and create opportunities that simultaneously address the requirements and motivations of nuclear-plant vendors, regulators, and reactor operators. Effectively driving nuclear technology forward through advanced fuel development requires interdisciplinary meshing of fields such as materials science, neutronics, thermal hydraulics, safety, and non-proliferation.

Recognizing the opportunity and the challenge, an attempt has been made to lay the foundation for critical examination of a promising fuel concept: LWR hydride fuels. Throughout this manuscript, the basic aspects of materials properties, performance, and behavior associated with incorporation of hydride fuels in LWRs are investigated. The research was focused on materials processing, characterization, performance modeling and compatibility issues of such fuels in LWR environments.

Crawford et al. [16] have studied the fuel development and qualification process and have provided a framework for the steps involved, which include the following: fuel candidate selection; concept definition and feasibility; fuel design improvement and evaluation; and finally fuel qualification and demonstration. Taking advantage of this framework, the activities described in this manuscript fall within a useful context that corresponds to one of the major phases identified in the fuel development process. The research presented here supports the concept definition and feasibility phase. Meanwhile the background and stepping stones have been provided to effectively transition into the next phase; fuel design improvement and evaluation.

1.1 Overview

Hydride fuels generally consist of fissile/fertile materials that are mixed into a metal hydride matrix. Historically the most common type of hydride fuel consists of metallic uranium particles dispersed in a zirconium hydride matrix, U-ZrH_x. This fuel was originally developed for the Systems for Nuclear Auxiliary Power (SNAP) program by National Aeronautics and Space Administration (NASA) starting in the late 1950s [27]. A nuclear-reactor-powered satellite (SNAP-10) was launched into space in 1965. During the same period, General Atomics developed and commissioned its TRIGA type research reactors with a similar hydride fuel. Both of the above reactor designs took advantage of the benefits gained from combining the moderator and fuel;

Table 1.1: Properties and operating parameters for various hydride- and oxide-fueled reactors [11, 50, 27, 32].

Reactor Type	SNAP-8	Romanian TRIGA	LWR Hydride	LWR oxide
Fuel Type	U-$ZrH_{1.6}$	U-$ZrH_{1.6}$	U-$ZrH_{1.6}$	UO_2
U-235 enrichment %	93	19.7	12.5	< 5
weight fraction U	0.10	0.45	0.45	-
U/Zr atomic ratio	0.04	0.32	0.32	-
Fuel density [g/cm^3]	6.1	7.3	7.3	10.5
Uranium Density [cm^{-3}]	1.4×10^{21}	5.7×10^{21}	5.7×10^{21}	24.4×10^{21}
Clad diameter [cm]	1.4	1.3	1.2	1.2
Clad material	Hastelloy	Incoloy 800	Zircaloy	Zircaloy
Coolant	NaK	Water	Water	Water
Inlet coolant temperature [ºC]	520	60	290	290
Max fuel temperature [ºC]	620	820	550	1450
Power [MWt]	0.6	14	4000	3800
Average LHR [W/cm]	77	350	175	175
Max LHR [W/cm]	140	800	375	375

most notably the high power density and the strong negative fuel-temperature reactivity feedback. Hydride fuels, however, have rarely been used for high-power applications such as the oxide fuels utilized in commercial nuclear power plants. The fuel designs and performance parameters of oxide and hydride fuels are compared in Table 1.1. The SNAP-8 [50] and the Romanian TRIGA [11] were (are) high-power versions of the SNAP and TRIGA-type reactors.

Due to the advantages of hydride fuel over uranium oxide, a new type of hydride fuel explicitly designed for commercial Light Water Reactors (LWR) is proposed [32]. Recent research activities on potential improvements accrued by incorporation of hydride instead of oxide fuels in LWRs were initially supported through U.S. Department of Energy's (DOE) NERI [32]. This work was performed in a partnership between the University of California, Berkeley, the Massachusetts Institute of Technology, and the Westinghouse Electric Company. The research covered various disciplines including neutronics, thermal hydraulics, fuel-rod vibration and mechanical integrity, and economics. A fuel rod design was proposed that consisted of $U_{0.31}ZrH_{1.6}$ fuel clad in Zircaloy with a liquid eutectic lead-bismuth (Bi-44wt%Pb) or a lead-tin-bismuth (Pb-33wt%Sn-33wt%Bi) alloy filling the fuel-cladding gap [47].

This chapter provides a brief review of improvement possibilities in the performance of PWRs and BWRs by fueling them with hydride rather than oxide fuels. In the following sections of this chapter, basic properties of hydride fuel and irradiation performance characteristics are discussed based on available literature and historic data.

1.2 Incentives for using hydride fuel in LWRs

From 2002 to 2008 the University of California, Berkeley Department of Nuclear Engineering, in collaboration with MIT, Westinghouse and Argonne National Laboratory with funding from NERI projects, investigated improvement possibilities in the design and performance of commercial PWRs and BWRs that are fueled with hydride instead of oxide fuel. An extensive description of the pros and cons of hydride fuel versus oxide fuel for LWR identified in these studies is given in the special issue of Nuclear Engineering & Design that summarizes these projects [32]. Briefly, it was found that hydride fuel can safely operate in PWRs and BWRs having comparable or higher power density relative to typical oxide-fueled LWRs. The most promising applications of hydride fuel identified are the following.

1.2.1 PWRs

Use of hydride fuel enables more effective recycling of plutonium in PWRs than is possible with oxide fuel by virtue of a number of unique features of hydride fuel; reduced inventory of U-238 and increased inventory of hydrogen. As a result, the hydride-fueled cores can fission approximately 64% of the loaded plutonium at the first recycle (Figure 1.2); this is nearly double the fractional transmutation of plutonium attainable with MOX fuel [24, 23]. In the optimized PWR hydride fuel, plutonium is incorporated as a separate PuH_2 phase making a PuH_2 -$ZrH_{1.6}$ fuel. Plutonium, as opposed to uranium, forms a stable hydride with similar crystal structure to that of zirconium hydride.

Moreover, the hydride fuel PuH_2 -$ZrH_{1.6}$ allows multi-recycling of plutonium in PWRs, which, in principle can occur an unlimited number of times when uniformly loaded in all fuel assemblies in the core. The number of recycles feasible with MOX fuel is limited because the coolant void coefficient becomes positive after the first or second recycle. This unique feature of hydride fuels is due to the incorporation of a significant fraction of the hydrogen moderator in the fuel, thereby reducing the effect of spectrum hardening due to coolant voiding accidents; therefore, the large-void-reactivity coefficient remains negative. It was additionally found that hydride fuels allow recycling of Pu+Np at least 6 times before a positive void reactivity feedback becomes the limiting factor. The number of recycles for the entire TRU stream is limited by positive large void reactivity feedback to 2 or 3 times. Figure 1.2 shows the TRU destruction capability for such cores with different constituents taking into account the reactivity coefficient constraints.

1.2.2 BWRs

Oxide fueled BWRs typically require approximately 1.5 times higher coolant-to-fuel volume ratio than their PWR counterparts. This is due to the relatively large coolant

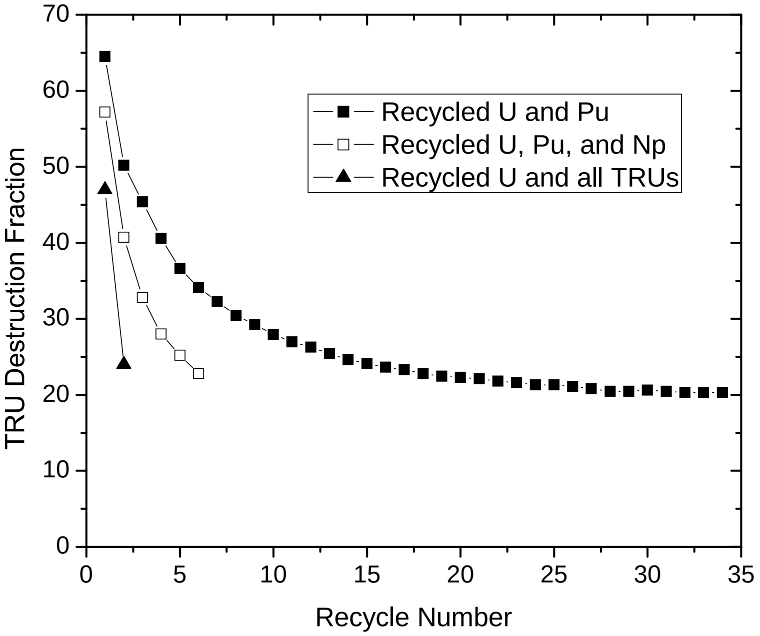

Figure 1.2: Destruction fraction of TRU in hydride fuel as a function of recycle number [24].

void fraction at the upper part of the core. Incorporating part of the moderator within the fuel, as in the case for hydride fuels, enables elimination of the dedicated moderator volumes within the fuel bundle, including water rods, partial length fuel rods, and water gaps not required for control-blade insertion. This enables a higher fuel rod loading per unit core volume while reducing the heterogeneity of BWR fuel bundles, thus achieving flatter pin-by-pin power distribution. Meanwhile the cooled fuel rod surface area, as well as the coolant flow cross-section area per unit of core volume are significantly increased. Figure 1.3 is one example of a simplified BWR bundle design utilizing hydride fuels. Non-uniform enrichment is still desirable due to the presence of water gaps when control blades are removed. The net result is up to 40% increase in the core power density and a reduction of the cost-of-electricity.

Selected design and performance characteristics of several hydride fueled bundles were compared with those of oxide fueled bundles when the power is not constrained by the coolant pressure drop. For identical minimum critical heat flux ratio (MCHFR) and coolant exit quality (χ_{out}), the best-performing hydride bundle design can safely operate at ~40% higher power than the reference 10×10 oxide fuel bundle, both bundles occupying the same volume. The corresponding peak hydride fuel-rod temperature is only 563 °C, significantly lower than the steady-state limit of 750 °C. The coolant pressure drop at this power level needs to be approximately twice of the nominal value (0.147 MPa); this could challenge the structural integrity of the core components [20].

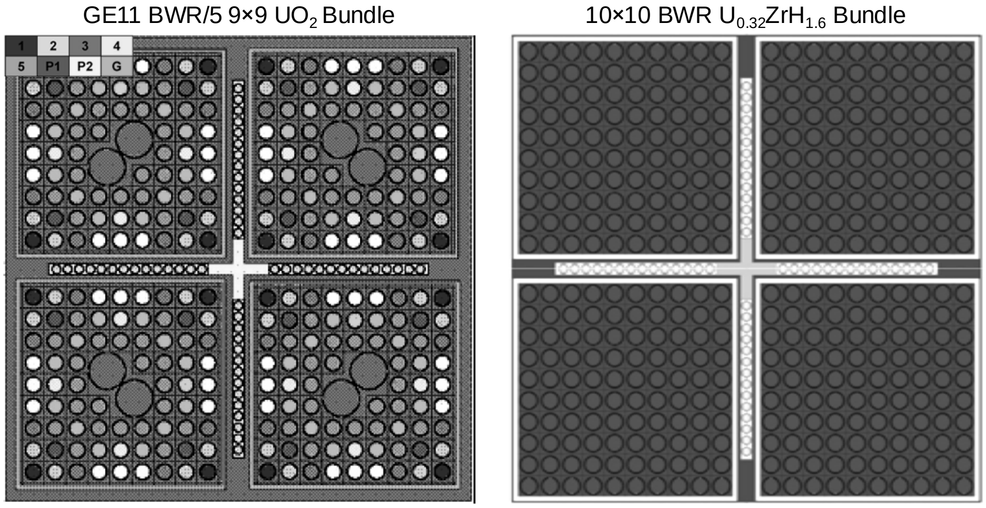

Figure 1.3: Left: GE11 BWR/5 oxide fuel bundle; 1-5, P1/P2, and G denote various enrichments, partial fuel length and gadolinia containing rods, respectively. Right: Uniform-enrichment BWR hydride fuel bundle [20].

1.3 As-fabricated hydride fuel properties

1.3.1 Fuel processing and structure

Hydride fuel fabrication is discussed in detail in Chapter 2 and involves alloying the metallic components of the fuel followed by a hydriding procedure. For U-Zr hydride fuel the uranium-zirconium alloys with the desired compositions are generally made by arc melting the metal components. The metal alloy then undergoes bulk hydriding at high temperatures (~ 700-900 °C) where the zirconium hydride phase is formed. The final fuel consists of metallic α-uranium phase (orthorhombic – *Cmcm* space group) and the δ-zirconium hydride (cubic - $Fm\bar{3}m$ space group) phase with H/Zr = 1.6. A typical microstructure is shown in Figure 1.4; the metallic uranium particles appear as the dark regions surrounded by the bright zirconium hydride matrix. Historically HEU (high-enriched uranium) was used in hydride fuel fabrication and the weight fraction of the metallic component was ~10wt%. Following termination of the SNAP program and subsequent inception of the Reduced Enrichment for Research and Test Reactor (RERTR) program, LEU (low-enriched-uranium) TRIGA fuel was introduced. The proposed LWR fuel contains the same weight fraction of uranium (45wt%) as current TRIGA fuel.

Uranium hydride (UH_3) is unstable at fuel processing temperatures and the hydrogen selectively reacts with zirconium atoms in the metallic solid solution. The hydrogen-to-zirconium ratio of the hydride matrix is selectively processed by control of temperature and hydrogen gas pressure. Other types of hydride fuels that have re-

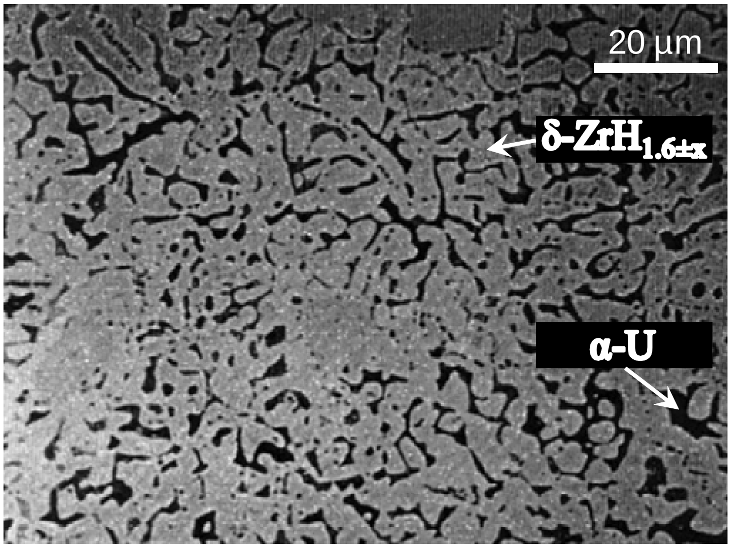

Figure 1.4: Optical micrograph of the microstructure of U(45wt%)-$ZrH_{1.6}$ fuel. Uranium appears as the dark phase [12].

ceived considerable attention during the past decade are uranium-thorium-zirconium hydrides [74, 67]. U-Th-Zr fuel fabrication is the subject of Chapter 2 and involves similar steps as described earlier.

1.3.2 Thermal properties

U-Zr hydride fuels have ~5 times higher thermal conductivity than the oxide type. This greatly reduces the temperature gradient across the pellet, offering a high-power-density fuel that operates at much lower temperatures compared to oxide fuel. Typical fuel-centerline temperatures during oxide fuel operation in light-water reactors is around 1000-1400 °C compared to 500-600 °C for hydride fuels. The temperature distribution across a hydride fuel pellet under steady state and transient conditions is discussed in Chapter 3. Figure 1.5 shows the thermal conductivity as a function of temperature for various unirradiated hydride fuels as well as oxide fuel at different burnups.

1.4 Irradiation effects on hydride fuels

1.4.1 Neutron flux and power distributions

Since the moderator is bound to the fuel, the neutron spectrum within the hydride fuel differs significantly from that in oxide fuels. In the latter, thermal neutrons, gener-

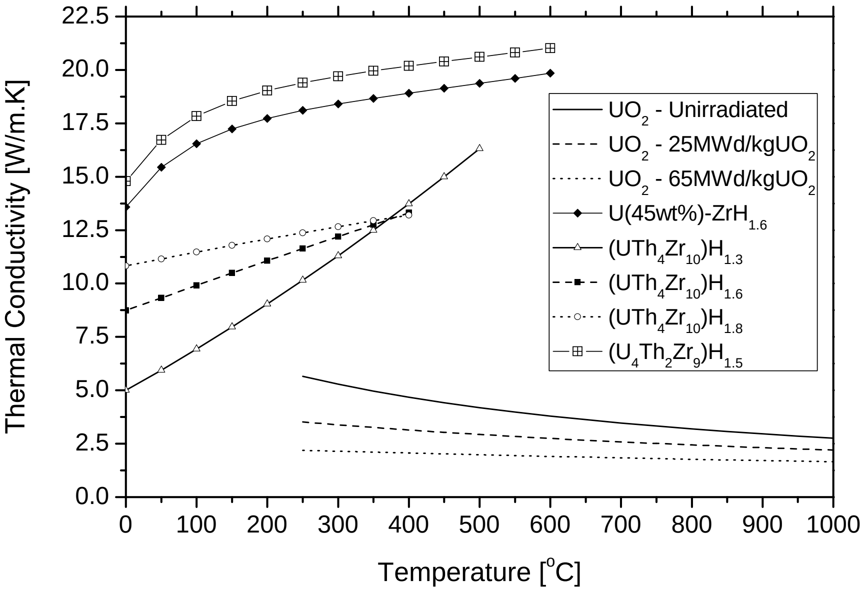

Figure 1.5: Thermal conductivity of various fuels as a function of temperature [66, 68, 72].

ated by moderation that takes place in the adjacent coolant, are present at high concentration at the periphery of the fuel; however their population decreases in the central regions. This causes deviations from a uniform power profile distribution and leads to phenomena such as the rim effect [59]. The presence of hydrogen within the fuel mitigates this issue because an almost uniform power density is maintained across the fuel radius. The fractional change from mean power across the radius of hydride and oxide fuels, conforming to the standard LWR geometries, is shown in Figure 1.6. The neutron spectra at different radial locations are also shown and are almost equivalent across the radius of a hydride fuel. The power profile and radial neutron spectra were calculated using a simple pin-cell model in MCNP (Monte Carlo N-Particle Transport Code), the details of which are discussed in Appendix A. The power density difference between the center and surface of the fuel pellet is ~11% and ~5% in fresh oxide and hydride fuels, respectively.

1.4.2 Swelling under irradiation

Most of the data describing swelling behavior of hydride fuels dates comes from the SNAP program [38]. An early-stage "offset" swelling observed prior to a burnup of 0.1% FIMA (fissions per initial metal atom) is very large in magnitude and strongly

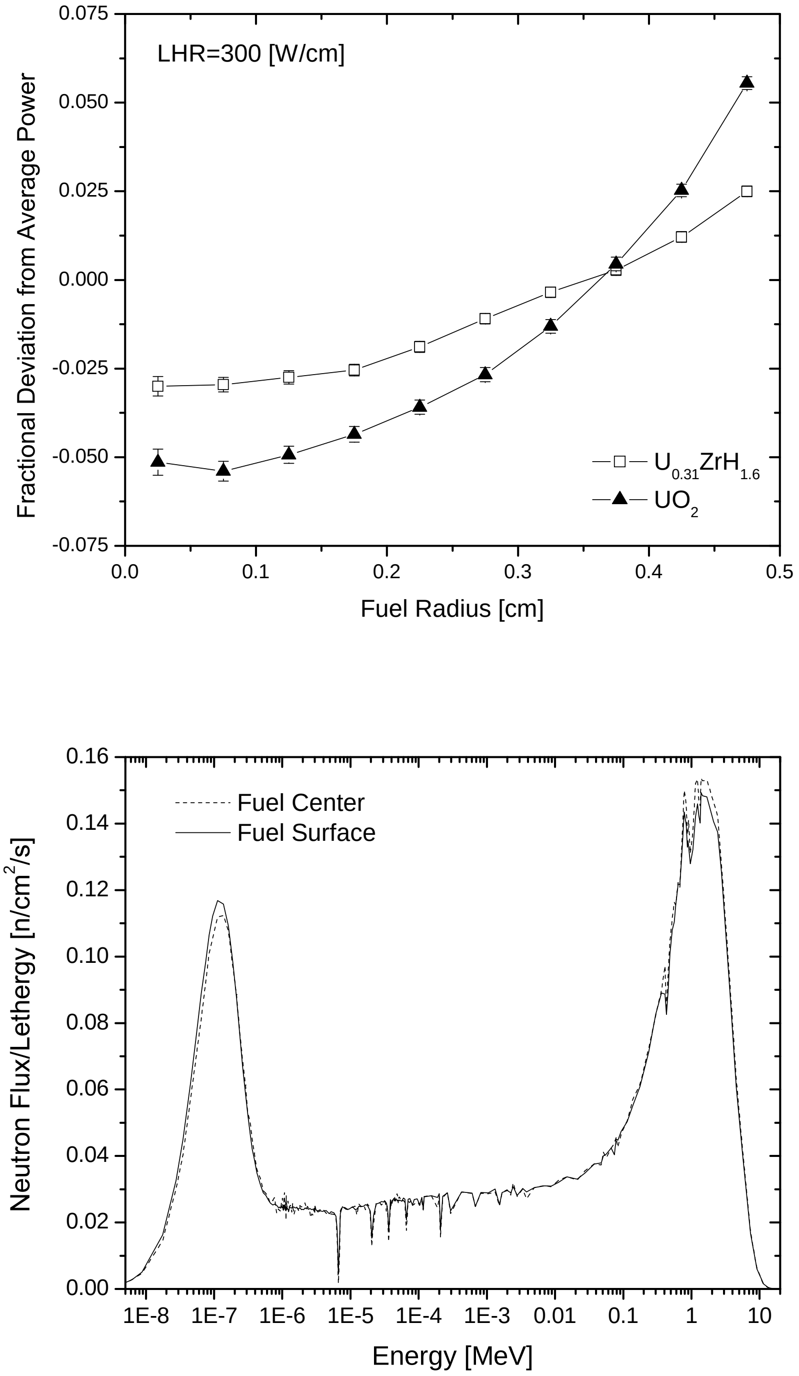

Figure 1.6: Top: MCNP calculation of the power density distribution across the fuel radius at LHR = 300 W/cm for oxide and hydride fuels. Bottom: Neutron flux spectra at the surface and center of a hydride fuel pellet.

temperature- and flux-dependent. The evolution of swelling as a function of burnup at various flux and temperature points is shown in Figure 1.7. The influence of flux (burnup rate) on the offset swelling rate is opposite of what is observed in fast-neutron-irradiated metals where the swelling rate (due to void growth) is directly proportional to square root of flux [46]. The observed offset swelling in the hydride fuel disappears at temperatures below 650 °C. Following this stage, a temperature- and flux- independent swelling of ~3% per %FIMA due to fission product formation is observed [47]; approximately three times larger than oxide fuel. SNAP tests utilized sophisticated experimental apparatus where the effects of flux and temperature on swelling rate were separated. Zirconium hydride (δ and ε phases) irradiated up to very large fluences showed negligible swelling [56]. In the SNAP studies offset swelling is attributed to voids that form near the uranium particles in the hydride matrix.

Swelling in hydride fuels is heterogeneous, while that in oxide fuel is homogeneous. Fission in hydride fuels is limited to the uranium particles that are distributed in the hydride matrix. The dominant portion of atomic displacements in the hydride matrix can be attributed to the high-energy fission fragments that escape from the uranium particles and cause significant damage at the particles periphery. Understanding the underlying mechanism of this phenomenon is necessary in order to assess the applicability of SNAP swelling data to predicting swelling behavior of the proposed LWR-type hydride fuel. The uranium particles in the SNAP fuel were ~ 5μm in diameter, ~40μm apart and 93% enriched in U-235. As shown in Figure 1.4, the U(45wt%)-$ZrH_{1.6}$ fuel consists of larger uranium particles placed much closer to one another. The U-235 enrichment in the proposed fuel is 12.5% which implies significantly less fission events within each uranium particle. These differences could greatly alter the extent and distribution of those local phenomena that collectively produce the macroscopically observed offset swelling.

1.4.3 Fission gas release

Fission gas release in uranium-zirconium hydride fuels has been investigated by two different experimental means. The first method involves in-pile irradiation experiments in which the sample temperature is controlled by electrical heating. Air or helium gases are used to sweep released gaseous species to a trap where gamma ray measurements are conducted. The results of these experiments represent the equilibrium ratio between the release rate and birth rate of the gaseous fission products. The observed release-to-birth-rate ratio is smaller than would be calculated due to recoil according to Equation 1.1[46]:

$$\frac{R}{B} = \overline{P}\left(\frac{S}{V}\right)\mu \tag{1.1}$$

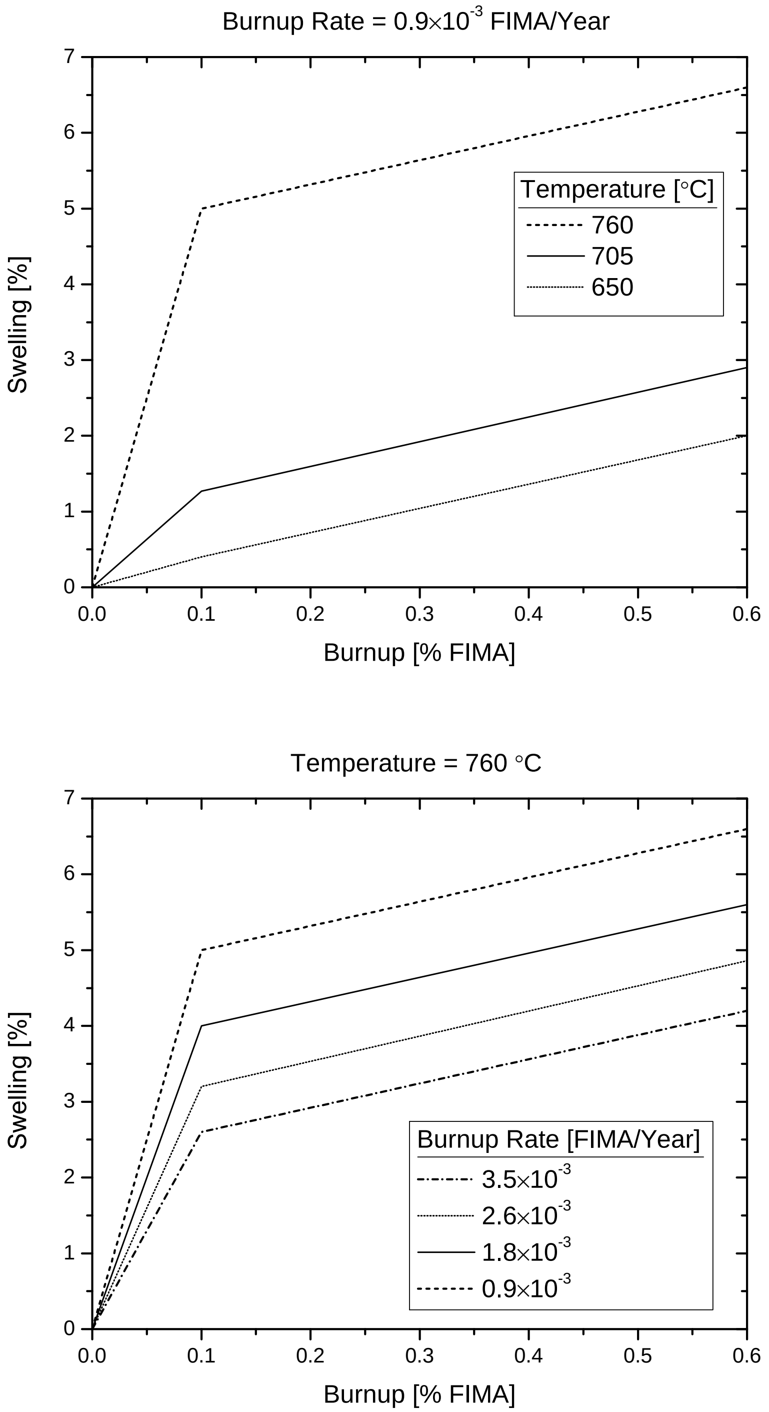

Figure 1.7: Swelling behavior of SNAP Fuel (U(10wt%)$ZrH_{1.6}$) as a function of burnup at various temperatures and burnup rates [47].

where $\overline{P}$, S, V, and μ are the escape probability (~0.25), fuel surface area, fuel volume, and the effective fission product range within the fuel, respectively. The GA specimens had an average surface- to-volume ratio of 0.39. The fission-product range within the fuel is that of 100 MeV fission products in uranium and zirconium hydride weighted by their respective volume fractions in the fuel and is ~9 μm. The calculated release-to-birth rate ratio could then be calculated as 8×10^{-4}, which is larger than that observed experimentally. At high temperatures it is possible to discern much lower release-to-birth rate ratios for high uranium content fuels. This observation refers back to the discussion regarding the microstructure of LEU fuel as opposed to the HEU fuel, where larger uranium particles effectively contain the fission products at high temperatures.

The second set of experiments involves post-irradiation annealing conducted for different durations and temperatures on samples that were initially irradiated up to $\sim2\times10^{13}$ fissions/cm^3 at room temperature. The results of the annealing experiments are the ratio of the total amount of fission gas released during the annealing (corrected for decay) to the total extent produced during the irradiation. Figure 1.8 shows the summary of all the data generated through both of the described procedures. All the data are from experiments conducted at General Atomics, with exception of 10 wt%U samples in the post-irradiation annealing experiments that are from the SNAP program [4]. Based on the available in-pile irradiation data, excellent fission gas retention is observed up to temperatures around 800ºC.

Interpretation of the post-irradiation annealing data is more challenging since different annealing times are compared to one another and detailed description of the SNAP (10wt%-U, 93% enriched U-235) experiments are unknown. The line in the figure is a conservative empirical correlation developed by General Atomics during the certification process of the TRIGA reactors [4]. Overall very good fission gas retention properties are observed up to temperatures significantly higher than expected to be experienced by the fuel during steady-state and transient conditions.

1.4.4 Irradiation effects on U-Th-Zr hydrides

Two uranium-thorium-zirconium hydrides, $(UThZr_4)H_{1.7}$ and $(UTh_2Zr_6)H_{1.3}$, were irradiated at the Japan Materials Testing Reactor (Japan) [75]. The irradiation temperature and uranium enrichment in the samples are unknown. The samples were investigated by electron microscopy and Vickers micro hardness testing at fluences of 7.4×10^{22}, 2.2×10^{23}, and 7.4×10^{23} n/m^2 of thermal neutrons corresponding to approximately 0.3, 0.9 and 3.1% of U-235 atom burnup. A maximum of ~15% decrease in hardness was observed at highest dose. No change in dimensions, mass, and microstructure of the samples were observed. The good irradiation performance of the fuels were attributed to their fine microstructure where the phase boundaries provided strong sinks for the produced defects.

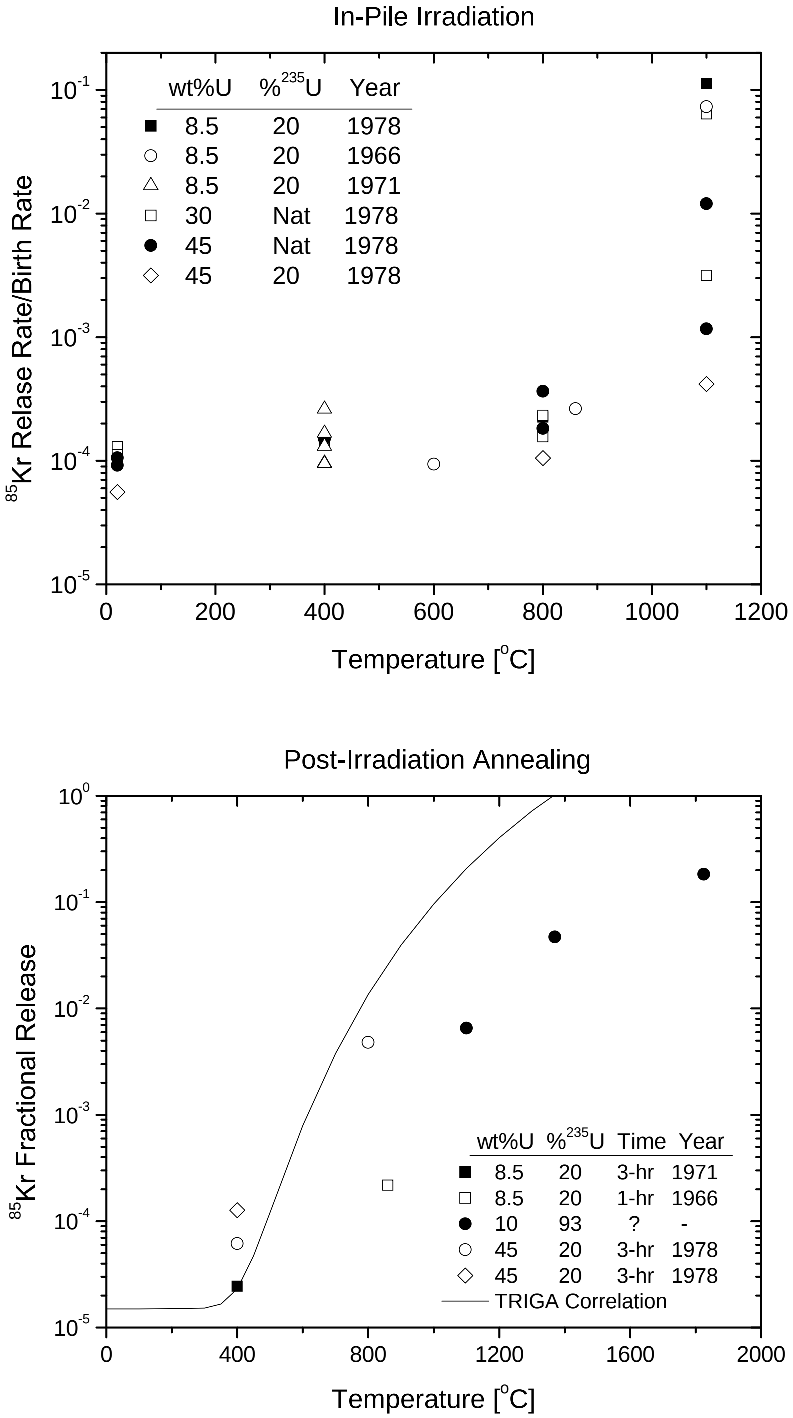

Figure 1.8: Top: Fission-gas-release to birth-rate ratio as a function of temperature. Bottom: Fractional fission-gas release as a function of post-irradiation annealing temperature [4].

1.5 Liquid-metal gap filler

A eutectic lead-bismuth alloy (Bi-44wt%Pb) that is liquid during reactor operation (126 °C melting point) is proposed as a substitute for the conventional helium-filled fuel-cladding gap. Thermal conductivity of the liquid-metal (LM) is approximately two orders of magnitude larger than that of helium gas, effectively eliminating the temperature drop across the gap during operation. This permits designing fuel rods with larger fuel-cladding gaps that can accommodate large swelling behavior of hydride fuels and eliminate pellet-cladding mechanical interaction (PCMI). Utilization of liquid metal also prevents formation of local hot spots on the cladding and the fuel (i.e. when the fuel is chipped or cladding is dented or ballooned). The fuel temperature is also reduced by eliminating the gap temperature drop. The liquid metal does not react with either oxide or hydride fuels or the coolant water and adequately wets the surface of both fuel and the Zircaloy cladding. Fabrication of full-length liquid-metal-bonded oxide fuels has been successfully demonstrated [73].

Another strong motivation for replacement of helium gas with LM in the gap is to protect the Zircaloy cladding from interactions with hydride fuel. Due to its superior neutronic and corrosion properties, Zircaloy is the cladding of choice for LWR fuel rods. Zirconium, however, is a strong getter of hydrogen and significantly embrittles upon reaction with hydrogen. It is therefore essential to limit hydrogen transport from the fuel to the cladding. Liquid-metal could be potentially utilized for this purpose and was preliminarily investigated [65]. Efficacy of LM to limit hydrogen transport from the fuel to the cladding is investigated in more detail in Chapter 6.

1.6 Organization

The chapters of this dissertation are organized as follows:

- Chapter 2 discusses the details of the experiments that were conducted during fabrication and characterization of uranium-thorium-zirconium hydrides.
- Chapter 3 discusses modeling of coupled heat conduction and hydrogen diffusion across the hydride fuel pellets under steady-state and transient reactor operating conditions. The magnitude of the various components of stress in the fuel pellet was also determined under these conditions.
- Chapter 4 focuses on determining the mechanisms and quantifying the rates of hydrogen desorption from and adsorption on zirconium hydride. The kinetics of hydrogen release from the fuel at high temperatures is of great practical importance during temperature excursions.
- Chapter 5 is dedicated to measurement of the hydrogen diffusion coefficient in thorium-zirconium hydride by means of incoherent quasi-elastic neutron scatter-

ing. The diffusivity of hydrogen in the hydride matrix is needed for fuel modeling codes such as the one discussed in Chapter 3.

- Chapter 6 outlines the results of the experimental work that was conducted to assess the compatibility of hydride fuels with Zircaloy cladding.
- Chapter 7 discusses the ongoing activities to fabricate and irradiate LWR hydride mini-fuel rods in order to make the necessary shift from laboratory scale experiments to more relevant environments.

Chapter 2

Fabrication and Characterization of Uranium-thorium-zirconium Hydrides

One of the preferred hydride-fueled pressurized-water reactor (PWR) core designs utilizes uranium-thorium-zirconium hydrides [24]. The design utilizes the thorium (Th/Zr ratio up to 0.25) along with IFBA (Integral Fuel Burnable Absorber) to achieve negative reactivity coefficients along the full fuel-burnup range. This eliminates the need for modifications in the core control system. Meanwhile utilization of U-Th-Zr hydrides has been proposed for transmutation of minor actinides in fast reactors [79]. In order to understand the properties and structures of these materials, two uranium-thorium-zirconium hydride fuels with gross compositions $(UTh_4Zr_{10})H_{1.9}$ and $(U_4Th_2Zr_9)H_{1.5}$ were processed and characterized.[1] $(UTh_4Zr_{10})H_{1.9}$ fuel is chosen as a benchmark based on previous work performed by Yamamoto et al. [74]. The $(U_4Th_2Zr_9)H_{1.5}$ fuel has been analyzed by Ganda and Greenspan [24].

Fuel fabrication involves arc melting and hydriding of the metal alloys. Subsequent characterization of the fuels has been performed using X-ray diffractometry, scanning electron microscopy, and transmission electron microscopy. Rietveld refinement of X-ray diffraction patterns confirmed formation of $ThZr_2H_7$, δ-$ZrH_{1.6}$ and α-U phases in both fuels. Scanning electron microscopy along with energy-dispersive X-ray spectroscopy provided information regarding the morphology and composition of the phases present in the microstructure of the fuels. Bright-field and phase-contrast imaging of the three phases present is done in the transmission electron microscope. Atomic force microscopy, along with nanoscale dynamic mechanical analysis of the fuel, have also been performed to map the elastic modulus of different phases across the microstructure. The results of the characterization techniques describe the detailed structure and morphology of the individual phases forming. The extent of formation of these phases depends on the composition of the fuel; however for the fuels that are subject of this work, thorium-zirconium hydride ($ThZr_2H_7$) is the matrix containing the evenly-dispersed zirconium hydride and uranium particles. The detailed composition of the fuels is presented in Table 2.1. Hydrogen-to-metal ratios were determined by weighing the samples prior and after the hydriding process. Volume fractions of each phase and the fuel density are all calculated based on the crystal structure of the three different phases in the fuel. During this calculation, densities of 19.05, 7.24, and 5.68 gr/cm^3 are used for α-U, $ThZr_2H_7$, and δ-$ZrH_{1.6}$ respectively. The calculated density for $(UTh_4Zr_{10})H_{1.9}$ is in good agreement with the experimental value of 7.55 gr/cm^3 determined by Tsuchiya et al. [68].

2.1 Fuel fabrication

Fuel fabrication was performed in Idaho National Laboratory's (INL) Materials and Fuels Complex (MFC) at Fuels and Applied Science Building (FASB). All the fabrica-

---

[1] Note that the use of parentheses in the notation $(UTh_4Zr_{10})H_{1.9}$, implies that the hydrogen-to-total metal (U+Th+Zr) ratio is 1.9; whereas the hydrogen-to-uranium, hydrogen-to-thorium, and hydrogen-to-zirconium ratios are 28.5:1, 28.5:4, and 28.5:10 respectively.

Table 2.1: Detailed composition of $(UTh_4Zr_{10})H_{1.9}$ and $(U_4Th_2Zr_9)H_{1.5}$.

Fuel	$(UTh_4Zr_{10})H_{1.93}$	$(U_4Th_2Zr_9)H_{1.55}$
H/M ratio	1.93	1.55
H/(Zr+Th) ratio	2.07	2.1
Vol% α-U	4.49	20.14
Vol% δ-$ZrH_{1.6}$	11.75	32.92
Vol% $ThZr_2H_7$	83.76	46.93
Fuel Density [$gr.cm^{-3}$]	7.57	9.1
at % U	2.16	10.81
at % Th	8.66	5.41
at % Zr	21.65	24.32
at % H	67.53	59.46
wt % U	11.28	42.14
wt % Th	43.99	20.54
wt % Zr	43.24	36.34
wt % H	1.48	0.97
Zr atom density [cm^{-3}]	2.17×10^{22}	2.18×10^{22}
H atom density [cm^{-3}]	6.76×10^{22}	5.34×10^{22}
U atom density [cm^{-3}]	2.17×10^{21}	9.71×10^{21}
Th atom density [cm^{-3}]	8.66×10^{21}	4.85×10^{21}

Table 2.2: Composition of U-Th-Zr alloys fabricated by arc melting.

Alloy	wt% U	wt% Th	wt% Zr
UTh_4Zr_{10}	11.5	44.7	43.9
$U_4Th_2Zr_9$	42	21.4	36.5

tion activities were performed either inside fume hoods with continuous air monitoring or negative pressure gloveboxes. The thorium metal was in form of plates of 99.5% purity, legacy material from 1971. Two alloys of uranium-thorium-zirconium were prepared by arc melting high-purity metal feedstock (>99%) in an argon glovebox under 4 ppm oxygen (Table 2.2). The alloys were subsequently casted in the shape of pins each weighing roughly around 30 grams. The metals were initially acid treated so that any impurities and scales on the surface were removed. Arc melting was done through the arc-lift process whereby the solidified buttons were turned and re-melted five times to achieve good homogeneity (Table 2.3). Between each melting step, the surface of the button was abraded to remove impurities. Arc melting resulted in melt temperatures in excess of 4000°C. The melt (single phase liquid) was then quickly solidified on a copper hearth, resulting in a quenched microstructure with dendrite formation.

Ternary phase diagrams of the U-Th-Zr system at equilibrium at temperatures of 550 °C, 800 °C and 1000 °C are shown in Figure 2.1 [3]. The three phases that have formed after arc melting are the following: γ phase that is a solid solution of uranium

Table 2.3: U-Th-Zr alloy arc melting process parameters.

Amperage	Polarity	Process	Output	Sample	Chiller setting
300	DC	Lift Arc	RMT Std.	Flip and remelt 5 times	20 °C

and zirconium with a body-centered cubic unit cell, α-thorium phase that has a face-centered cubic unit cell, and the δ-UZr_2 phase that is an ordered compound of uranium and zirconium with a hexagonal lattice.

One pin from each alloy was sectioned using a high speed saw with a diamond blade. The sample was continuously oscillated at an angle of ±15 while saw operation took place in the presence of water and oil mixture coolant inside the fumehood. The result was seven metal disks approximately 2.5 mm thick for each alloy. The alloy disks were then loaded into the inert glovebox environment and surface cleaned using a metal brush to remove some of the oxide formed during the sectioning operation. Disks were then loaded into an alumina boat and placed inside the hydriding furnace. A small piece of alumina was placed between metal disks in order to prevent diffusion bonding at high temperatures. The hydriding furnace consisted of a conventional tube furnace with a stainless steel tube. The hydriding furnace was located inside the argon glovebox and was connected to gas-manifold system on top of the glovebox. Atmospheric and vacuum-range pressure gauges were connected to the tubes leading to the furnace. Using the gas manifold, argon and hydrogen could be introduced inside the furnace at specified pressures or flow rates. A vacuum pump was also connected to the gas manifold to remove the gas inside the furnace. The furnace and gas manifold system is shown in Figure 2.2.

Outgassing of the metal disks took place in vacuum at 900 °C for 20 minutes in order to remove any volatile species present on the surface. Hydrogen gas was introduced into the tube furnace at pressure of approximately 1 atm (+1 inch of water). The alloys consumed the gas at this temperature very rapidly. However, the process soon saturated and hydriding became limited by diffusion of hydrogen into the metal disks. A characteristic diffusion length of hydrogen in zirconium hydride at this temperature and in one hour is ~1 mm. The temperature was then lowered from 900 °C to 500 °C over a 4-hour period in order to achieve higher hydrogen-to-metal ratios ($1.5 \rightarrow 2$) as was reported by Yamamoto et al. [74]. This was necessary since at higher temperatures (i.e. 900 °C) the equilibrium partial pressure of hydrogen with $H/M = 2$ exceeds 1 atm. It was therefore important to continue the hydriding at lower temperatures in order to increase the hydrogen concentration in the metal alloy.[2]

---

[2] The process just described for hydriding of the metal alloys is not the ideal optimized process. The ideal process would start by initially selecting a desired hydrogen-to-metal ratio for the overall alloy. Assuming that the hydrogen content of the uranium phase is negligible, the hydrogen stoichiometry in the zirconium hydride and thorium-zirconium hydride phases could then be determined. Hydrogen stoichiometries in the two hydride phases are not independent of one another; both are influenced by the hydrogen partial pressure in the gaseous phase in contact with the hydrides (hydrogen activity).

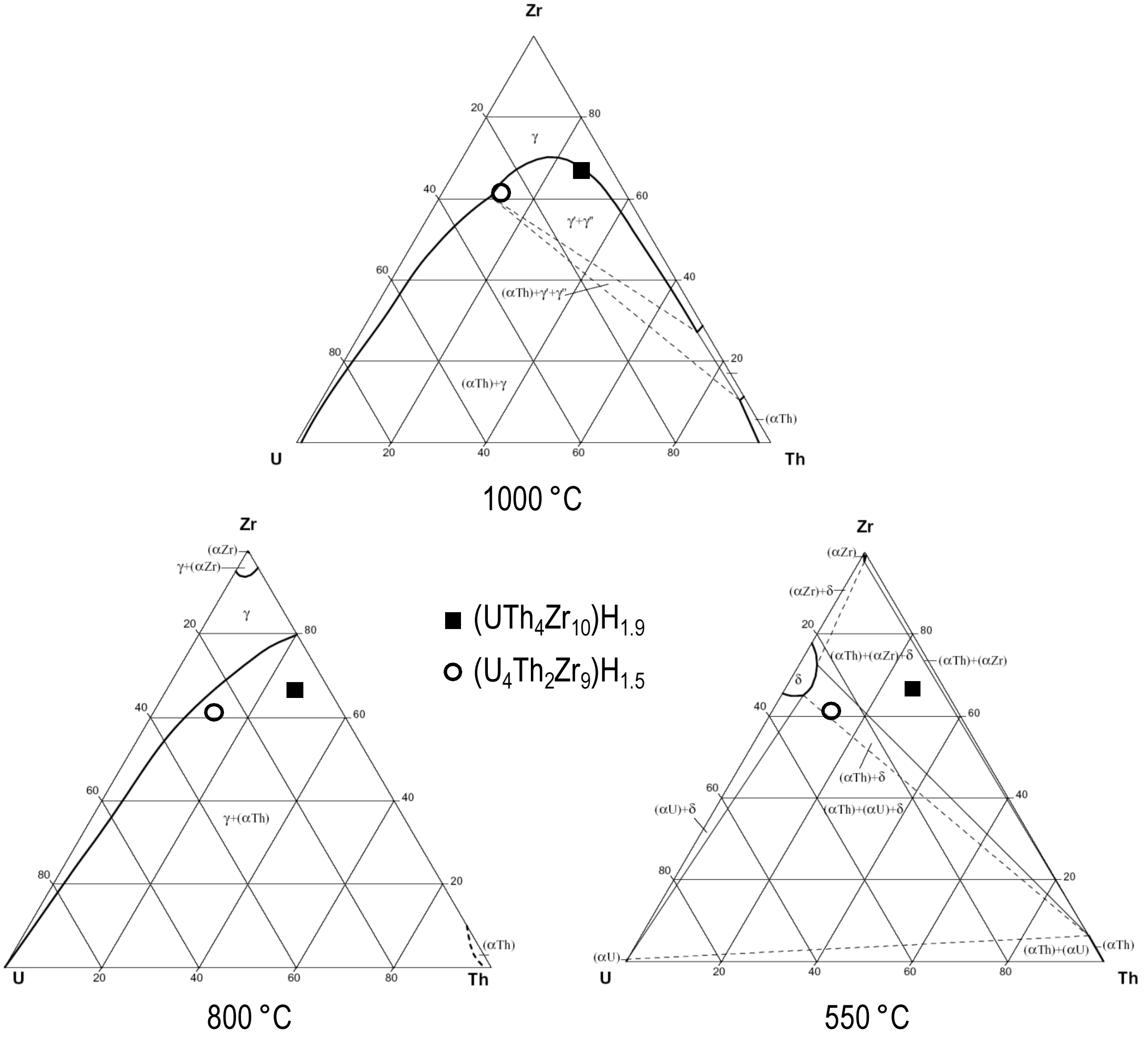

Figure 2.1: Uranium-thorium-zirconium ternary system at 550 °C, 800 °C and 1000 °C [3].

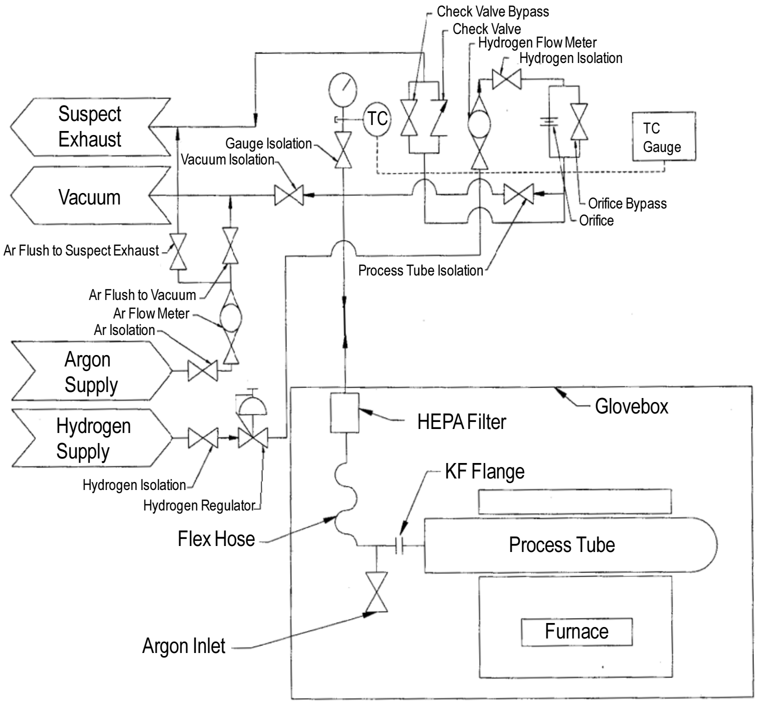

Figure 2.2: Schematic drawing of the hydrogen gas manifold and hydriding furnace.

Some of the disks experienced cracking after hydriding due to the large volume expansion associated with hydride formation. The extent of volume expansion is different based on the composition of the fuel. In order to estimate the extent of volume expansion in the two fuels, it is assumed that hydriding takes place at temperatures around 800 °C, where both of the metal alloys are in the two phase region of γ + α-thorium. The post-hydriding microstructure consists of the following three phases: α-U, $ThZr_2H_7$, and δ-$ZrH_{1.6}$. Table 2.4 includes the crystal structure and lattice pa-

---

Equilibrium temperature, hydrogen pressure and hydrogen concentration relationships for the two hydrides have been determined experimentally [70, 9]. This information could be utilized to determine the corresponding hydrogen stoichiometries of the two phases in equilibrium with each other and with the gas phase. After determining the desired hydrogen-to-metal ratio the process would start at high temperatures where the material is able to creep and accommodate the change in volume after hydriding. After completion of the hydriding process and upon cooling, both the temperature and hydrogen gas pressure should be lowered along the isochor line corresponding to this specific hydrogen-to-metal ratio. The advantage of this method is that a uniform hydrogen concentration is maintained across the material from the beginning of the process until the end. This is important since keeping the same hydrogen pressure and lowering the temperature increases the hydrogen concentration at the surface while the diffusion of hydrogen is greatly reduced, preventing the bulk of the material from achieving the same hydrogen-to-metal ratio as the surface. This would also give rise to severe stresses across the material since the surface and center of the material contain different quantities of hydrogen and therefore expand and contract respectively.

Table 2.4: Crystal structure and lattice parameter of phases present pre- and post-hydriding.

Phase	Space Group	Lattice Parameter [Å]	Ref.
β-Zr	$Im\bar{3}m$	3.5453	[18]
γ-U	$Im\bar{3}m$	3.4740	[17]
α-Th	$Fm\bar{3}m$	5.0836	[33]
δ-$ZrH_{1.6}$	$Fm\bar{3}m$	4.7770	[10]
$ThZr_2H_7$	$Fd\bar{3}m$	9.1549	[8]

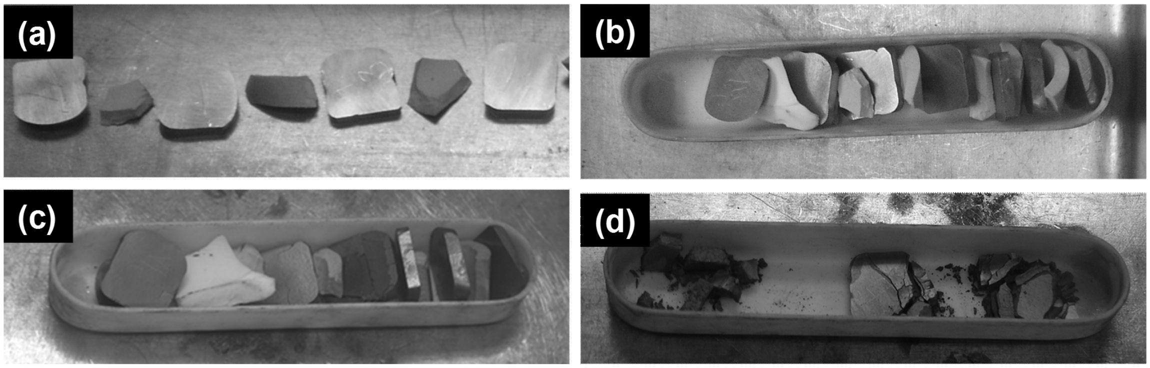

Figure 2.3: a) metal disks numbered and ready to be loaded into the alumina boat; b) metal disks and alumna chips loaded into the alumina boat; c) disks after hydriding; d) disks with severe cracking.

rameter of the starting elements and the phases present after hydriding. The lattice parameter of the γ phase can be estimated by applying Vegard's law based on the fuel composition. Using this information the extent of volume expansion due to hydriding is approximately 22% and 18% for the $(UTh_4Zr_{10})H_{1.9}$ and $(U_4Th_2Zr_9)H_{1.5}$ fuels, respectively.[3]

Figure 2.3 shows the metal disks prior to and after hydriding. It should also be pointed out that the condition of the disks kept at room temperature (especially in case of $(UTh_4Zr_{10})H_{1.9}$ worsened with time; some of the disks turned completely into a fine powder after a week. This is due to the significant residual stresses generated during the hydriding process and the subsequent cooling.

---

[3] This is in agreement with experimental observations since the $(UTh_4Zr_{10})H_{1.9}$ fuel experienced much more cracking.

Table 2.5: Lattice parameter of phases present in $(UTh_4Zr_{10})H_{1.9}$ and $(U_4Th_2Zr_9)H_{1.5}$ determined through Rietveld refinement.

Phase	Space Group	$(UTh_4Zr_{10})H_{1.9}$	$(U_4Th_2Zr_9)H_{1.5}$	Ref.
$ThZr_2H_7$	$Fd\bar{3}m$	a = 0.9186 nm	a = 0.9184 nm	a = 0.9154 nm [8]
δ-$ZrH_{1.6}$	$Fm\bar{3}m$	a = 0.4783 nm	a = 0.4762 nm	a = 0.4777 nm [10]
α-U	$Cmcm$	N/A	a = 0.2855 nm	a = 0.2854 nm [61]
		N/A	b = 0.5862 nm	b = 0.5869 nm
		N/A	c = 0.4956 nm	c = 0.4955 nm
ε-UH_3	$Pm\bar{3}n$	N/A	a = 0.6655 nm	a = 0.6627 nm [7]

2.2 Characterization

2.2.1 X-ray diffractometry (XRD)

XRD samples were prepared by depositing fuel powder on a low background silicon single-crystal sample holder using a slurry of powder and ethanol. Samples were also mixed with lanthanum hexaboride (LaB_6 SRM 660a) powder to be used as an internal standard during pattern refinement. High-resolution diffraction patterns were obtained using a Phillips PANalytical X'Pert Pro instrument with a Cu Kα source. Rietveld refinement was performed on the experimental patterns for the two fuels. Formation of α-U, $ThZr_2H_7$, and δ-$ZrH_{1.6}$, and minute amounts of ε-UH_3 was confirmed. Detailed results are presented in Table 2.5. The lattice parameter of α-U and ε-UH_3 phases could not be accurately determined for the $(UTh_4Zr_{10})H_{1.9}$ fuel due to the small volume fraction of these phases in this fuel. None of the following phases (accompanied by the corresponding space group) were detected in either of the fuels: ε-$ZrH_{1.8}$ ($I4/mmm$); δ-UH_3 ($Pm\bar{3}n$); δ-UZr_2 ($P6/mmm$); ZrH ($P42/n$); ThH_2 ($I4/mmm$); Th_4H_{15} ($I\bar{4}3d$).

The experimental powder patterns along with the results of the refinement fit are shown in Figure 2.4 for $(UTh_4Zr_{10})H_{1.9}$ and $(U_4Th_2Zr_9)H_{1.5}$ fuels. The structure factor calculations (SFC) were performed to match the experimental XRD intensities from different phases to the calculated volume fractions presented in Table 2.1. SFC was done specifically comparing the 022 type reflection from the $ThZr_2H_7$ phase and the 021 and 110 reflections from the α-U phase in the $(U_4Th_2Zr_9)H_{1.5}$ fuel. The intensity of the particular reflection is proportional to the square of the structure factor. Structure factor, F, is calculated as shown in Equation 2.1; where hkl, $u_nv_nw_n$, and f_n, are the plane indices for the specific reflection, atomic coordinates inside the lattice, and atomic scattering factor respectively. The basis vectors for thorium and zirconium in $ThZr_2H_7$ and uranium in α-U are known based on the structure and could be substituted for $u_nv_nw_n$ in Equation 2.1. The atomic scattering factors for all these elements are also tabulated as a function of angle in literature [22]. Scattering from hydrogen atoms was neglected in this calculation since the atomic scattering factor from this element is negligible com-

Table 2.6: Comparison of experimental peak intensities and structure factors.

Phase	Reflection	Experimental	SFC
$ThZr_2H_7$	022	1	1
α-U	021	0.75	0.79
	110	0.32	0.27

pared to that of the other high-Z elements present. Finally the square of the calculated structure factor is normalized by the fraction of the number of unit cells of each material per unit volume of the fuel (calculated from Table 2.1). The resulting calculated intensities shown in Table 2.6 agree well with the experimental values.

$$F_{hkl} = \sum_{1}^{N} f_n \exp\left[2\pi i \left(hu_n + kv_n + lw_n\right)\right] \tag{2.1}$$

Bartscher et al. [9, 8] have studied the $ThZr_2D_x$ system using neutron and X-ray diffraction and report the lattice parameter for the cubic unit cell as a function of different deuterium to metal ratios up to x = 6.3. Linear extrapolation of these results matches the determined lattice parameter for this phase (Table 2.5) to hydrogen stoichiometry of 7 (as in $ThZr_2H_7$) in both fuels. However, uncertainty is inherent in Bartscher data while extrapolation of this data introduces further error in what is estimated as the hydrogen stoichiometry for this phase in the fabricated fuels.

2.2.2 Scanning electron microscopy

Scanning electron microscopy (SEM) was performed on the metal alloys prior to and after hydriding. SEM on the metal alloy was performed using a FEI instrument model XL30-SFEG equipped with secondary and backscatter electron detectors and an EDAX Phoenix EDS (energy dispersive x-ray spectroscopy) system. The accelerating potential during operation was 20 kV. SEM specimens were prepared by embedding samples in epoxy and polishing to achieve very flat and smooth surfaces. No etching was done on the samples. A backscattering electron image of the microstructure of $U_4Th_2Zr_9$ alloy is shown in Figure 2.5. Three distinct phases embedded in two different microstructures are apparent. The rapid post-arc melting solidification has resulted in a very fine and non-equilibrium microstructure different than what is predicted by the ternary phase diagram at different temperatures in Figure 2.1. Figure 2.6 shows the energy dispersive X-ray spectra for the three specified regions (each corresponding to one of the phases present) in Figure 2.5(b). The contrast from the backscattered electron image correlates directly with the EDS spectra; where the bright phases are highly concentrated in uranium and thorium and depleted in zirconium and vice-versa. The limited focusing capability of the electron beam excited the atoms in the adjacent phases, besides the region of interest, and EDS spectra became contaminated with X-rays originating from the adjacent phases. Also the microstructure is that of cored dendritic

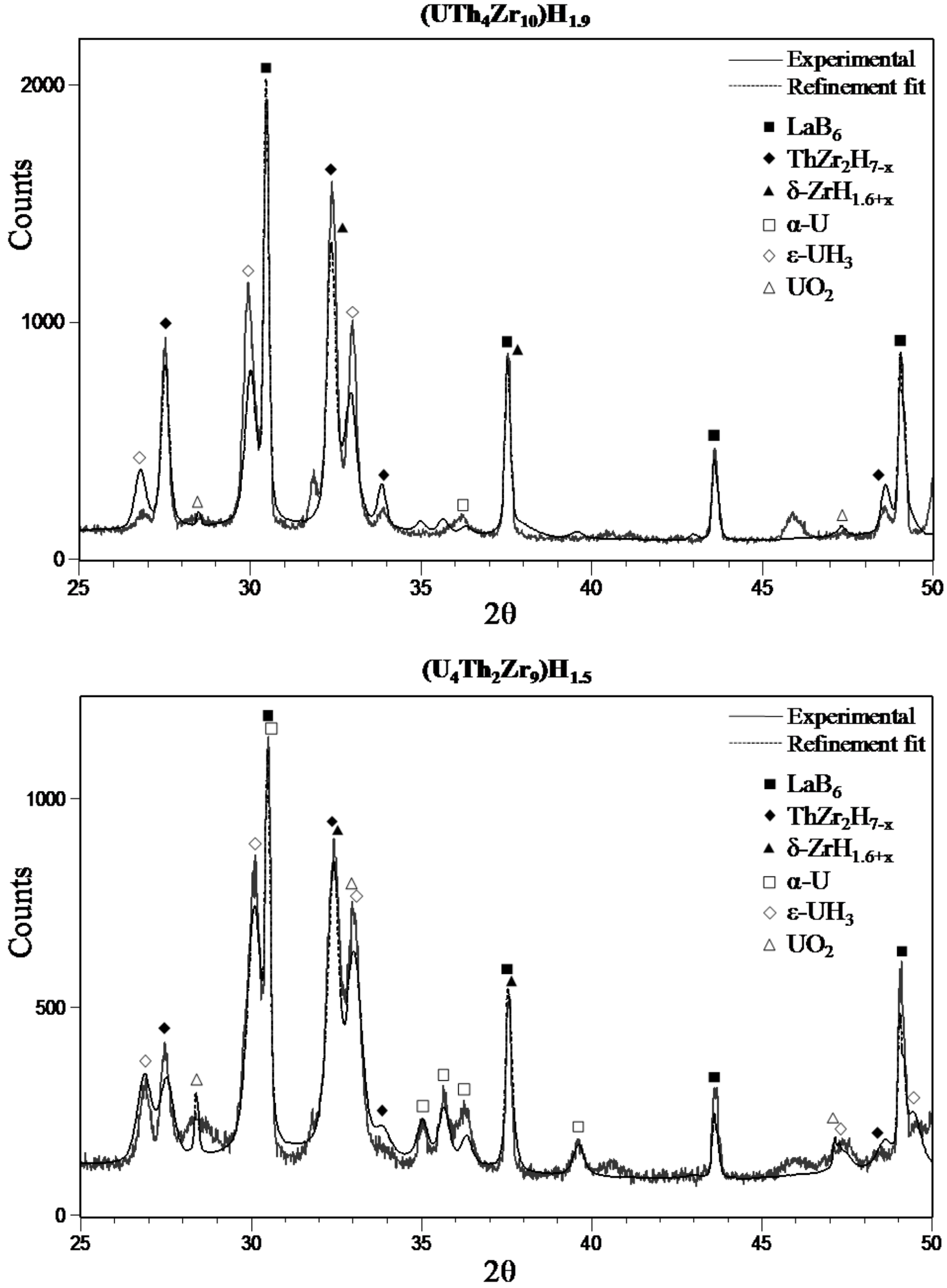

Figure 2.4: Powder x-ray diffraction patterns for (UTh$_4$Zr$_{10}$)H$_{1.9}$ and (U$_4$Th$_2$Zr$_9$)H$_{1.5}$ along with Rietveld-refinement fit.

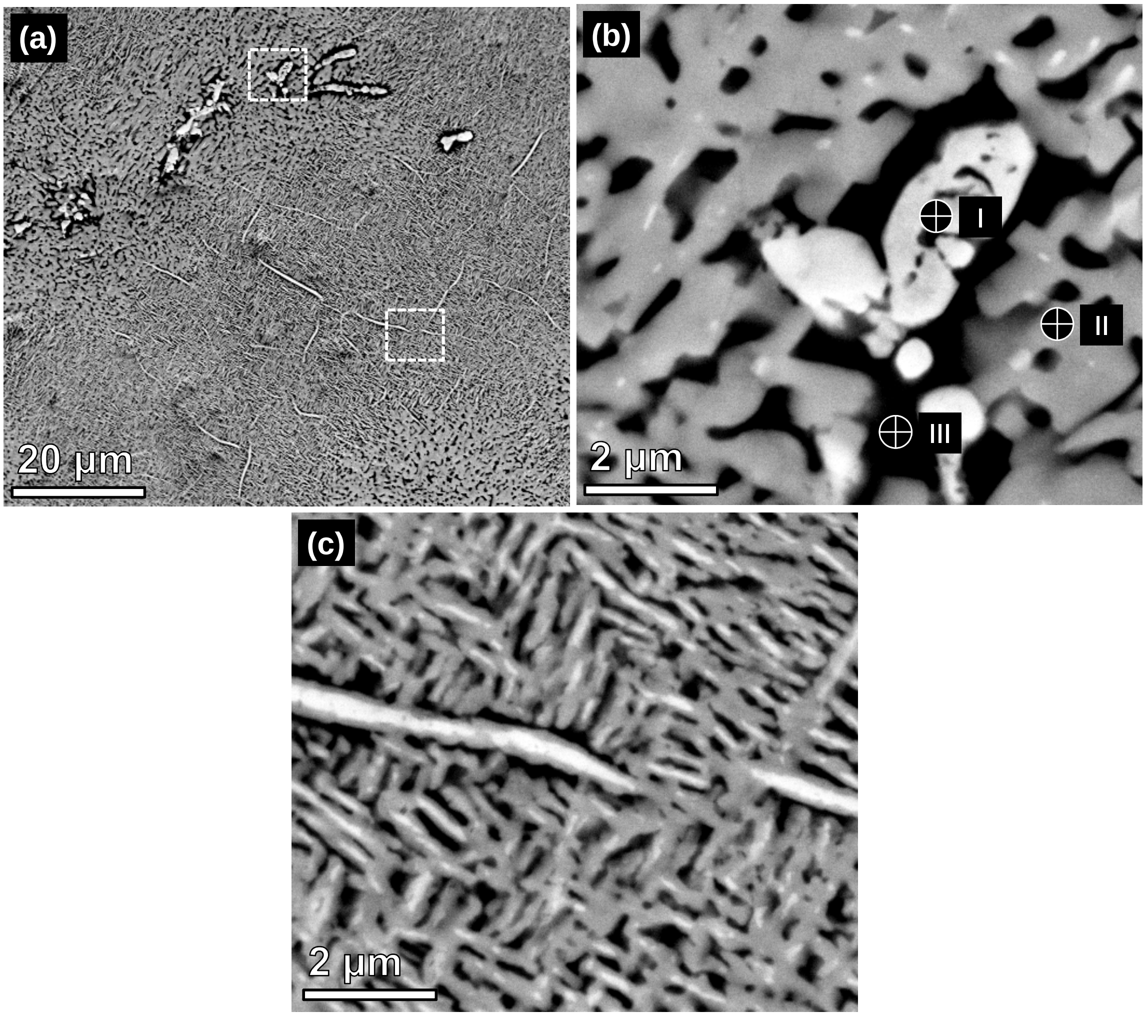

Figure 2.5: Backscattered electron image of the arc-melted $U_4Th_2Zr_9$ alloy prior to hydriding. The EDS spectra from the specified regions in (b) is shown in Figure 2.6.

form where the denderites are all graded in composition from the core to the outer shell. Therefore it is not feasible to pinpoint the exact chemical composition of each phase accurately while the presence of any impurities in the microstructure is ruled out.

The post hydriding specimens were investigated using a JEOL SEM instrument model JSM-5610 equipped with secondary and backscatter electron detectors and an Oxford ISIS EDS system. The accelerating potential during operation was 15 kV. Metallographic samples were prepared and a 50% nitric acid solution was used to etch the specimens. The samples were then sputter-coated with carbon to produce a conductive surface. No sign of preferential corrosion at grain boundaries was observed. Therefore the samples were examined under backscattering electron mode in order to generate

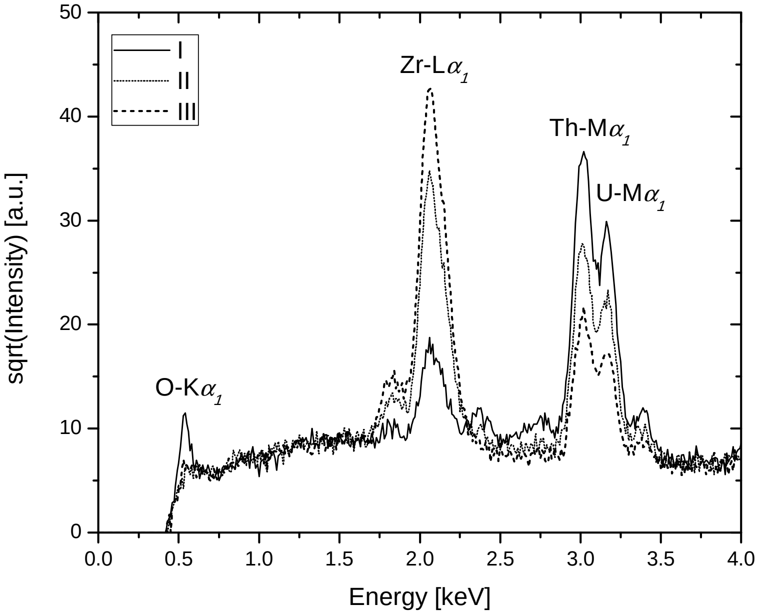

Figure 2.6: EDS spectra from the identified regions in Figure 2.5(b).

contrast based on the average atomic number in each phase; as shown in Figure 2.7. The morphology of both fuels showed three distinct phases. Each region corresponds to one of the structures identified in the X-ray diffraction results presented in the previous section, where the phases from brightest to darkest are α-U, $ThZr_2H_7$, and δ-$ZrH_{1.6}$ respectively. This is the case since the intensity of the backscattered image is proportional to the average atomic number in each phase. This is also in agreement with the corresponding EDS spectra (Figure 2.8).

Severe microcracking is observed in the microstructure of the $(UTh_4Zr_{10})H_{1.9}$ fuel, presumably as a result of volume expansion during processing. The cracks are both transgranular and intergranular, forming a network that expands across the microstructure. However, no sign of cracking is observed in the microstructure of $(U_4Th_2Zr_9)H_{1.5}$. This is in agreement with the calculated percent volume expansions of 22% and 18% upon hydriding for $(UTh_4Zr_{10})H_{1.9}$ and $(U_4Th_2Zr_9)H_{1.5}$ fuels, respectively. The morphology of both fuels shows elongated grains, but this feature is much more noticeable in the $(U_4Th_2Zr_9)H_{1.5}$ fuel. This morphology is due to the formation of dendrites during the solidification of metal alloys as seen in Figure 2.5(c). Uranium particles are evenly dispersed in small scale in $(UTh_4Zr_{10})H_{1.9}$ fuel ($\leq$1 μm in diameter) while in $(U_4Th_2Zr_9)H_{1.5}$ fuel the uranium particle distribution is random with large particle size. Similar characteristics can be seen for δ-$ZrH_{1.6}$ grains of different sizes with an average diameter in the range of a few micrometers. These micrographs further show that the ternary $ThZr_2H_7$ phase is the dominant phase in both fuels. This major chemical phase represents approximately 85 vol% of the $(UTh_4Zr_{10})H_{1.9}$ sample where it is

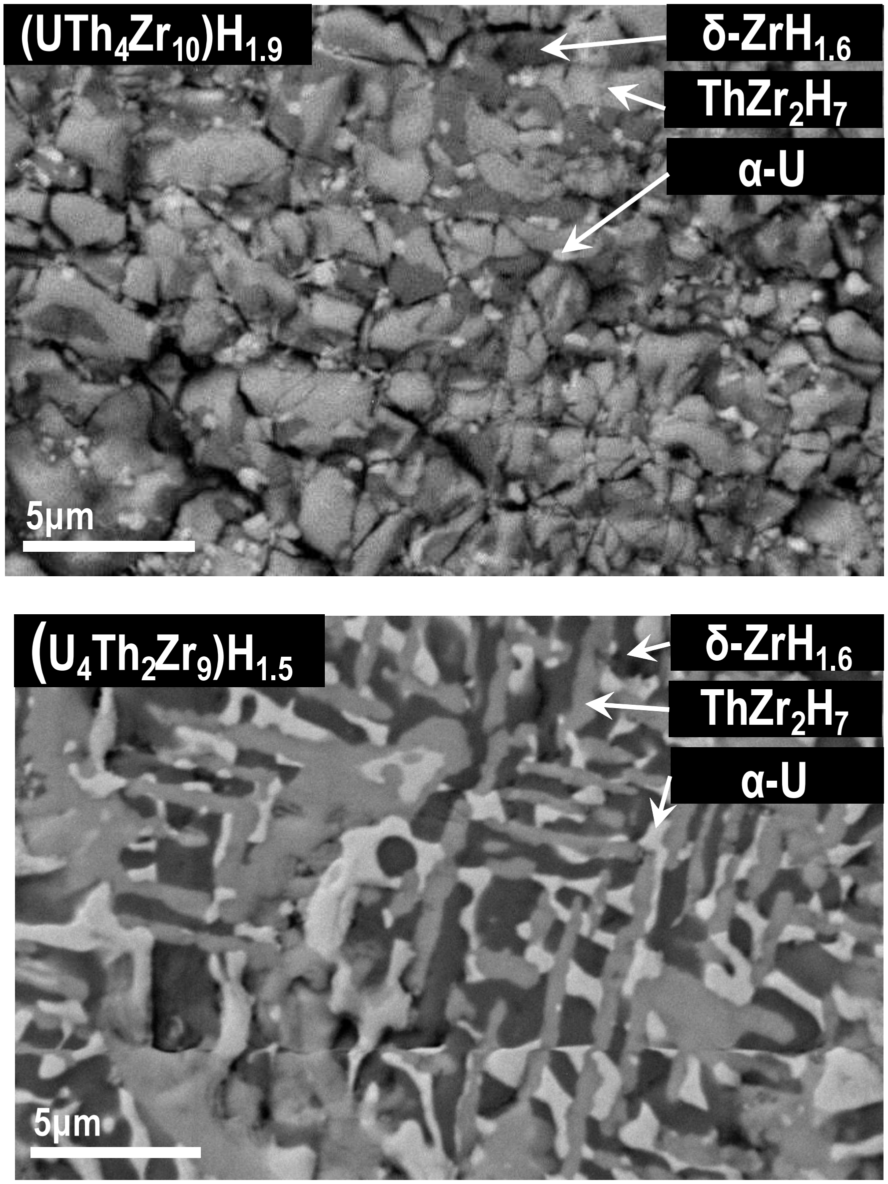

Figure 2.7: Backscattered electron image of: Top: $(UTh_4Zr_{10})H_{1.9}$; Bottom: $(U_4Th_2Zr_9)H_{1.5}$ fuels.

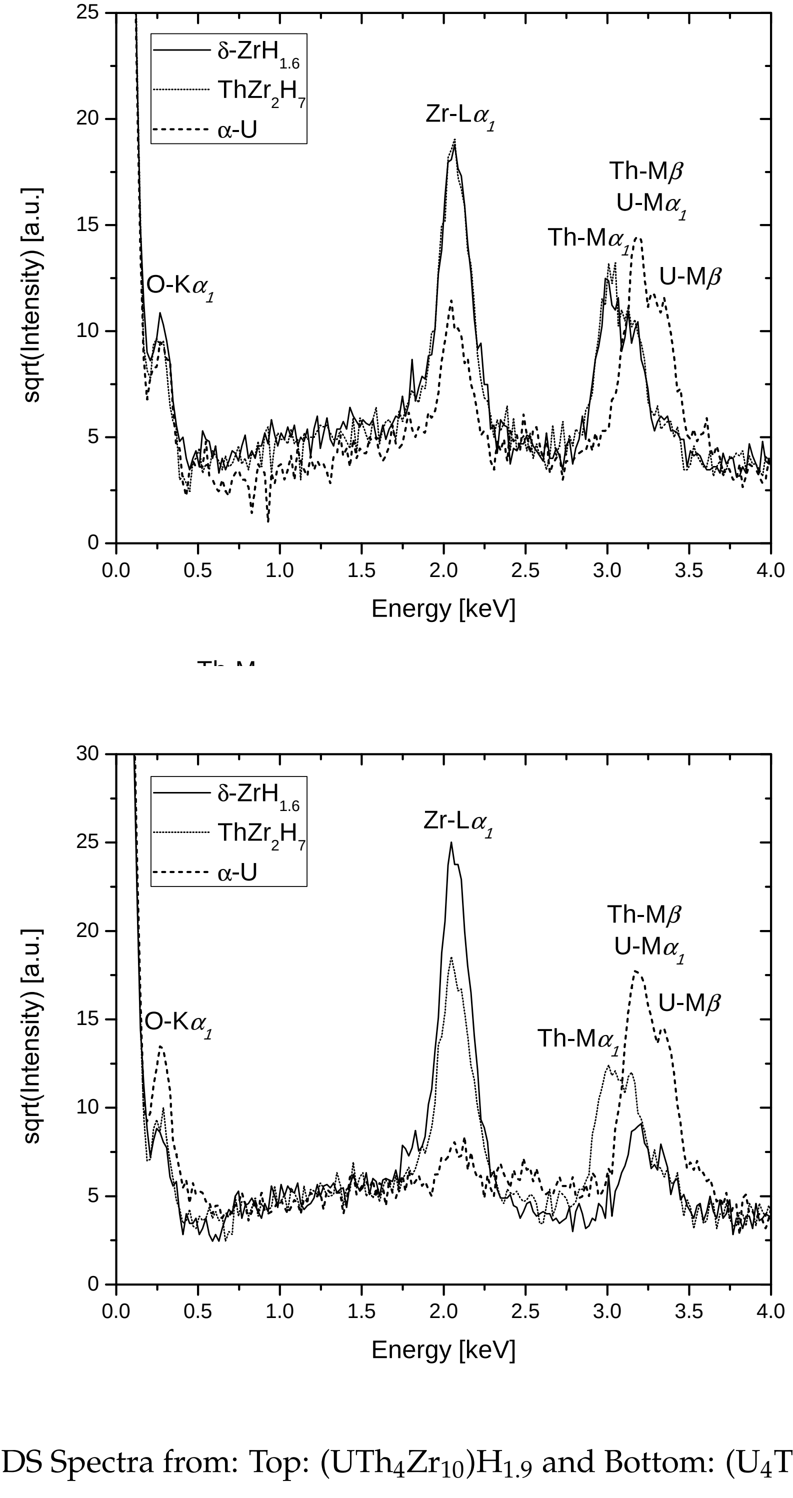

Figure 2.8: EDS Spectra from: Top: $(UTh_4Zr_{10})H_{1.9}$ and Bottom: $(U_4Th_2Zr_9)H_{1.5}$ fuels.

continuous. On the other hand only ~46 vol% of the $(U_4Th_2Zr_9)H_{1.5}$ sample constitutes this phase.

2.2.3 Transmission electron microscopy

Transmission electron microscopy was performed using a TECNAI-G2-F30 microscope with a 300 keV field emission gun. TEM images were recorded using a low scan CCD camera attached to a Gatan GIF 2000 image filter. Four TEM specimens were prepared through microtome cutting at thicknesses of 25 and 50 nm for each fuel. Thin samples are essential because of the significant electron beam attenuation by samples consisting of high atomic number elements. Powdered fuel was initially embedded in spur-resin in a micro-vial, which was then solidified at 60 °C overnight. The microtome specimens were cut using the diamond blade of a Leica EM UC6rt instrument and were then placed on a 3 mm copper grid supported by thin carbon film. Bright field and STEM (TEM in scanning mode) images of $(U_4Th_2Zr_9)H_{1.5}$ is presented in Figure 2.9. Images lack any morphological information since the specimens were prepared starting from fine powder, and during microtomy further cracking occurred. Dislocation-free grains of $ThZr_2H_7$ and δ-$ZrH_{1.6}$ phase are shown with good coherence at the grain boundary. EDS was performed by the TEM in scanning mode, confirming the composition of the grains shown in the image. The instrument was inadequate to generate selected area diffraction patterns due to complications with the intermediate aperture.

High resolution (HRTEM) images of $ThZr_2H_7$, δ-$ZrH_{1.6}$, and α-U phases were generated through phase contrast imaging. The microscope spherical and chromatic aberration coefficients were reported as 1.2 mm and 1.4 mm by the manufacturer. The Scherzer defocus condition (providing the most uniform contrast over a large range of reciprocal space distances) for the instrument was then calculated by Equation 2.2:

$$\Delta f_{Schz} = -1.2\sqrt{C_s\lambda} = -1.2\sqrt{(1.2\times10^6 nm)\,(1.969\times10^{-3} nm)} = -58.3nm \tag{2.2}$$

where C_s and λ are the spherical aberration coefficient and the electron wavelength, respectively. The value of defocus during imaging was unknown and it was later estimated through one of the following techniques. The first method, that was utilized for the $ThZr_2H_7$ phase, involves analysis of contrast transfer function contours based on scattering from an amorphous region of the sample. No amorphous region was present during imaging of the δ-$ZrH_{1.6}$ or α-U phase, and Bloch wave computer simulation [80] was used instead to estimate the defocus value. Figure 2.10 is the phase contrast image taken from $ThZr_2H_7$ phase at the 323 type zone axis in $(U_4Th_2Zr_9)H_{1.5}$ fuel (25nm thickness). To the bottom right of the figure is the fast Fourier transform (FFT) of the image that corresponds to the diffraction pattern from the 323 zone axis. To the top left of the image the {131} and {202} type planes are outlined in higher magnification.

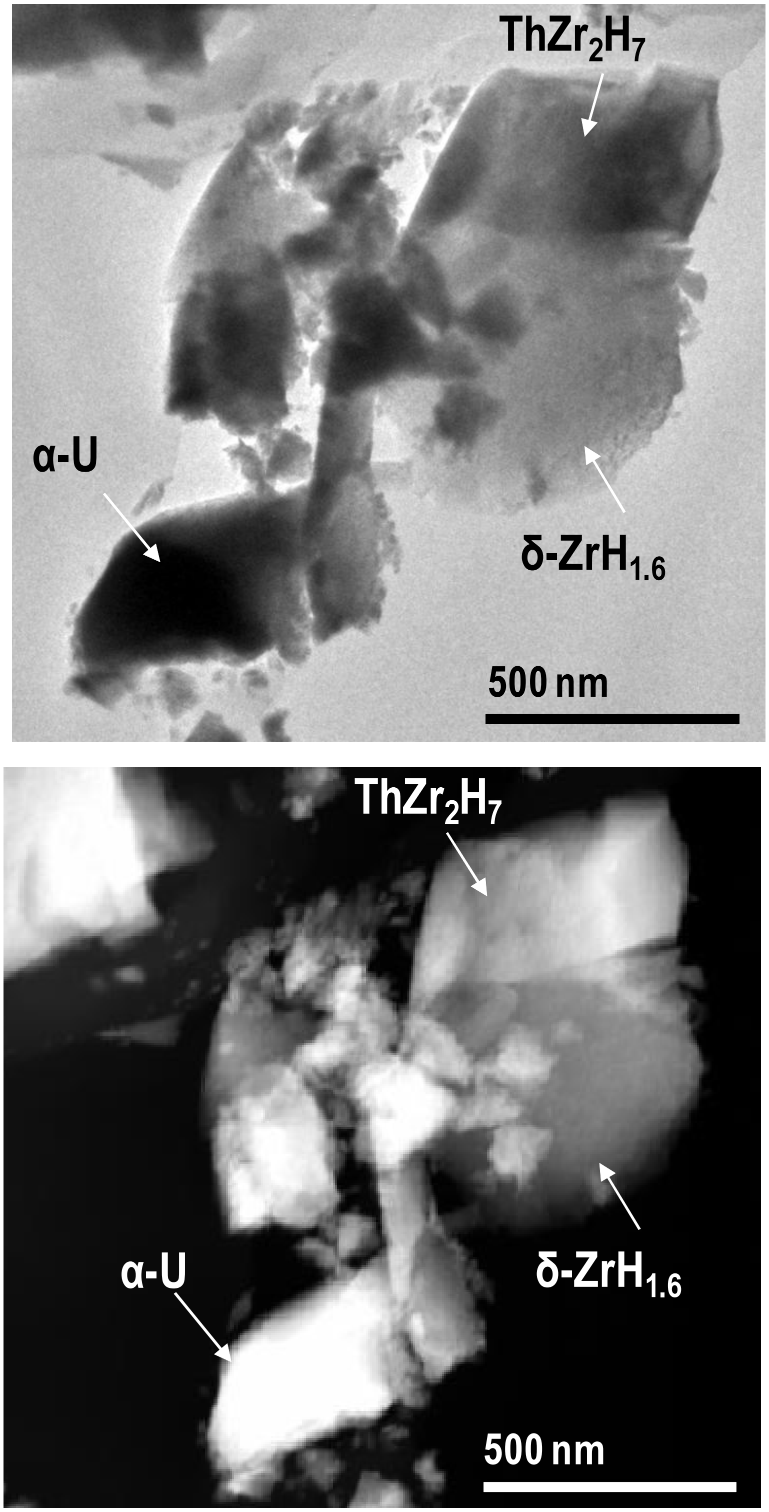

Figure 2.9: Top: Bright-field image of $(U_4Th_2Zr_9)H_{1.5}$ at 300 kV. Bottom: STEM image of same area showing contrast based on chemical composition.

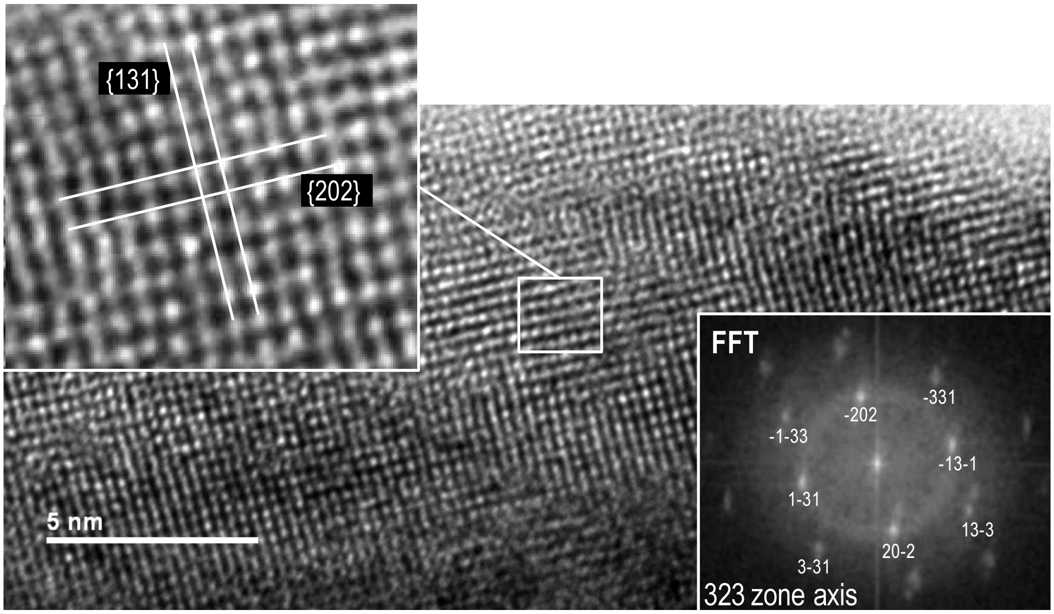

Figure 2.10: Phase-contrast image of 323 zone axis $ThZr_2H_7$ with FFT.

An amorphous area adjacent to the sample was used in order to determine the value of defocus. The amorphous material is capable of continuously scattering electrons over a large range of reciprocal lattice space distances. The contrast in the FFT of the image taken from the amorphous region would ultimately correspond to the contours in the square of the phase transfer function. Therefore the location of the dark and bright rings in the FFT match up with the reciprocal space distances where the transfer function is 0 and ±1 respectively. The phase contrast transfer function is calculated as shown in Equation 2.3.

$$T\left(r\right) = 2\sin\left[\pi\left(C_s\frac{\lambda^3 r^4}{2} + \Delta f \lambda r^2\right)\right] \tag{2.3}$$

The maximum and minimum in the square of the transfer function occurs when the expression inside the sin function is equal to $\frac{n\pi}{2}$ with n odd, and $\frac{n\pi}{2}$ with n even respectively. Therefore by matching the profile of the dark and bright rings to the following equation (Equation 2.4) the extent of defocus could be predicted. The amorphous region and the corresponding FFT are shown in Figure 2.11.

$$\frac{n}{r^2} = C_s\lambda^3 r^2 + 2\Delta f \lambda \tag{2.4}$$

The actual lengths in the FFT image (reciprocal space distance, r) are unknown since the picture is not calibrated in the reciprocal space. Therefore the length u, defined as r multiplied by a unit less proportionality constant m, is measured for each ring radius. Equation 2.5 could then be rewritten as:

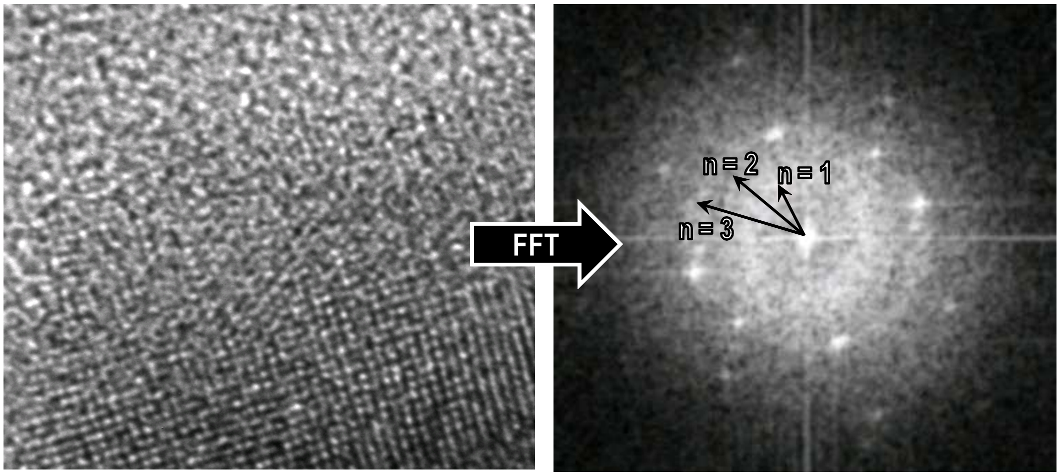

Figure 2.11: Amorphous region (top left corner) and FFT of the $ThZr_2H_7$ image (Δf=-100 nm).

$$\frac{n}{r^2m^2} = C_s\lambda^3\frac{r^2m^2}{m^4} + \frac{2}{m^2}\Delta f\lambda \xrightarrow{u=r.m} \frac{n}{u^2} = \frac{C_s\lambda^3}{m^4}u^2 + \frac{2}{m^2}\Delta f\lambda \tag{2.5}$$

Equation 2.5 is arranged such that a linear relationship between $\frac{n}{u^2}$ and u^2 exists. It is possible to plot $\frac{n}{u^2}$ v.s. $u^2$and thereby calculate the value of constant m and the extent of defocus based on the slope and y-intercept of the linear fit (Figure 2.12). The phase contrast transfer function at this value of defocus is presented in Figure 2.13. The position of the reciprocal space vectors corresponding to diffraction from {220}, {131}, and {331} type planes in $ThZr_2H_7$ is also shown along with the transfer function. The square of the phase contrast transfer function at these positions ultimately determines the contrast in the high resolution image. The intensity of diffraction spots in FFT of the HRTEM image on the $ThZr_2H_7$ phase in Figure 2.10 correspond well to what is predicted in Figure 2.13.

Figure 2.14 presents a high resolution image of δ-$ZrH_{1.6}$ in the $(U_4Th_2Zr_9)H_{1.5}$ fuel along with the indexed FFT and computer simulation of the high resolution image. FFT analysis of this image reveals a 110 type zone axis for the face centered cubic phase. It is noteworthy to point out that the X-ray and electron atomic scattering factors (f_θ) for hydrogen atom are small compared to the magnitude of such quantities for the zirconium, thorium and uranium atoms (i.e. at $\theta = 0$, $f_\theta^H = \frac{1}{40}\ f_\theta^{Zr} = \frac{1}{90}\ f_\theta^{Th} = \frac{1}{92}\ f_\theta^U$). Therefore the intensity of diffraction from hydrogen atoms (proportional to the square of the atomic scattering factor) vanishes as a part of the background. As was discussed previously δ-zirconium hydride is composed of zirconium atoms on a FCC lattice surrounding a SC hydrogen lattice within itself. Therefore the diffraction pattern is equivalent to only that of FCC zirconium atoms since the hydrogen atom scattering of electrons is negligible. No amorphous region was present during imaging of the δ-

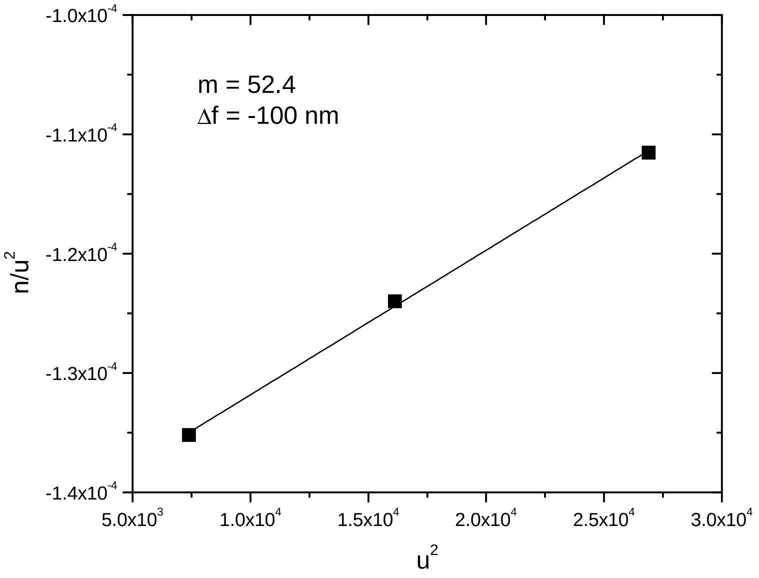

Figure 2.12: Determination of the extent of defocus from transfer-function amplitude variations in FFT of the image from an amorphous area of $ThZr_2H_7$.

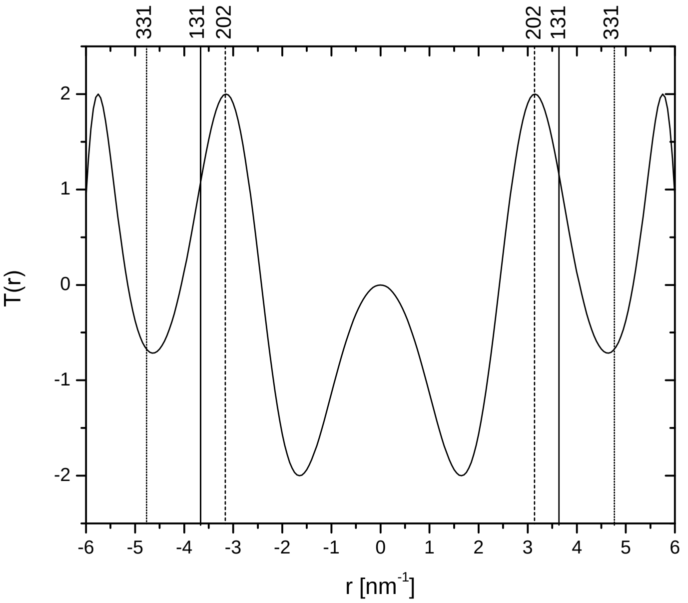

Figure 2.13: Phase-contrast transfer function at Δf = -100 nm (C_s = 1.2 mm).

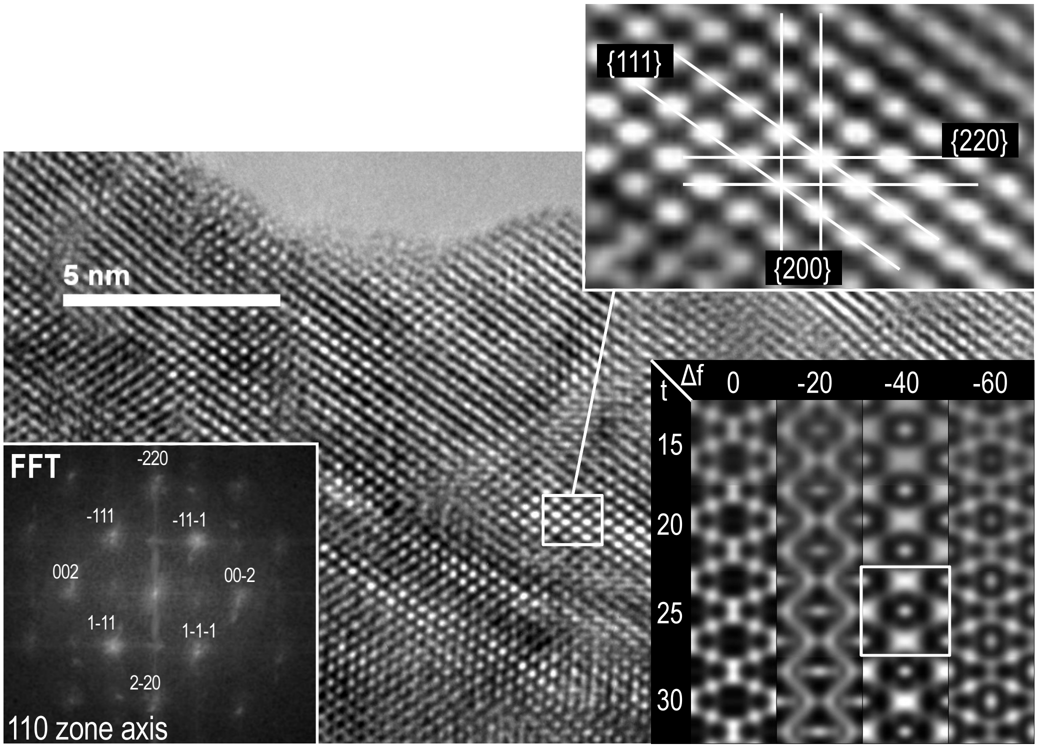

Figure 2.14: Phase-contrast image of 110 zone axis of δ-$ZrH_{1.6}$ (Δf = -40 nm) along with indexed FFT. In the computer simulation, box t and Δf correspond to thickness and defocus in nm respectively.

zirconium hydride phase and computer simulation was therefore used to estimate the extent of defocus during imaging. The computer simulation [80] is shown for various thicknesses and values of defocus, and the closest match to the experimental results is for the 25 nm thick sample with defocus of approximately -40 nm.

The final set of high resolution images is for the metallic uranium embedded in the hydride matrices (Figure 2.15). The structure of uranium at temperatures below 668 °C is orthorhombic. This temperature limit is slightly lowered as small amounts of zirconium is dissolved in the uranium metal (up to 1.1 at%). FFT of the phase contrast image corresponds to the 311 zone axis of the orthorhombic uranium. The high magnification image to the right is generated through inverse fast Fourier transformation of the corrected FFT. Corrected FFT refers to the pattern where all the background is masked off from the FFT and only the peaks corresponding to the 311 uranium pattern are allowed for image reconstruction. The extent of defocus is determined through computer simulation similar to what was discussed in the case of δ-$ZrH_{1.6}$; where it appears that the image is taken very close to the Scherzer defocus condition.

The observations from HRTEM are in agreement with the XRD and SEM results;

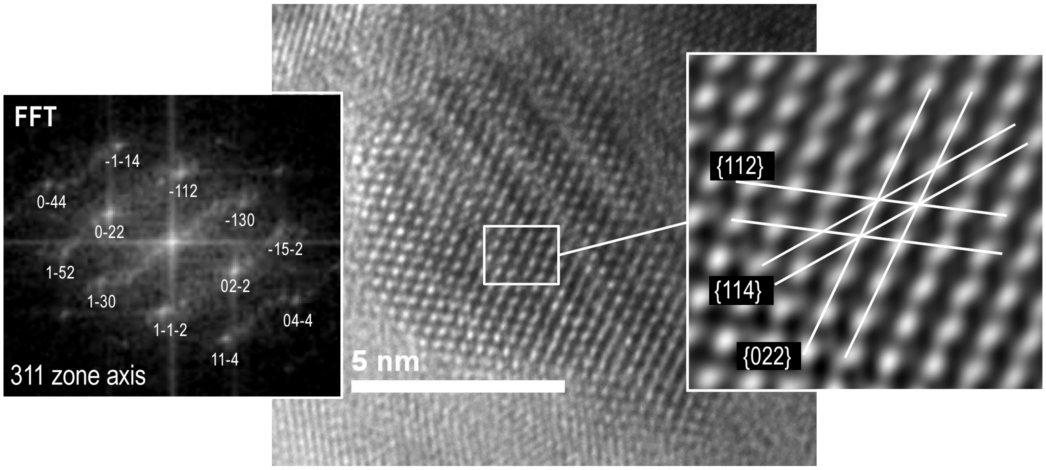

Figure 2.15: Phase-contrast image of 311 zone axis of α-uranium with FFT (Δf = -60 nm).

confirming the formation of $ThZr_2H_7$ and δ-$ZrH_{1.6}$. No sign of formation of tetragonal ε-$ZrH_{1.8}$ phase is observed. The FFT of the image corresponding to the uranium phase is representative of diffraction from an orthorhombic phase. This result rules out formation of significant amounts of cubic ε-UH_3.

2.2.4 Nanoscale dynamic mechanical mapping

DSM (TriboScope nanoindenter, Hysitron, Minneapolis, MN) coupled with an atomic force microscope controller (NanoScope IIIa, Veeco, Santa Barbara, CA) was used to determine the elastic modulus of the phases forming the uranium-thorium-zirconium hydride fuels. The technique provides topography as well as viscoelastic properties through storage and loss moduli mapping across the fuel microstructure at nanometer length scales. This was done by applying a sinusoidal electrostatic force acting on the spring-suspended center of the force-displacement transducer of the nanoindenter while contact mode imaging was conducted. A cube-corner diamond tip was attached to this transducer. The amplitude and the phase of the resulting transducer displacement signal were measured with a dual-channel lock-in amplifier, and this information was used to determine the local indentation moduli of the sample at each pixel of the imaging process. In the present case only the storage modulus (designated as elastic modulus) is reported due to negligible magnitudes of loss modulus found for the samples studied. The diamond tip radius used for imaging was calibrated by a standard quartz sample with an elastic modulus of 69.7 GPa. Balooch et al. [5] provide detailed description of the instrument and the technique.

Two regions of 3.5×3.5 μm^2 and 10×10 μm^2 in area were investigated in the $(U_4Th_2Zr_9)H_{1.5}$ fuel and the results are presented in Figure 2.16. The elastic modulus values are represented by the shades of gray in the images. The variation of the elastic modulus (black spots) along the black horizontal lines superimposed on the images is also shown for further clarification. Three distinct regions, corresponding to α-U, $ThZr_2H_7$, and δ-$ZrH_{1.6}$, are apparent from brightest to darkest, respectively. The microstructure in this set of images is directly comparable to what was previously characterized during backscattered scanning electron microscopy.

The elastic moduli of α-U and δ-$ZrH_{1.6}$ are reported as 202 GPa [28] and 130 GPa [78], respectively. The elastic moduli values determined in Figure 2.16 are in good agreement with the values reported previously for these two phases. The elastic modulus of the ternary $ThZr_2H_7$ phase, embedded in the fuel is reported, where the mean value is determined here as 172±5 GPa.

Monophase samples of $ThZr_2H_x$ with different hydrogen contents where fabricated in a separate study; as discussed in detail in Chapter 5. Elastic modulus and hardness of the material as a function of hydrogen content in the pure $ThZr_2H_x$ phase were determined using nanoindentation experiments. Figure 2.17 illustrates a typical load-displacement data, from which the elastic modulus and hardness of the material are extracted using the Oliver-Pharr method [49]. All the indentation experiments were performed with maximum force of 1500 μN. Typical penetration of the diamond indenter into the material was around 250 nm which guaranteed negligible contribution from surface impurities (i.e. surface oxide). 15 indentations were made for each sample where the mean and the standard deviation of the determined values are shown in Figure 2.18 as the scatter point and the error bar respectively. The large standard deviation for the metallic sample ($ThZr_2$ alloy) is due to the presence of the dendritic microstructure forming after the solidification of the melt; as discussed in detail in Section 5.2 (Figure 5.4). Also the value of elastic modulus for $ThZr_2H_7$, determined from the phase embedded in the $(U_4Th_2Zr_9)H_{1.5}$ fuel and discussed in the previous paragraph, is shown in Figure 2.18. The elastic modulus exhibits an increasing trend as function of hydrogen concentration. No information regarding the fracture toughness could be obtained since cracking at the indentation sites did not occur.

Deep indentation experiments were also performed on the fuel specimen in order to determine the fracture toughness of the phases present. However the indentations did not yield any useful results for two reasons. The first reason was that the thickness of these phases in the vertical direction was unknown. In other words during the indentation, it is likely that the surface region is thin enough such that the indentation results are representative of another phase that exists just below the surface. This was not a concern during modulus mapping since the extent of diamond tip penetration into the material was minimal; on the order of a few nanometers. The second reason was that no cracking at the edges of the indentation marks was observed and consequently the extraction of fracture toughness data was not possible. The indentation marks brought upon by the penetration of diamond tip (shaped as the corner of a cube) into the various phases is shown in Figure 2.19 where differences in the extent of penetration for the different phases are obvious. The penetration depth is representative of

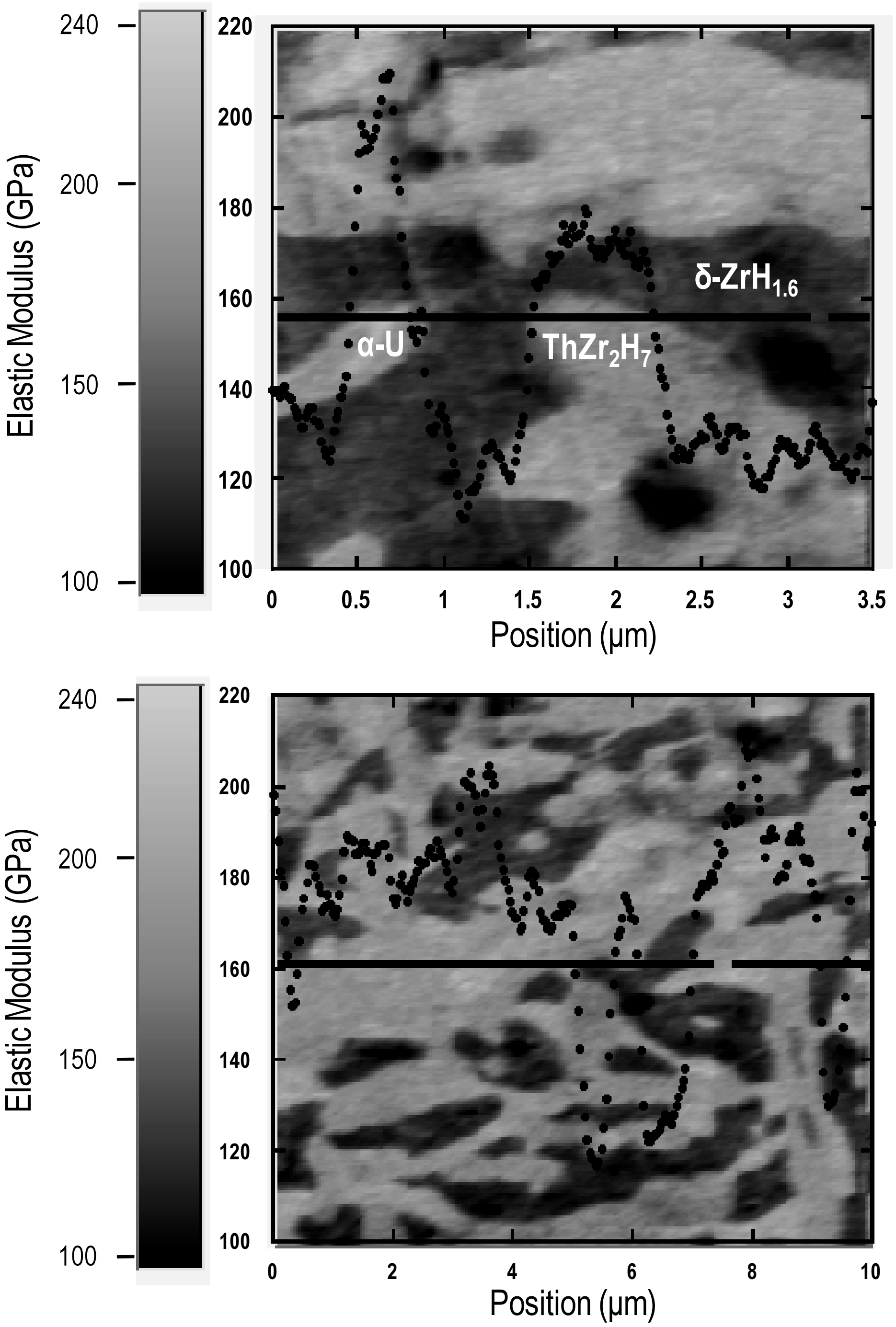

Figure 2.16: Elastic modulus mapping of the microstructure of $(U_4Th_2Zr_9)H_{1.5}$ fuel Top: 3.5×3.5 μm^2 area; Bottom: 10×10 μm^2 area.

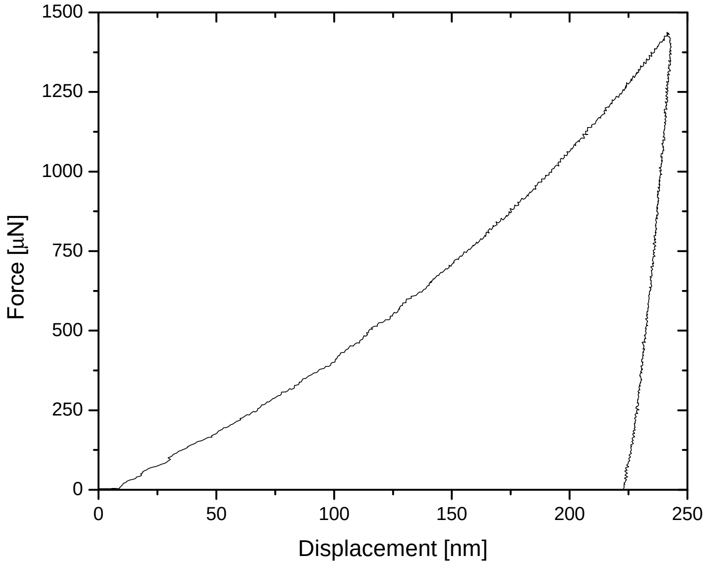

Figure 2.17: Load vs. displacement curve for $ThZr_2H_3$ nanoindentation.

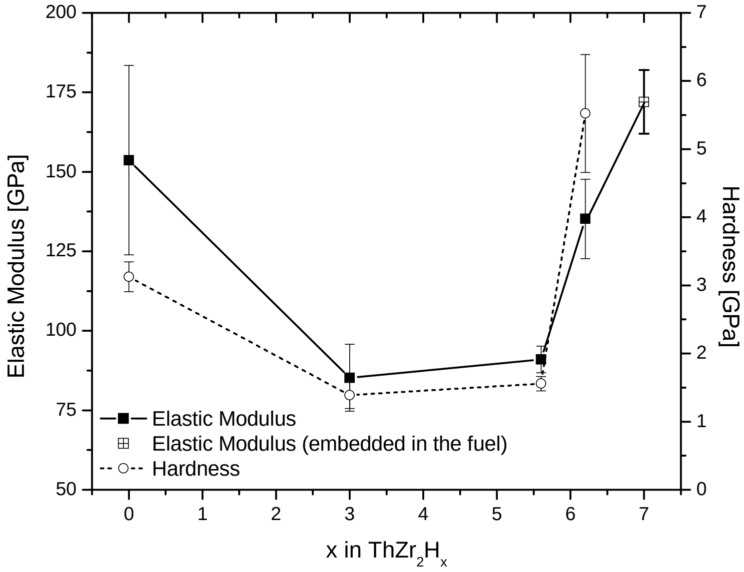

Figure 2.18: Elastic modulus and hardness values for thorium-zirconium hydride as a function of hydrogen stoichiometry.

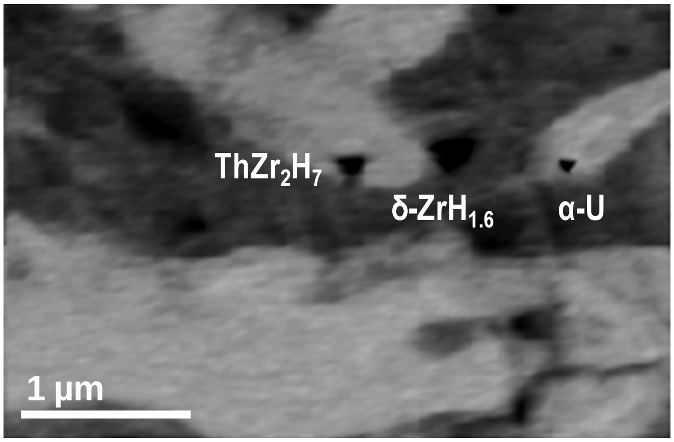

Figure 2.19: Comparison of indentation marks in $ThZr_2H_7$, δ-$ZrH_{1.6}$ and α-U.

the hardness for the specific phase; implying that the value of hardness is highest for α-uranium and lowest for δ-zirconium hydride. This is in agreement with the reported values for these phases where Vickers hardness of α-U (fine grain) and δ-zirconium hydride is approximately 250 HV [28] and 200 HV [35] respectively.

2.3 Discussion

Fuel fabrication could be improved by homogenization of the arc-melted metal alloys prior to hydriding in order to remove the dendritic structure. The hydriding process could also be greatly improved if the desired H/M ratio is initially established at high temperature and then maintained during the cool down. The diffusion-limited process takes place relatively quickly at high temperature under high pressure of hydrogen gas while the material is ductile enough to accommodate the large volume expansion. During the cool-down step, the hydrogen partial pressure should be continuously reduced to correspond to the desired H/M ratio. This inhibits formation of hydrogen concentration gradients that would in turn induce stress across the material. The equilibrium partial pressures of hydrogen with zirconium hydride and thorium-zirconium hydride are known [70, 9] as functions of temperature and are shown in Figure 2.20. At equilibrium, the activities of hydrogen in the gas and the two hydride phases are identical; therefore the exact H/M ratio in each phase could be determined. The equilibrium partial pressure of hydrogen changes by four orders of magnitude over the processing temperatures of these hydrides. Hence, sophisticated instrumentation and control systems are necessary to execute this procedure. The thermodynamic stability of the metal hydrides present in this system are functions of temperature and hydrogen concentration. Thermodynamic stability could be assessed by investigation of hydrogen activity (partial pressure); as shown in figure 2.20. Comparison of the value of hydrogen activity for these phases with that of UH_3 [44, 71] and ThH_2 [40] explains why the latter two phases have not precipitated during high-temperature hydriding. Uranium hydride is unstable above 420 °C (under 1 atm of H_2 gas). The residual uranium hydride formation, as detected by XRD analysis, is due to the presence of hydrogen in the furnace during the cool-down.

The density of hydrogen in hydride nuclear fuels is of great importance since it replaces a part of the moderator and thus significantly affects the neutronic properties. Figure 2.21 shows the hydrogen and uranium atomic densities in different hydride fuels as functions of atomic percent uranium dispersed in the hydride matrix. Uranium-thorium-zirconium hydride fuels are superior to uranium-zirconium hydride fuels since similar uranium atomic densities could be achieved with higher hydrogen atomic densities.

2.4 Summary

Two uranium-thorium-zirconium alloys were arc-melted and then hydrided to form fuels with the nominal compositions of $(UTh_4Zr_{10})H_{1.9}$ and $(U_4Th_2Zr_9)H_{1.5}$. Powder XRD analysis showed both these fuels consisted of the α-U, $\delta ZrH_{1.6}$, and $ThZr_2H_7$ phases with the latter phase dominant in both. SEM and TEM (in bright-field and high-resolution mode) imaging confirmed the presence of these three phases. Atomic force microscopy along with nanoscale dynamic stiffness analysis performed on fuel specimens to map the Young's modulus across the microstructure revealed the elastic modulus of $ThZr_2H_7$ embedded in fuel to be ~172 GPa. Separate nanoindentation experiments on pure $ThZr_2H_x$samples with different hydrogen stoichiometry were also performed to determine the elastic modulus as a function of hydrogen content. Both the elastic modulus and hardness of $ThZr_2H_x$ increase as a function of increasing hydrogen stoichiometry, for x between 3 and 7.

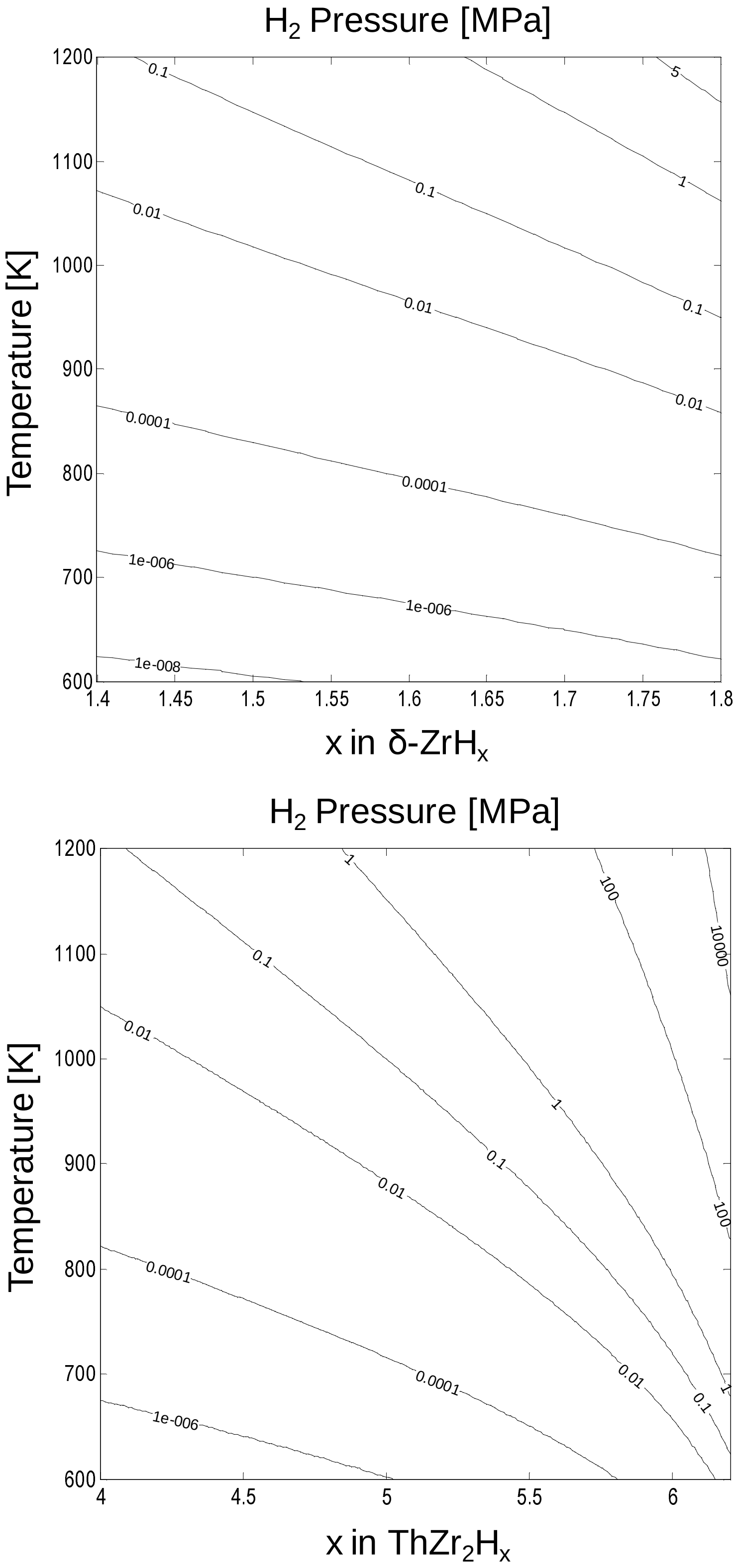

Figure 2.20: Pressure-temperature-hydrogen concentration equilibria for: Top: δ-ZrH_x and Bottom: $ThZr_2H_x$.

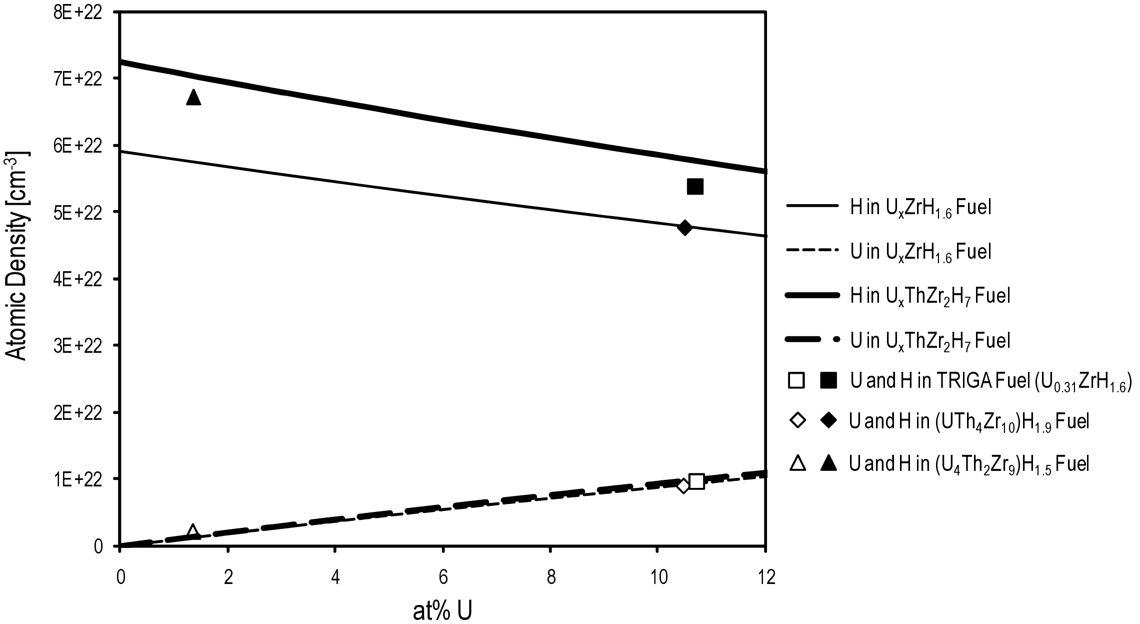

Figure 2.21: Hydrogen and uranium atomic densities as function of at% uranium metal in different hydride matrices.

Chapter 3

Transient Hydride Fuel Behavior in LWRs

The transient response of a uranium zirconium-hydride ($U_{0.31}ZrH_{1.6}$) fuel element to conditions typical of a light-water reactor reactivity-insertion accident is the subject of this chapter. Uranium-zirconium hydride fuel consists of metallic α-U phase dispersed in a δ-$ZrH_{1.6}$ matrix. The fuel is typically fabricated by hydriding of uranium-zirconium alloys formed by arc melting of the metal components. Uranium in the fuel remains metallic since the equilibrium partial pressure of the UH_3 phase at fuel processing temperatures is very high (pH_2 = 1 atm for UH_3 at ~700K); hydriding temperatures range from 800K - 1200K. Maximum heavy-metal loading inside the fuel is limited to 45 wt% uranium, which corresponds to the fuel composition of $U_{0.31}ZrH_{1.6}$.[1] During operation of the reactor, the temperature gradient across the fuel drives the hydrogen to the cooler regions due to the large heat of transport of hydrogen in the δ-$ZrH_{1.6}$ phase (T_Q = 640K) [58]. Thermal conductivity of the fuel is a function of both temperature and hydrogen concentration, with a stronger dependence on the latter. The volumetric heat capacity has the same dependencies; however its dependence on the temperature is more marked. Hydrogen diffusivity is an exponential function of temperature with a small dependence on hydrogen concentration (due to site-blocking by other hydrogen atoms during stochastic jumps).

It is therefore necessary to couple heat conduction to the hydrogen diffusion in order to achieve accurate results in predicting the temperature and hydrogen concentration profiles both under steady state and transient operating conditions. Accurate modeling of the coupled transient behavior will provide detailed information of the stress across the fuel as well as the necessary information for predicting the possibility of excessive hydrogen release from the fuel during accidents.

3.1 Methodology

Table 3.1 lists the notations, a description and respective units of all the variables discussed in the equations throughout this chapter.

3.1.1 Hydride fuel properties

3.1.1.1 Thermal conductivity and volumetric heat capacity

The fuel is a composite of metallic α-uranium dispersed in a δ-zirconium hydride matrix. The thermal conductivity of the fuel is the product of thermal diffusivity, density, and specific heat capacity of the composite material. These properties can be estimated using the rule of phase mixtures where thermal diffusivity and density are estimated on volume-fraction basis and heat capacity on mass-fraction basis, respectively.

---

[1] As consistent with the notation used in Chapter 2, hydrogen-to-uranium and hydrogen-to-zirconium ratios are 1.6:0.31 and 1.6:1, respectively.

Table 3.1: Nomenclature

C	H/Zr ratio	v	volume fraction
C_p	specific heat capacity [J/gr.K]	w	mass fraction
D	H diffusion coefficient [cm^2/s]	α	coefficient of thermal expansion [K^{-1}]
E	Young's modulus [GPa]	β	coefficient of expansion of hydrogen
h	heat transfer coefficient [W/cm^2.K]	δ_c/δ_g	cladding/gap thickness [cm]
J	radial flux [cm^{-2}/s]	ε_r, ε_θ, ε_z	radial, azimuthal, and axial strain
k	thermal conductivity [W/cm.K]	η	number of available adjacent jump sites
N_{Zr}	Zr number density in δ-ZrH$_{1.6}$ [cm^{-3}]	κ	thermal diffusivity [cm^2/s]
r	radial location in fuel pellet [cm]	λ	jump distance during diffusion [cm]
R	gas constant [kJ/mole.K]	ρ	mass density [kg/cm^{-3}]
R_f	fuel pellet radius [cm]	σ_r, σ_θ, σ_z	radial, azimuthal, and axial stress [MPa]
S	surface area/volume of shell [cm^{-1}]	τ	mean residence time in lattice site [s]
T	Temperature [K]	$\dot{q}^{m}$	volumetric heat generation rate [W/cm^3]
T_∞	Coolant temperature [K]	ν	Poisson's ratio
T_Q	heat of transport of H in δ-ZrH$_{1.6}$ [K]	ν_f	vibrational frequency inside lattice [s^{-1}]
T_{R_f}	fuel surface temperature [K]		

This requires the thermal properties of uranium as a function of temperature and zirconium hydride as a function of both temperature and H/Zr ratio [76, 64, 25, 68], as shown in Equation 3.1 (Figure 3.1). A similar approach can be used to determine the volumetric heat capacity of the fuel as a function of temperature and H/Zr ratio in the composite fuel (Figure 3.1). The influence of burnup on these properties is unknown and therefore this analysis is applicable only to fresh fuel. Thermal conductivity is expected to decrease as a function of burnup since hydride fuel experiences large swelling rates associated with void formation in the hydride matrix, especially at low burnups. Hydride fuel also has good fission-gas retention properties which indicates voids containing noble gases form during operation (see Chapter 1). This is related to swelling and will further deteriorate the thermal conductivity.

$$k = k_U \left(v_U + \frac{\kappa_{ZrH_{1.6}}}{\kappa_U} \left(1 - v_U\right) \right) \left(v_U + \frac{\rho_{ZrH_{1.6}}}{\rho_U} \left(1 - v_U\right) \right) \left(w_U + \frac{C_{p,ZrH_{1.6}}}{C_{p,U}} \left(1 - w_U\right) \right) \tag{3.1}$$

3.1.1.2 Hydrogen diffusivity

The diffusivity of hydrogen in zirconium hydride has been measured over a large range of temperatures and hydrogen concentrations by Majer et al. [39]. The only set of data corresponding to δ phase zirconium hydride (H/Zr ratio = 1.58) yields the diffusion coefficient as:

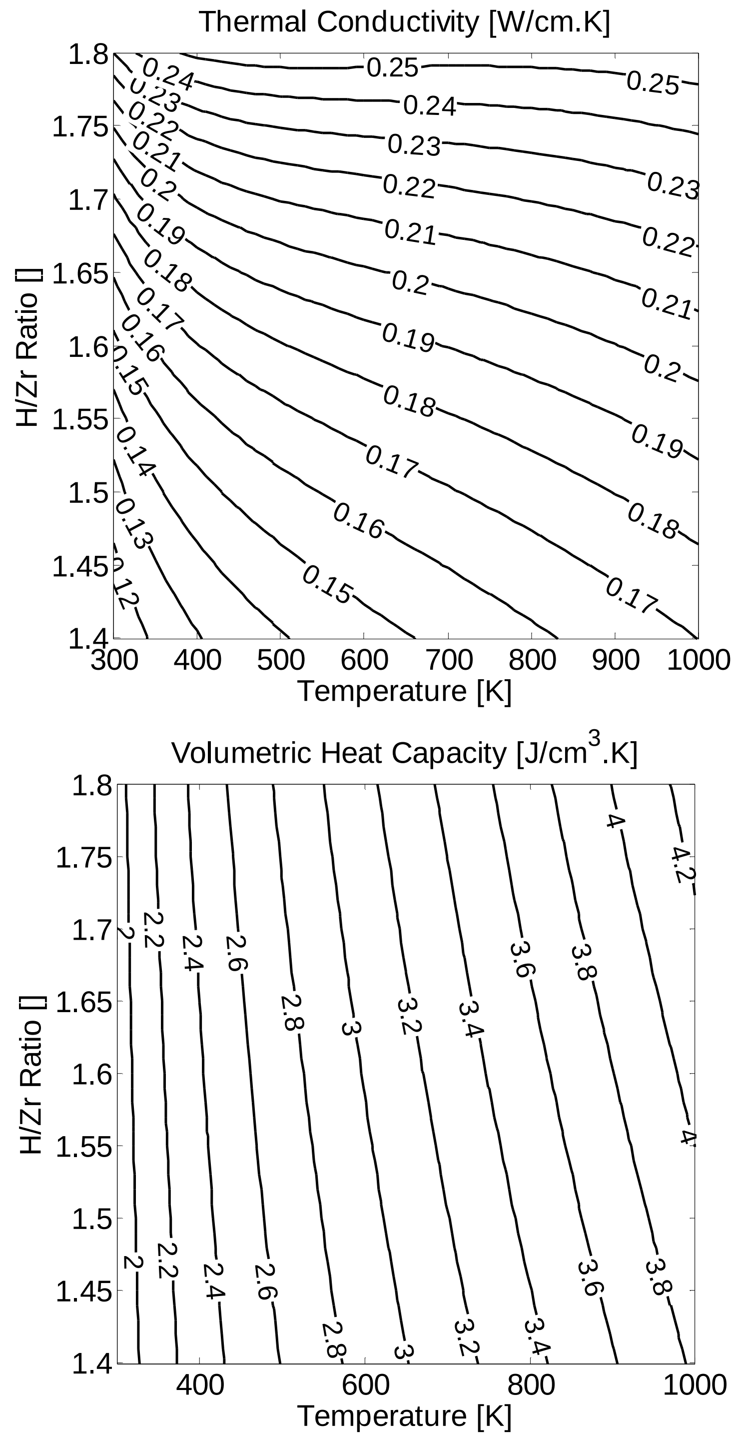

Figure 3.1: Top: Thermal conductivity; Bottom: volumetric heat capacity of the $U_{0.31}ZrH_x$ fuel as functions of temperature and H/Zr ratio.

$$D = 1.53 \times 10^{-3} \exp\left(\frac{-58.8}{RT}\right) \tag{3.2}$$

The Einstein diffusion model describes the diffusion coefficient as the following:

$$D = \frac{1}{6}\frac{\lambda^2}{\tau} \tag{3.3}$$

where λ is the jump distance of the diffusing species and τ is the mean residence time in each site before a jump. The latter is inversely proportional to the product of the number of available adjacent jump sites (η) and the jump frequency. The jump frequency is the product of vibration frequency of the species in that site (ν_f) with an Arrhenius factor that determines the probability of each vibration leading to a successful jump. Therefore, the pre-exponential factor in the diffusion coefficient can be expressed as:

$$D_\circ = \frac{1}{6}\lambda^2 \eta \nu_f \tag{3.4}$$

η is the product of the number of adjacent jump sites (6, since hydrogen is on a simple cubic lattice inside the face centered cubic Zr unit cell where the overall structure corresponds to a $Fm\overline{3}m$ space group) with the probability that the site is not currently occupied by another hydrogen atom. This probability can be determined from the stoichiometry and structure of the system; the pre-exponential term can therefore be estimated as:

$$D_\circ = \lambda^2 \left(1 - \frac{C}{2}\right) \nu_f \tag{3.5}$$

Activation energy for diffusion is essentially independent of hydrogen concentration, assuming the mechanism of diffusion doesn't change in the range of interest (H/Zr ratio from 1.5 to 1.7). The final expression that is used for the diffusion coefficient of hydrogen in δ-ZrH_x is the following:

$$D = 7.29 \times 10^{-3} \left(1 - \frac{C}{2}\right) \exp\left(\frac{-58.8}{RT}\right) \tag{3.6}$$

3.1.2 Heat conduction model

The transient radial heat conduction equation for an axial slice of fuel with internal heat generation and variable properties is shown below:

$$\frac{\partial}{\partial t}\left(\rho C_p T\right) = \frac{1}{r}\frac{\partial}{\partial r}\left(kr\frac{\partial T}{\partial r}\right) + \dot{q}^m \tag{3.7}$$

All terms are treated as radially- and temporally-variant except for the internal heat generation which is approximated as spatially uniform. The validity of this assumption is addressed in detail in Section 3.3.3. The steady-state solution defines the initial condition and the time-dependent heat-generation rate $\dot{q}^m$ drives the transient. The two boundary conditions are zero heat flux at the fuel centerline and a fuel surface temperature that depends on the coolant temperature and the intervening conductance. This second relation is shown below.

$$T_{R_f}(t) = -\frac{k_{R_f}(t)}{h} \left.\frac{\partial T}{\partial r}\right|_{R_{f,t}} + T_\infty \tag{3.8}$$

where the heat conductance, h, is defined as [19]:

$$\frac{1}{h} = R_f \frac{\ln\left(1 + \frac{\delta_{gap}}{R_f}\right)}{k_{gap}} + \left(R_f + \delta_{gap}\right) \frac{\ln\left(1 + \frac{\delta_{clad}}{R_f + \delta_{gap}}\right)}{k_{clad}} + \frac{1}{h_{hyd}} \tag{3.9}$$

A semi-implicit Crank-Nicolson scheme is used [15] whereby time is discretized with the trapezoid rule and space with the central-difference formula. This method assures inherent stability and second-order accuracy. The solution might require an iterative predictor-corrector algorithm since the iterate is not known explicitly. However, if the relation is formed into a linear system, the problem is transformed into solving a sparse linear system of equations at each time-step. Fortunately, MATLAB® contains LAPACK, a library of linear algebra subroutines that solves linear systems such as these quickly and accurately. The full discretization of the heat equation can be found in Section 3.4.1.

3.1.3 Hydrogen diffusion model

The driving force for flux of hydrogen atoms across the fuel exists due to temperature and concentration gradients across the pellet. The radial flux is equal to:

$$J_r = -DN_{Zr}\left(\frac{dC}{dr} + \frac{T_Q C}{T^2}\frac{dT}{dr}\right) \tag{3.10}$$

After relating the flux and concentration in a conservation equation such as in Huang et al. [30], an explicit time-discretization scheme can be used since the rate of change of the concentration is small and linearization introduces only small errors. The flux at the surface of the fuel is approximated to be zero; the accuracy of this simplification is addressed in Section 3.3.2. In the conservation equation, the fluxes are multiplied by the surface area to volume ratio which correspond to the surface through which the flux is passing and the volume of fuel in which hydrogen resides. Since hydrogen exists only in the δ-ZrH$_x$ phase (the flux of hydrogen atoms in the α-U phase is negligible [30]), this area-to-volume ratio is weighted by the volume fraction of this

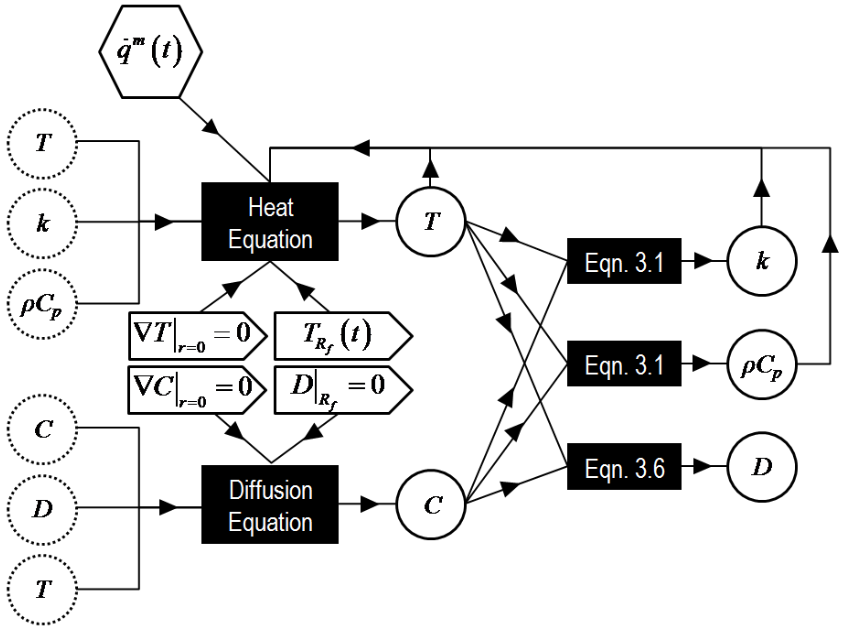

Figure 3.2: A single time-step in the solution algorithm.

phase (~0.9). The fully-expanded discretized diffusion equation and its derivation can be found in Section 3.4.2.

3.1.4 Coupling algorithm

As mentioned earlier, there is a high degree of interdependency of the pertinent variables. The heat conduction equation depends on thermal conductivity and volumetric heat capacity. The hydrogen diffusion equation depends on temperature, hydrogen concentration, and diffusivity. The diffusivity, thermal conductivity, and volumetric heat capacity all depend on temperature and hydrogen concentration.

The following operator-splitting algorithm is used for each time step. The heat conduction equation is semi-implicitly solved for the current temperature using properties from the previous time step and extrapolated properties for the current time step (see Section 3.4.1). Next, the hydrogen concentration is explicitly calculated for the current time step using parameters from the previous time step (see Section 3.4.2). Third, the diffusivity, thermal conductivity, and volumetric heat capacity are updated with the current temperature and hydrogen concentration. This process is shown in Figure 3.2 where arrows denote inputs, circles are variables (dashed lines denote the previous time step), rectangles are equations, pentagons are boundary conditions, and the hexagon is power density (assumed independent of other variables).

Before the transient solution algorithm is run, the steady-state equations are solved using a similar process with a relative error tolerance for convergence of 10^3 times machine precision.

3.1.5 Stress calculation

The two sources of strain in the material arise from temperature and hydrogen concentration gradients across the fuel. Olander [48] reported the linear coefficient of expansion of hydrogen as β=0.027 per unit change of H/Zr ratio in ZrH_x. The temperature dependent coefficient of thermal expansion of the zirconium hydride has been reported as $\alpha = 3.36 \times 10^{-6}\left(1 + 4.40 \times 10^{-3} T\right)$ per unit change of temperature in Kelvin [56]. The elastic modulus of zirconium hydride is approximately 130 GPa in the temperature range of interest [78]. The elastic modulus of the composite fuel is obtained using the rule of mixtures as 145GPa (vol% α-U = 19.4). Using a similar analysis, Poisson's ratio for the composite is 0.3 ($\nu_{\alpha-U}$ = 0.23, $\nu_{ZrH_{1.6}}$= 0.32 [78]). Total strain in the fuel is the sum of elastic, thermal and hydrogen strains. The constitutive equations in the axi-symmetric cylindrical coordinates are then presented as[2]:

$$\varepsilon_r = \frac{1}{E}\left[\sigma_r - \nu\left(\sigma_\theta + \sigma_z\right)\right] + \alpha\left(\Delta T\right) + \beta\left(\Delta C\right) \tag{3.11}$$

$$\varepsilon_\theta = \frac{1}{E}\left[\sigma_\theta - \nu\left(\sigma_r + \sigma_z\right)\right] + \alpha\left(\Delta T\right) + \beta\left(\Delta C\right) \tag{3.12}$$

$$\varepsilon_z = \frac{1}{E}\left[\sigma_z - \nu\left(\sigma_\theta + \sigma_r\right)\right] + \alpha\left(\Delta T\right) + \beta\left(\Delta C\right) \tag{3.13}$$

where ΔT and ΔC are the magnitudes of the difference between the temperature and hydrogen concentration across each radial mesh point, respectively. Eliminating the displacement vectors in the definition of cylindrical strains, the relationship in Equation 3.14 is obtained. Using the constitutive equations coupled with this condition and assuming plane-strain in the axial direction, a differential equation governing the radial stress across the fuel is determined (Equation 3.15). The fuel is assumed initially restrained in the axial direction (the plain-strain assumption); later by application of Saint Venant's principle the unrestrained axial stress is determined [52]. The two boundary conditions are zero stress gradients at the fuel centerline and zero radial stress at the fuel surface.

$$\frac{d\varepsilon_\theta}{dr} + \frac{\varepsilon_\theta - \varepsilon_r}{r} = 0 \tag{3.14}$$

---

[2] Since strain is a tensor and this is a multi-axial stress problem, the displacements due to thermal and hydrogen expansion need to be accounted for simultaneously in the constitutive equations. In other words, solving the constitutive equations once only accounting for thermal expansion and another time only taking into effect the hydrogen expansion followed by linear summation of strains would result in an incorrect answer.

$$\frac{1}{r}\frac{d}{dr}\left(r^3\frac{d\sigma_r}{dr}\right) = \frac{-E}{1-\nu}\left[\frac{d}{dr}(\alpha T) + \beta\frac{dC}{dr}\right] \tag{3.15}$$

The radial equilibrium condition in cylindrical coordinates (Equation 3.16) is used to calculate the azimuthal stress across the fuel based on the radial stress.

$$\sigma_\theta = \frac{\partial}{\partial r}(r\sigma_r) \tag{3.16}$$

To determine the distribution of axial stress across the fuel, the axial stress is first calculated assuming complete restraint in the axial direction (ε_z = 0). Then the difference from the average of this quantity across the fuel is denoted as the actual magnitude of axial stress (Saint Venant's principle). For complete set of calculations showing the derivation of different stress components see Section 3.4.3.

Simpson and Cann [57] report the mode I fracture toughness of δ-zirconium hydride as 3 MPa.m$^{\frac{1}{2}}$ at 573 K. Ductile-phase toughening in the fuel due to the presence of uranium particles is expected by crack-bridging and process-zone-toughening mechanisms. By conservatively ignoring such effects, linear elastic fracture mechanics can be applied. However finite element methods are necessary to predict the evolution of flaw size in the material due to the complex state and distribution of stress and are beyond the scope of this work. An adequate scheme would be to artificially assign cracks to different regions of the material that would in turn correspond to dissimilar states of stress. The progression in flaw size and geometry that correspondingly depends on the evolution of the changing stress state can then be studied.

3.1.6 Model physical parameters

The model was composed of a fuel element 1 cm in diameter, housed inside a Zircaloy cladding of 0.9 mm in thickness, with a 70 μm molten lead-tin-bismuth (Pb-33.3wt%Sn-33.3wt%Bi) gap in between. The gap and cladding were not modeled explicitly but instead were introduced as the outer boundary condition along with the hydraulic conditions. The conductivities used for the liquid-metal (LM) gap and clad were 0.20 W/cm.K [15] and 0.16 W/cm.K [16], respectively. The thermal-hydraulic heat transfer coefficient was estimated using the Presser correlation for the Nusselt number with the typical geometry and operating parameters of a PWR, resulting in an approximate value of 1 W/cm^2.K. The bulk coolant temperature was 575 K and the pitch-to-diameter ratio was 1.2. The fuel-averaged H/Zr ratio was 1.6.

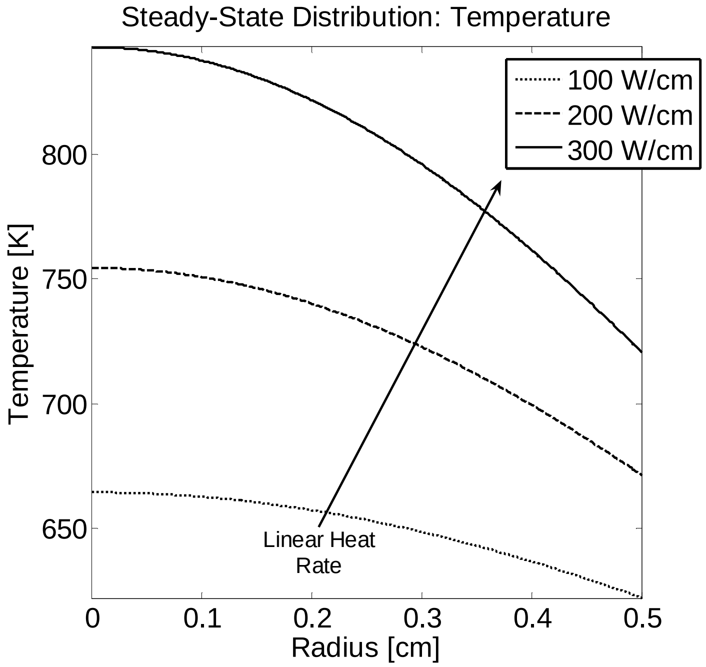

Figure 3.3: Steady-state temperature distributions at LHRs of 100, 200, and 300 W/cm.

3.2 Results

3.2.1 Steady-state results

The steady-state calculations were conducted with 500 spatial nodes at linear heat rates (LHR) of 100, 200, and 300 W/cm. The results of the steady state temperatures, H/Zr ratios, and axial stress distributions are shown in Figures 3.3, 3.4, and 3.5, respectively.

As expected, the fuel temperature gradient and outer fuel temperature increase with LHR. The hydrogen concentration gradients are also steeper with increasing LHR. With a LM bonded fuel, even though the average temperature is lower when compared to the conventional He gap fuel, the extent of hydrogen redistribution is more severe (as reported by Olander [48]). This has been confirmed by the model but is not shown here. This trend is justified by inspection of the flux governing equation where the T^{-2} dependence of the temperature gradient term enhances its impact at lower temperatures.

The largest component of stress is the axial stress, whose value is influenced by the temperature and hydrogen concentration gradients in an opposing manner. However, hydrogen-induced stresses are the dominant component, as is evident from the steady state results. Generally, the fuel surface experiences severe compression from axial and azimuthal components of stress, while all three components of stress are tensile at

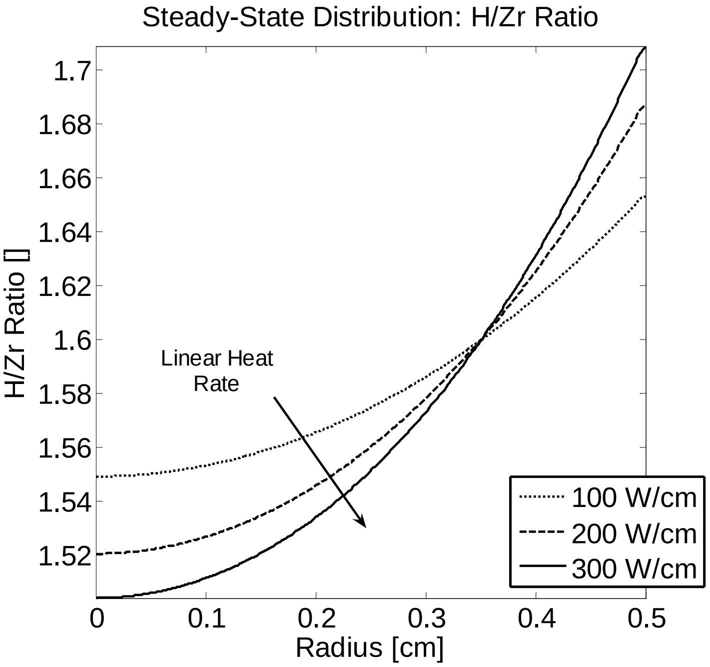

Figure 3.4: Hydrogen concentration across the fuel pellet at LHRs of 100, 200, and 300 W/cm.

the central region of the fuel. Even though the hydrogen redistribution is larger with increasing LHR, the magnitude of stress might not increase due to larger thermally-induced strains.

3.2.2 Transient results

A parametric transient case study was completed with a nominal LHR of 300 W/cm and coolant temperature of 575 K, respectively. The power was pulsed to twice the nominal value (to 600 W/cm) for 2.5 seconds and then dropped to 5% of that limit while the coolant temperature and fuel-to-coolant conductance remained constant. This represents a simplified and exaggerated reactivity insertion accident (RIA) with a large pulse height, a long pulse width, and a subsequent SCRAM. The hydrogen redistribution, although present, is miniscule since the hydrogen diffusivity is orders of magnitude smaller than the thermal diffusivity (~2×10^{-8} cm^2/s compared to ~6×10^{-2} cm^2/s). Consequently, only the resultant spatial fuel temperature and axial stress distributions are shown in Figure 3.6.

The fuel temperature directly follows the power pulse, rapidly peaking as the power jumps and then relaxing down after the SCRAM. The stress response of the fuel is interesting in that the axial stress is actually lowered and flattened during the power pulse. This is caused by the increased thermal stresses that counteract the dominat-

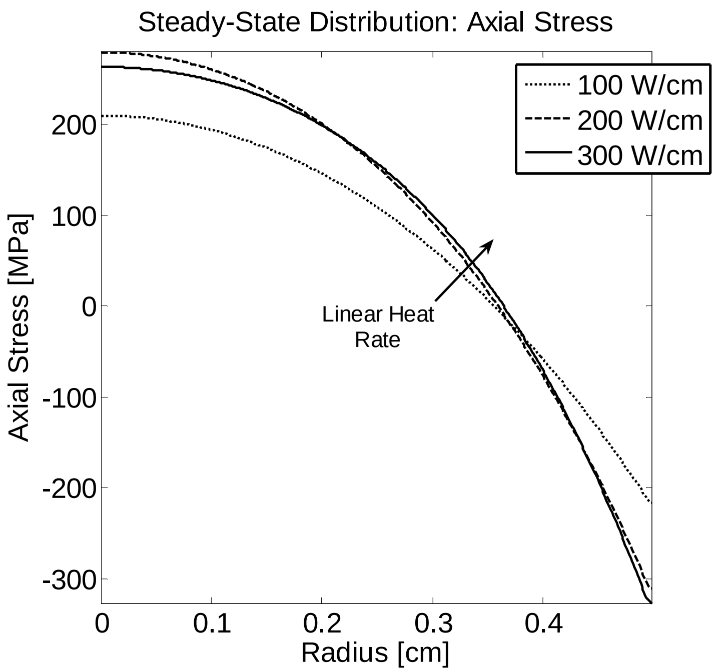

Figure 3.5: axial stress distribution across the fuel pellet at LHRs of 100, 200, and 300 W/cm.

ing stresses created by the hydrogen concentration gradient. As the fuel cools during the SCRAM portion, the hydrogen-induced stresses remain unopposed and the overall stress increases. Figure 3.7 shows the maximum fuel temperature for various pulse heights and durations induced on a fuel operating with nominal linear heat rate of 300 W/cm.

3.3 Discussion

3.3.1 Comparison of constant properties and variable properties

Table 3.2 summarizes the relative percent error accrued by using material properties that are independent of temperature and hydrogen concentration for a steady-state solution. The constant values used for thermal conductivity and volumetric heat capacity were 0.16 W/cm.K and 2.3 J/cm^3.K. Results are shown for LHRs of 100, 200, and 300 W/cm. Although the relative percent errors may seem small, a 3% relative difference amounts to 30 K at a temperature of 1000 K. Also, at 100 W/cm, the overshoot in temperature and undershoot in H/Zr ratio at the fuel centerline causes a 12% error in the axial stress. A moderate discrepancy in any of these terms may have a significant effect on the overall fuel behavior.

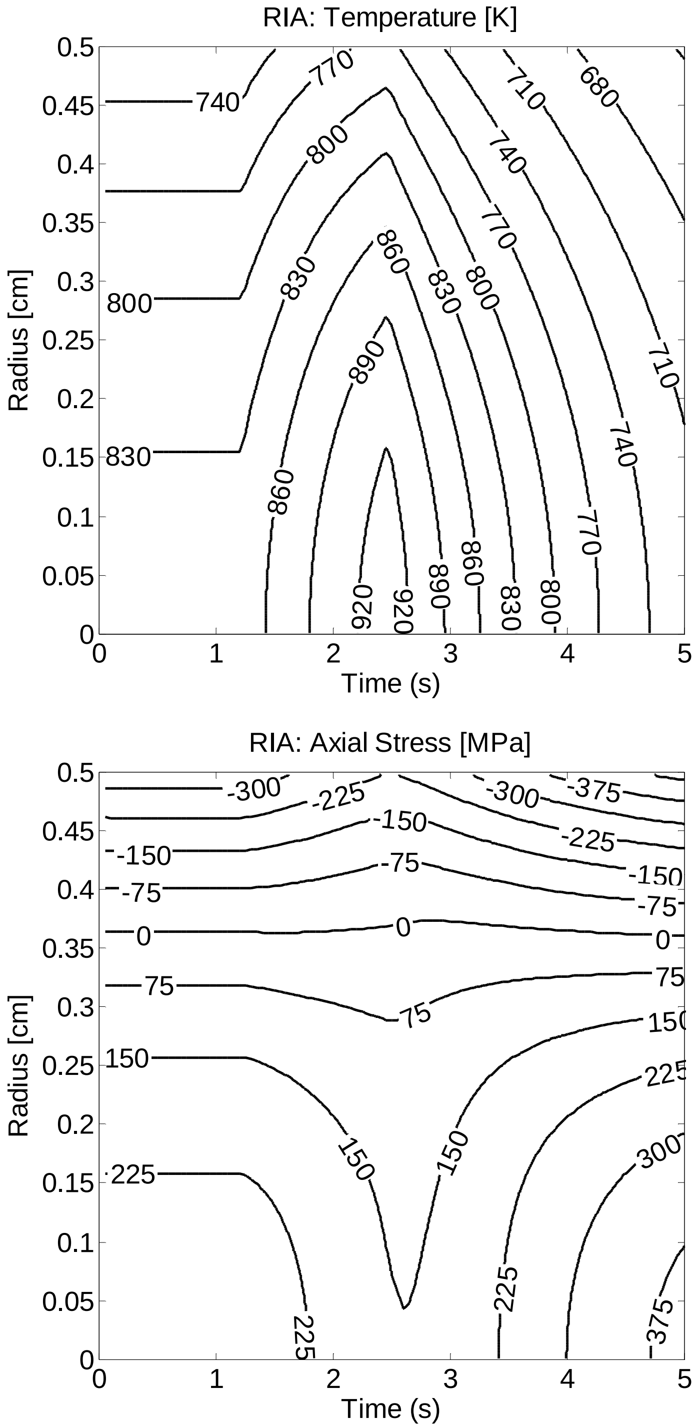

Figure 3.6: Top: Fuel temperature and Bottom: axial-stress response to RIA.

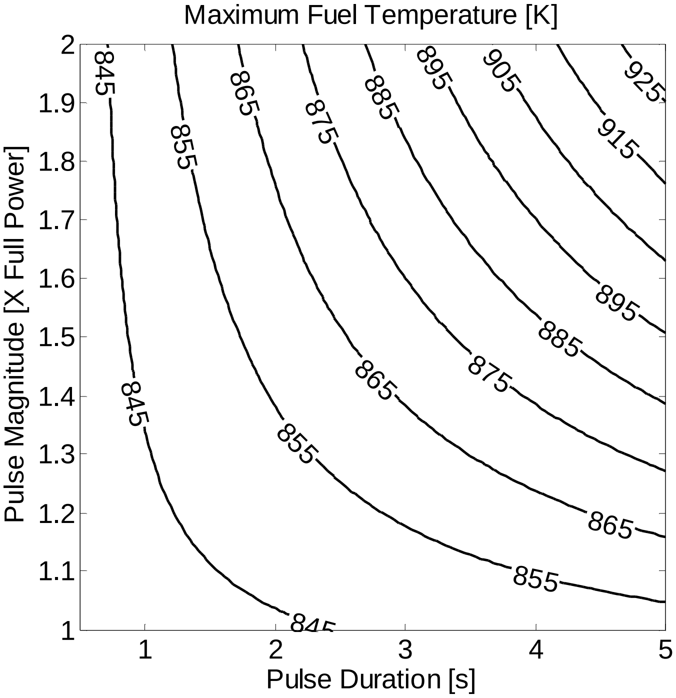

Figure 3.7: Maximum fuel temperature during power pulse.

Table 3.2: Effects of variable-property versus constant-property analysis: relative percent error.

LHR [W/cm]	Maximum temperature (%Δ)	H/Zr at fuel center (%Δ)	H/Zr at fuel surface (%Δ)	Axial stress at fuel center (%Δ)
100	1.11	-0.51	0.55	12
200	2.18	-0.84	0.97	8.73
300	3.19	-1.05	1.29	2.78

3.3.2 Extent and effect of hydrogen desorption

The extent of hydrogen release from the LM-bonded fuel is unknown. However, it is believed to be smaller when compared to the case of a gap filled with helium, in which case hydrogen is readily released from the surface into a much larger volume. For perspective, it is appropriate to study fuel with a He filled gap. The extent of release can then be estimated by the equilibrium partial pressure of hydrogen inside the cladding, which can be expressed as a function of temperature and fuel surface hydrogen concentration according to Wang et al. [70] as:

$$p\,[\text{atm}] = \left(\frac{C_{eq}}{2 - C_{eq}}\right) \exp\left(8.01 + 5.21 C_{eq} - \frac{2.07 \times 10^4}{T\,[\text{K}]}\right) \tag{3.17}$$

The free volume inside the cladding due to the plenum volume and gap is approximately 40 cm^3. Assuming a pre-pressurization to 1 MPa of He, the total pressure in the cladding can be calculated as the sum of partial pressures of hydrogen and helium that in turn obey the ideal gas law. Figure 3.8 shows the equilibrium pressure inside the cladding as function of temperature and H/Zr ratio at the fuel surface. The plenum and gap are conservatively assumed to be at the fuel surface temperature. The amount of hydrogen in each fuel rod is approximately 25 moles [48]. The equilibrium fractional loss as a function of fuel-surface temperature and H/Zr ratio at the fuel surface is also shown in Figure 3.8. Adsorption of hydrogen on the inner surface of cladding and its subsequent diffusion into the cladding is ignored. Over time however, this will result in a larger fractional release of hydrogen into the cladding.

3.3.3 Magnitude and effect of power depression in a fuel pellet

A pin-cell model was built in the MCNP (Monte Carlo N-Particle) transport code to determine the steady-state power profile during the reactor operation so the accuracy of the uniform-power approximation could be addressed (Appendix A). The steady-state temperature and hydrogen concentration results with the uniform power LHR of 300 W/cm were used as input for the cross-sections and number densities of the MCNP model. The power was tallied in 10 radial shells of the fuel. The resultant power profile was used to update the heat and hydrogen diffusion model and the process was iterated until convergence. The normalized power profile for the first iteration is shown in Figure 3.9. The maximum difference between the uniform and depressed power profiles is around 2% and it changes the centerline temperature by 2.25 K, or ~0.8% of the fuel-centerline-to-coolant temperature drop. Its effects on the hydrogen concentration and stresses are even smaller, so the uniform power profile is a good assumption.

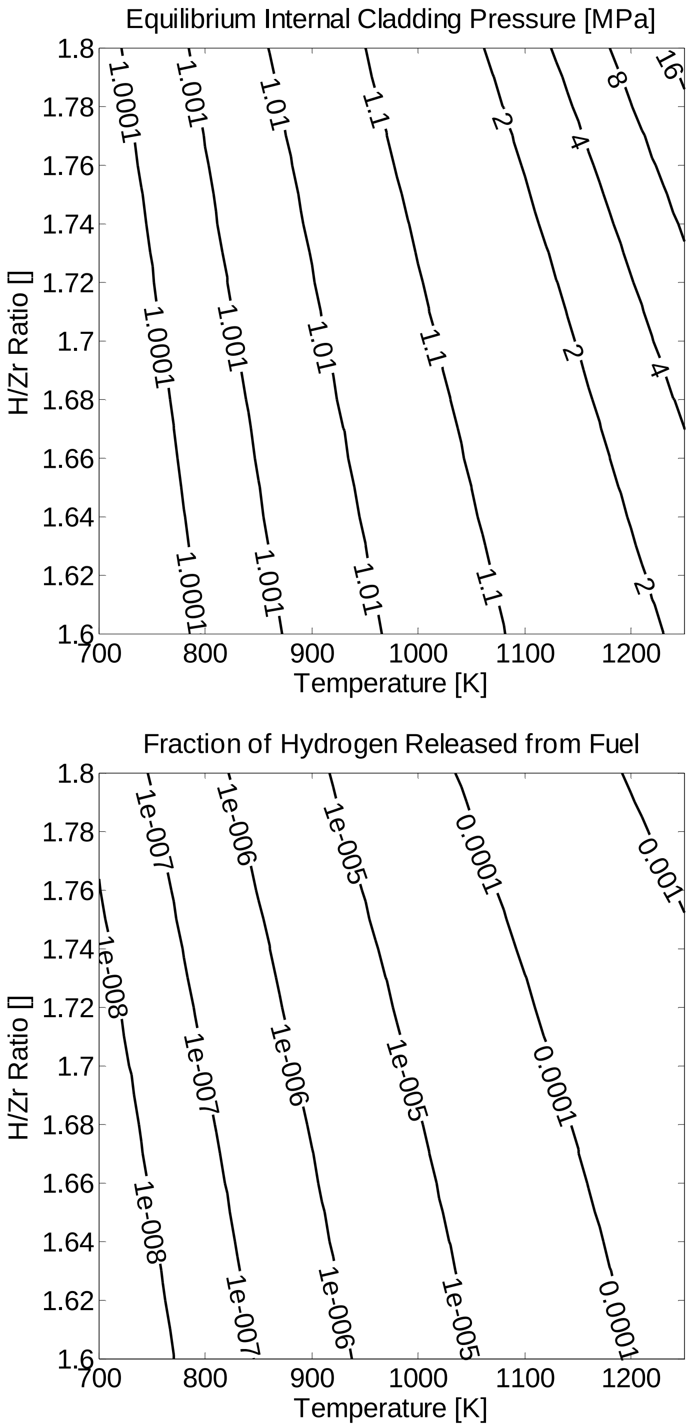

Figure 3.8: Top: Equilibrium total pressure inside the cladding. Bottom: Total fraction of hydrogen inside the fuel lost to the cladding free volume in equilibrium.

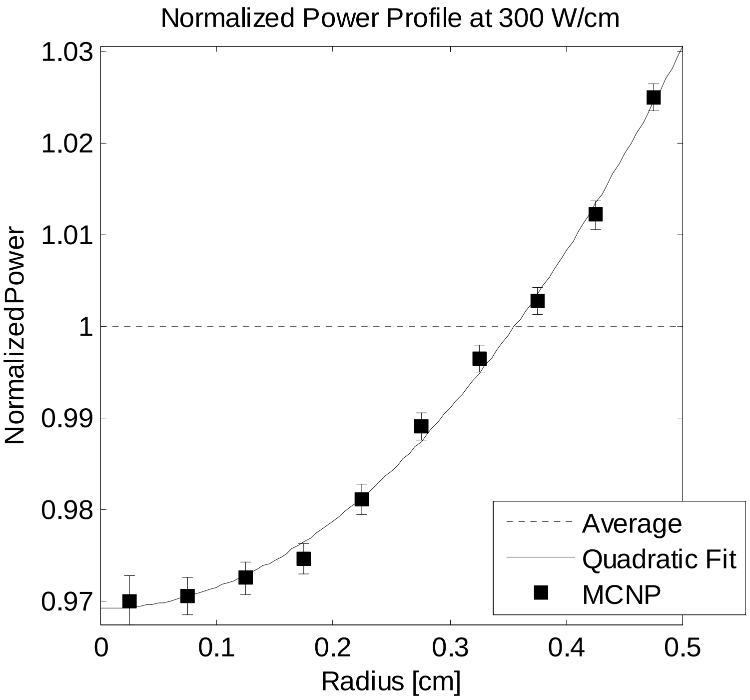

Figure 3.9: Distribution of the power profile across fuel operated at a linear heat rate of 300 W/cm.

3.4 Discretization of differential equations

3.4.1 Heat conduction equation

Radial heat conduction equation with variable properties is described by a non-linear partial differential equation (Equation 3.7). A well known discretization procedure is that of Crank and Nicolson [15], in which time is discretized with the trapezoid rule and space with central difference. This first step is shown below:

$$\begin{gathered}\tfrac{1}{\Delta t}\left[\left(\rho C_p T\right)_i^{j+1} - \left(\rho C_p T\right)_i^{j}\right] = \\ \tfrac{1}{2}\tfrac{1}{r_i \Delta r}\left[\left(rk\tfrac{\partial T}{\partial r}\right)^{j+1}_{r_{i+1/2}} - \left(rk\tfrac{\partial T}{\partial r}\right)^{j+1}_{r_{i-1/2}} + \left(rk\tfrac{\partial T}{\partial r}\right)^{j}_{r_{i+1/2}} - \left(rk\tfrac{\partial T}{\partial r}\right)^{j}_{r_{i-1/2}}\right]\end{gathered} \tag{3.18}$$

where *i* and *j* indicate the radial node and time step, respectively. All terms are considered as node-centered. The equation is expanded and rearranged:

$$\begin{gathered}\left(\rho C_p\right)_i^{j+1} T_i^{j+1} - \left(\rho C_p\right)_i^{j} T_i^{j} = Q\Delta t + \omega\left[\tfrac{r_{i+1/2}}{r_i}k_{i+1/2}^{j+1}\left(T_{i+1}^{j+1} - T_i^{j+1}\right)\right. \\ \left. -\tfrac{r_{i-1/2}}{r_i}k_{i-1/2}^{j+1}\left(T_{i}^{j+1} - T_{i-1}^{j+1}\right) + \tfrac{r_{i+1/2}}{r_i}k_{i+1/2}^{j}\left(T_{i+1}^{j} - T_i^{j}\right) - \tfrac{r_{i-1/2}}{r_i}k_{i-1/2}^{j}\left(T_{i}^{j} - T_{i-1}^{j}\right)\right]\end{gathered} \tag{3.19}$$

where the following terms and notations are defined and used for convenience:

$$Q = \frac{1}{2}\left(\dot{q}_i^{m,j+1} + \dot{q}_i^{m,j}\right) \tag{3.20}$$

$$\omega = \frac{\Delta t}{2\Delta r^2} \tag{3.21}$$

$$k_{i\pm 1/2} = \frac{1}{2}\left(k_{i\pm 1} + k_i\right) \tag{3.22}$$

Since a marching procedure is performed in time, in solving for the $(j+1)$st iterate from the known jth iterate, the thermal conductivity and volumetric heat capacity at the $(j+1)$st time step are not known as they depend on both temperature and hydrogen concentration. Further, the functional dependencies are highly non-linear. Initially, predictor-corrector iterations were performed at each time step, requiring substantial increases in run-time. Newton-Raphson methods were also considered but were deemed too laborious. A final, simpler method that produces results with essentially no difference is a first-order Taylor extrapolation of the material properties using the jth and $(j-1)$st values. This procedure is outlined below:

$$k^{j+1} \approx k^j + \Delta t\frac{k^j - k^{j-1}}{\Delta t} = 2k^j - k^{j-1} \tag{3.23}$$

$$\left(\rho C_p\right)^{j+1} \approx 2\left(\rho C_p\right)^{j} - \left(\rho C_p\right)^{j-1} \tag{3.24}$$

The node-centered radius terms are also expanded accordingly:

$$r_i = \Delta r\left(i - \frac{1}{2}\right) \tag{3.25}$$

$$\frac{r_{i\pm 1/2}}{r_i} = \frac{r_i \pm \frac{\Delta r}{2}}{r_i} = 1 \pm \frac{\Delta r}{2r_i} = 1 \pm \frac{\Delta r}{2\Delta r\left(i - \frac{1}{2}\right)} = 1 \pm \frac{1}{2i - 1} \tag{3.26}$$

Utilizing these enhancements, the final form of the semi-implicitly discretized heat equation is acquired:

$$\begin{gathered}\left\{\begin{array}{l} T_i^{j+1}\left[\frac{\left(\rho C_p\right)_i^{j+1}}{\omega} + \left(1 + \frac{1}{2i-1}\right)k_{i+1/2}^{j+1} + \left(1 - \frac{1}{2i-1}\right)k_{i-1/2}^{j+1}\right] \\ T_{i+1}^{j+1}\left[-\left(1 + \frac{1}{2i-1}\right)k_{i+1/2}^{j+1}\right] + T_{i-1}^{j+1}\left[-\left(1 - \frac{1}{2i-1}\right)k_{i-1/2}^{j+1}\right] \end{array}\right\} \\ = \left\{\begin{array}{l} T_i^{j}\left[\frac{\left(\rho C_p\right)_i^{j}}{\omega} - \left(1 + \frac{1}{2i-1}\right)k_{i+1/2}^{j} - \left(1 - \frac{1}{2i-1}\right)k_{i-1/2}^{j}\right] \\ T_{i+1}^{j}\left[\left(1 + \frac{1}{2i-1}\right)k_{i+1/2}^{j}\right] + T_{i-1}^{j}\left[\left(1 - \frac{1}{2i-1}\right)k_{i-1/2}^{j}\right] \end{array}\right\} + \frac{Q\Delta t}{\omega}\end{gathered} \tag{3.27}$$

3.4.2 Hydrogen diffusion equation

The hydrogen mass balance equation can be written for a differential radial shell in terms of the flux within the fuel as the following:

$$c_i^{j+1} = c_i^{j} + \left[J_{i-1/2}^{j} S_{i-1/2} - J_{i+1/2}^{j} S_{i+1/2}\right] \tag{3.28}$$

where c is the molar concentration of hydrogen in mole H/cm^3; J is the hydrogen atom flux specified earlier in Equation 3.10. S is the ratio of inner/outer surface of each radial shell to its volume with units of cm^{-1}:

$$S_{i\pm 1/2} = \frac{2\pi r_{i\pm 1/2} l}{\pi\left(r_{i+1/2}^2 - r_{i-1/2}^2\right) l} = \frac{2\left(r_i \pm \frac{\Delta r}{2}\right)}{\left(\left[\left(r_i + \frac{\Delta r}{2}\right)\right]^2 - \left[\left(r_i - \frac{\Delta r}{2}\right)\right]^2\right)} \tag{3.29}$$

After substituting Equation 3.26 and simplifying, Equation 3.29 becomes:

$$S_{i\pm 1/2} = \frac{2\left(r_i \pm \frac{\Delta r}{2}\right)}{\left(2r_i\Delta r\right)} = \frac{r_i \pm \frac{\Delta r}{2}}{r_i \Delta r} \xrightarrow{r_i = \Delta r\left(i - \frac{1}{2}\right)} \left\{\begin{array}{l} - \longrightarrow \frac{i-1}{\Delta r\left(i - \frac{1}{2}\right)} \\ + \longrightarrow \frac{i}{\Delta r\left(i - \frac{1}{2}\right)} \end{array}\right. \tag{3.30}$$

The hydrogen-to-zirconium atomic ratio is:

$$C_i^j = \frac{M_{Zr}}{\rho_{Zr}} c_i^j \tag{3.31}$$

where M_{Zr} is the atomic mass of zirconium. Substituting for Equations 3.30, 3.31, and 3.10, Equation 3.28 generates the following result:

$$\begin{aligned} C_i^{j+1} \tfrac{\rho_{Zr}}{M_{Zr}} = C_i^j \tfrac{\rho_{Zr}}{M_{Zr}} + \Bigg[-D_{i-1/2}^j \tfrac{\rho_{Zr}}{M_{Zr}} \left(\tfrac{C_i^j - C_{i-1}^j}{r_i - r_{i-1}} + \tfrac{T_Q C_{i-1/2}^j}{T_{i-1/2}^2} \tfrac{T_i - T_{i-1}}{r_i - r_{i-1}} \right) \tfrac{i-1}{\Delta r \left(i - \frac{1}{2} \right)} \\ - D_{i+1/2}^j \tfrac{\rho_{Zr}}{M_{Zr}} \left(\tfrac{C_{i+1}^j - C_i^j}{r_{i+1} - r_i} + \tfrac{T_Q C_{i+1/2}^j}{T_{i+1/2}^2} \tfrac{T_{i+1} - T_i}{r_{i+1} - r_i} \right) \tfrac{i}{\Delta r \left(i - \frac{1}{2} \right)} \Bigg] \Delta t \end{aligned} \tag{3.32}$$

Further simplification of the above results in the fully explicit discretization for H/Zr ratio as:

$$\begin{aligned} C_i^{j+1} = C_i^j \Bigg[1 - 0.9 \tfrac{\Delta t}{\Delta r^2} D_{i+1/2}^j \tfrac{i}{\left(i - \frac{1}{2} \right)} \left(1 - \frac{T_Q \left(T_{i+1}^j - T_i^j \right)}{\left(T_{i+1/2}^j \right)^2} \right) \\ - 0.9 \tfrac{\Delta t}{\Delta r^2} D_{i-1/2}^j \tfrac{i-1}{\left(i - \frac{1}{2} \right)} \left(1 - \frac{T_Q \left(T_i^j - T_{i-1}^j \right)}{\left(T_{i-1/2}^j \right)^2} \right) \Bigg] \\ + C_{i+1}^j \left[0.9 \tfrac{\Delta t}{\Delta r^2} D_{i+1/2}^j \tfrac{i}{\left(i - \frac{1}{2} \right)} \left(1 - \frac{T_Q \left(T_{i+1}^j - T_i^j \right)}{\left(T_{i+1/2}^j \right)^2} \right) \right] \\ + C_{i-1}^j \left[0.9 \tfrac{\Delta t}{\Delta r^2} D_{i-1/2}^j \tfrac{i-1}{\left(i - \frac{1}{2} \right)} \left(1 - \frac{T_Q \left(T_i^j - T_{i-1}^j \right)}{\left(T_{i-1/2}^j \right)^2} \right) \right] \end{aligned} \tag{3.33}$$

3.4.3 Stress equations

Equation 3.15 for the radial stress is first discretized with central difference:

$$\begin{aligned} \tfrac{1}{r_i^2} \tfrac{1}{\Delta r} \left(r^3 \left. \tfrac{d\sigma_r}{dr} \right|_{r_{i+1/2}} - r^3 \left. \tfrac{d\sigma_r}{dr} \right|_{r_{i-1/2}} \right) = \\ \tfrac{-E}{1-\nu} \left[\tfrac{1}{\Delta r} \left(\alpha T|_{r_{i+1/2}} - \alpha T|_{r_{i-1/2}} \right) + \beta \tfrac{C_{i+1/2} - C_{i-1/2}}{\Delta r} \right] \end{aligned} \tag{3.34}$$

Utilizing Equations 3.25 and 3.26 and taking into account the linearly-temperature-dependent coefficient of thermal expansion, Equation 3.35 becomes:

$$\begin{gathered}\sigma_{r,i}\left[-i\left(1+\tfrac{1}{2i-1}\right)^2-(i-1)\left(1+\tfrac{1}{2i-1}\right)^2\right]\\+\sigma_{r,i+1}\left[i\left(1+\tfrac{1}{2i-1}\right)^2\right]+\sigma_{r,i-1}\left[i\left(1-\tfrac{1}{2i-1}\right)^2\right]\\=\tfrac{-E}{1-\nu}\left[\alpha_{\circ}\left(\left[T_{i+1/2}-T_{i-1/2}\right]+a\left[T^2_{i+1/2}-T^2_{i-1/2}\right]\right)+\tfrac{\beta}{2}\left(C_{i+1}-C_{i-1}\right)\right]\end{gathered} \tag{3.35}$$

With the boundary conditions described in Section 3.15, Equation 3.35 can be solved in the matrix form, obtaining the radial stress across the fuel. The azimuthal stress across the fuel is then determined by Equation 3.6 with the condition of radially symmetric stress applied:

$$\sigma_{\theta,i}=\frac{1}{2}\left[i\left(\sigma_{r,i+1}+\sigma_{r,i}\right)-(i-1)\left(\sigma_{r,i}+\sigma_{r,i-1}\right)\right] \tag{3.36}$$

As discussed in Section 3.1.5 the axial stress is defined as the difference between the actual to the mean of the restrained axial stress (such that $\varepsilon_z = 0$), as shown in Equation 3.37.

$$\sigma_{z,i}=\sigma^R_{z,i}-\bar{\sigma}^R_{z,i} \tag{3.37}$$

The actual and mean of the restrained axial stress are found as shown in Equations 3.38 and 3.39. The reference temperature was taken as 750 K, corresponding to the typical fuel fabrication temperatures, during which the material is assumed to be free of residual stresses. The reference value of H/Zr ratio is 1.6.

$$\sigma^R_{z,i}=\nu\left(\sigma_{\theta,i}+\sigma_{r,i}\right)-E\left[\alpha_{\circ}\left(\left[T_i-aT_i^2\right]-\left[T_{ref}-aT^2_{ref}\right]\right)+\beta\left(C_i-C_{ref}\right)\right] \tag{3.38}$$

$$\bar{\sigma}^R_{z,i}=\frac{2}{R^2}\int_0^R r\sigma^R_{z,i}dr=\frac{2}{R^2}\sum_{i=1}^{m}\left(i-\frac{1}{2}\right)\sigma^R_{z,i}\Delta r^2 \tag{3.39}$$

3.5 Conclusions

Steady-state and transient behavior of several aspects of fuel-operating performance have been investigated, taking into account the temperature- and hydrogen-concentration dependence of the fuel properties.

Steady-state temperature, hydrogen concentration, and stress profiles of the hydride fuel operated at various linear heat rates have been calculated. The extent of hydrogen redistribution, driven by the temperature gradient, becomes more severe as the power increases. Strains in the fuel occur from thermal and hydrogen concentration gradients, with the latter being the dominant contributor. Axial and azimuthal stresses are both compressive at the surface and tensile at the fuel centerline. These results are in agreement with what was previously shown by Olander [48], where the dependence of fuel properties (except the coefficient of thermal expansion) on temperature and hydrogen concentration were ignored. The fuel fracture criterion is unknown and needs be determined through finite element methods.

The transient response of hydride fuel to a reactivity insertion accident scenario was studied by pulsing the power in a square wave. The thermal response of the fuel to the changing boundary conditions is very rapid (on order of few seconds) due to the small fuel rod and large thermal diffusivity. There is no discernable alteration in the transient hydrogen profile, since the characteristic diffusion time for these length scales is many orders of magnitude larger than the transient durations. However, it is necessary to model the hydrogen diffusion since it is important to know the steady-state distribution for the initial conditions. Surprisingly, the stress across the fuel is actually reduced during the power pulse. The temperature-induced stresses counteract the hydrogen-induced stresses, so the fuel is in its most relaxed state during this stage of the transient. The fuel experiences maximum stress when temperature gradients diminish but the hydrogen displacement remains at the pre-transient distribution.

The flux of hydrogen atoms out of the fuel, in a fuel assembly with a He filled gap, during steady state and transient operation of the fuel is very small since the net rate (desorption – adsorption) quickly becomes zero when the equilibrium hydrogen partial pressure is established. The pressure buildup inside the cladding and the total fraction of hydrogen lost from the solid state to the cladding volume are negligible even at very high fuel surface temperatures. The extent of dehydriding is expected to be even less for LM-bonded fuels.

Chapter 4

The Kinetics of Hydrogen Desorption from and Adsorption on Zirconium Hydride

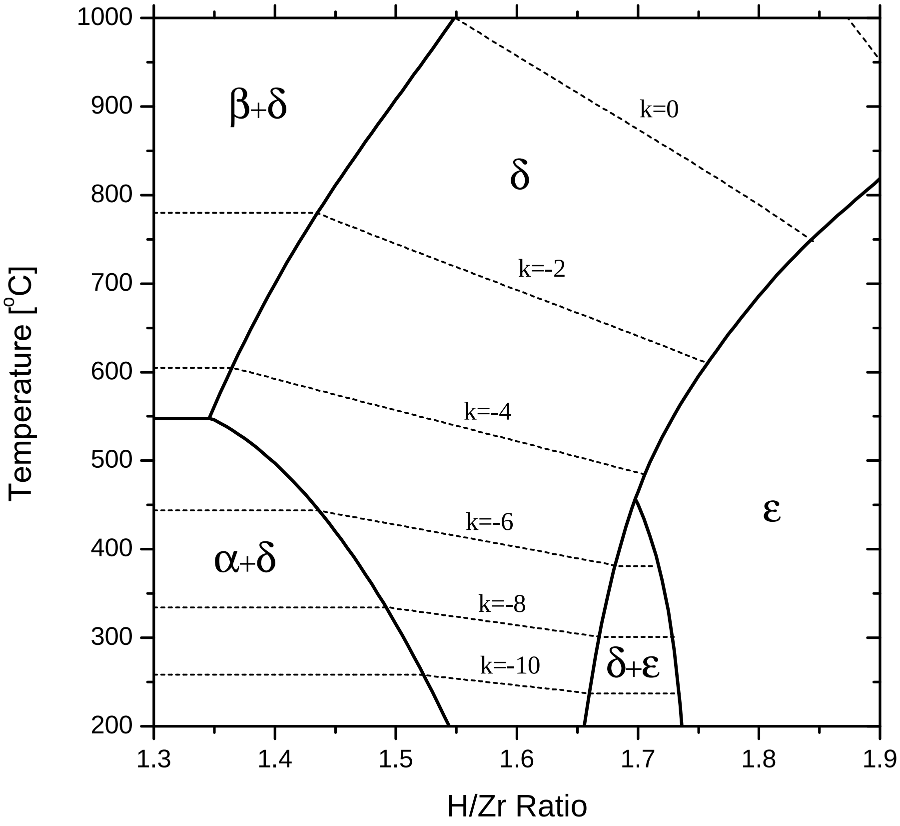

Figure 4.1: Phase Diagram for Zirconium-Hydrogen System [4] with equilibrium H_2 isobars labeled as $p_{H_2} = 10^k$ [MPa].

Hydride fuel is produced by contacting U-Zr alloys (~ 45 wt % U) with hydrogen gas at high temperature. Other alloy compositions containing thorium or minor actinides are also possible hydride fuels. In case of the U-Zr hydride fuel, controlling the hydrogen pressure during fabrication establishes the H/Zr ratio (typically 1.6). The resulting microstructure consists of micron-size metallic uranium particles dispersed in a matrix of zirconium hydride. The Zr-H phase diagram is well-established, as is the equilibrium hydrogen pressure as a function of temperature and H/Zr ratio (Equation 4.1) [70]. In Equation 4.1, C is the hydrogen-to-zirconium ratio.

$$p\,[\mathrm{MPa}] = \left(\frac{C}{2-C}\right)\exp\left(5.72 + 5.21C - \frac{172\,\left[\mathrm{kJmol^{-1}}\right]}{T\,[\mathrm{K}]}\right) \tag{4.1}$$

Figure 4.1 indicates that substantial hydrogen pressures can be generated if the fuel is driven to high temperatures (> ~800 °C) in a transient, as was discussed in Chapter 3. This in turn can release H_2 to the gap and the plenum, with several adverse consequences: i) overpressurization of the fuel rod; ii) permeation of hydrogen through the cladding (Zircaloy); iii) hydrogen embrittlement of the cladding. Although the thermodynamic driving force for hydrogen loss from the zirconium hydride matrix in the fuel at high temperature exists, the kinetics of the process is unknown. The purpose of the present work is to report the results of several experiments bearing on the kinetics of the dehydriding process. All the results presented here pertain to the cubic δ-$ZrH_{1.6\pm x}$ phase [10].

4.1 Experimental setups

Three independent experiments yielding information on the dehydriding process were conducted. The first method involved measurement of hydrogen gas pressure-buildup in a closed vessel as the dehydriding reaction proceeded. The other two experiments, although independent, were conducted using thermogravimetric analysis (TGA) setups, which measured the rate of mass loss while dehydriding took place.

4.1.1 Pressure-buildup experiments

The rate of pressure increase inside a closed system due to dehydriding of zirconium hydride was measured in the experimental setup shown in Figure 4.2.

A small disk of 99.9% purity zirconium metal (1.0 mm thick, 13.5 mm diameter) was cleaned by mechanical polishing and alcohol rinsing. The specimen was placed inside a 316 stainless-steel vessel that was then welded shut. After attaching a pressure transducer and a valve leading to a gas/vacuum management system, the vessel was placed in a furnace. The initial step in the experiment involved in situ production of hydride from the metal disk. The zirconium disk was heated to 750 – 920 °C in an H_2 atmosphere. The stoichiometry was controlled according to Equation 4.1 by adjustment of the temperature and pressure. Upon hydriding volume expansion increased the dimensions of the specimen by ~ 4%.

The sample initially underwent hydriding at 881 °C under 0.34 MPa hydrogen gas pressure for one hour. After each subsequent dehydriding step, the duration of hydriding at a different temperature was established by a rough diffusion analysis on the same specimen. The length of the hydrogen diffusion path is the half thickness of the specimen ($\frac{l}{2}$). The diffusion coefficient of hydrogen in the δ-zirconium hydride reported by Majer et al. [39] is 2.1×10^{-10} m^2/s at 800 °C and 3.7×10^{-10} m^2/s at 900 °C. The characteristic diffusion time, defined as $\frac{l^2}{D}$, at these two temperatures is 20 and 11 minutes, respectively. 30 minutes of hydriding time was used to fabricate hydrides of uniform hydrogen concentration at each temperature. The final dimensions of the hydride disks were 1.04 mm in thickness and 14.0 mm in diameter.

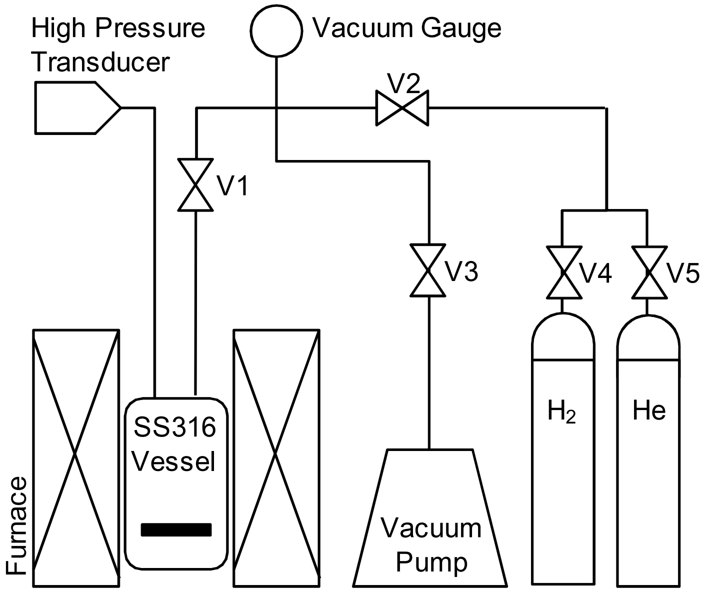

Figure 4.2: Experimental setup for pressure-buildup measurements.

After the uniform hydriding was achieved across the sample, the system was quickly pumped down to vacuum and then isolated by valving off the vessel. Subsequently, the rise in pressure from vacuum due to dehydriding was monitored by a high-pressure transducer connected to the vessel. The volume of the vessel and the connecting tubing up to valve V1 and the interior of the pressure transducer was 1.95×10^{-5} m^3. The system was designed with minimal volume in order to achieve accurate pressure-change measurements. Hydriding and dehydriding were performed in sequence at constant temperature.

A minor complication with this technique is the permeability of the stainless steel wall of the vessel to hydrogen. The leakage rate of hydrogen from the vessel can be written as shown in Equation 4.2, where $\Phi_\circ$ and H_Φ are the pre-exponential and activation energy of the permeation process, respectively.

$$R_{leak} = \Phi_\circ \frac{1}{\delta}\sqrt{p}\exp\left(\frac{-H_\Phi}{RT}\right) \tag{4.2}$$

δ is the thickness of the vessel wall. Permeation of hydrogen through stainless steel has been extensively studied [42] and the activation energy is reported as 60 kJ/mol. The permeation rate was determined from the rate of pressure drop, using a vessel filled with hydrogen gas but no hydride specimen at different temperatures. The pre-exponential term and activation energy were determined as 1.1×10^{-4} mol H_2/ m.s.$MPa^{½}$ and 53 kJ/mol, respectively. As shown in Figure 4.3, these results are in good agreement with literature values.

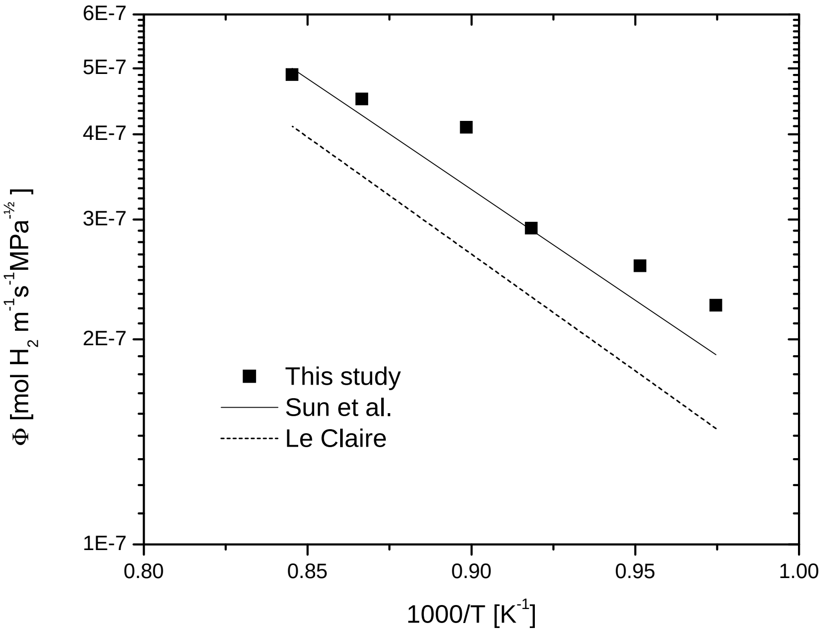

Figure 4.3: Leakage rate (permeation) of hydrogen through the stainless steel vessel as a function of temperature [37, 62].

4.1.2 Thermogravimetric experiments

Two separate TGA experiments were conducted, one at Univ. of California, Berkeley California [26] (on zirconium samples) and another at Chulalongkorn Univ., Bangkok, Thailand (on Zircaloy specimens). In both cases a microbalance was utilized to measure changes in sample weight as a function of time. The samples for the Berkeley experiment were initially polished and pickled in a solution of 50 vol% water, 45 vol% 16M nitric acid and 5 vol% 28 M hydrofluoric acid for two minutes. Specimens were then hung using a tungsten-rhenium wire into a quartz tube with controlled atmosphere, where temperatures up to 810 °C were attainable. The samples were first heated under vacuum then hydrided in a hydrogen atmosphere. The pre-dehydriding H/Zr ratio was fixed by controlling the temperature and hydrogen gas pressure, and was verified by the mass gain. Then, while at constant temperature, a vacuum on the order of 10^{-3} Pa was induced and maintained inside the quartz tube. The rate of hydrogen desorption was determined by measuring the weight-loss rate. The second set of thermogravimetric experiments was performed using hydrided Zircaloy-2 tubes under similar conditions and experimental procedures.

4.2 Results and analysis

4.2.1 Pressure-buildup experiments

A typical graph showing the rise in pressure as a function of time for the first 6 minutes during dehydriding is presented in Figure 4.4. The rise in pressure is rapid and reaches equilibrium in a matter of minutes.[1] Experiments were performed at 13 different temperatures and starting H/Zr ratios (Table 4.1). Pre- and post-dehydriding hydrogen gas pressures are also given in Table 4.1. The H/Zr ratios were calculated by substituting the steady-state hydrogen pressures into Equation 4.1.

Conservation of mass at the surface of the hydride disk requires that the net rate of H_2 desorption equals the hydrogen atom flux to the surface by diffusion (Equation 4.3). The term taking into account the change in the hydrogen stored at the surface layer is ignored since it is many orders of magnitudes smaller than the other two. The rate of hydrogen gas accumulation inside the vessel is due to H_2 adsorption and desorption from the hydride and to the rate at which the hydrogen leaks from the vessel (Equation 4.4 and Figure 4.5).

$$\frac{1}{2} R_{diff}\Big|_{x=\frac{1}{2}} = R_{des} - R_{ads} \tag{4.3}$$

---

[1] Due to the limited temporal range shown in Figure 4.4, some of the curves have not leveled off completely. However, during the experiment enough time was permitted for equilibrium conditions to establish.

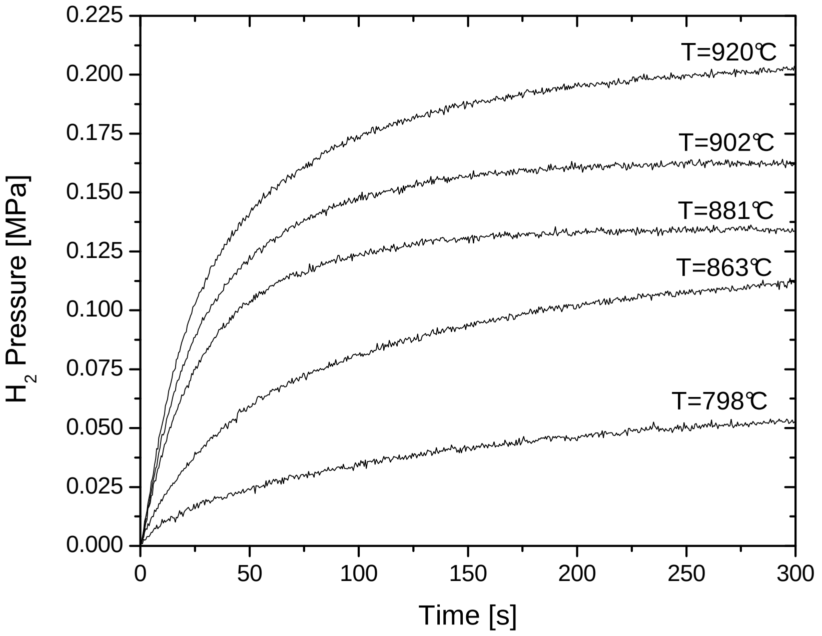

Figure 4.4: Typical results corresponding to accumulation of hydrogen gas inside the vessel as a function of time.

Table 4.1: Experimental conditions and details.

	Pre Dehydriding		Post Dehydriding	
Temperature [°C]	H2 Pressure [MPa]	H/Zr Ratio	H2 Pressure [MPa]	H/Zr Ratio
743	0.042	1.632	0.016	1.546
770	0.092	1.654	0.039	1.579
798	0.294	1.704	0.066	1.581
800	0.464	1.735	0.075	1.589
829	0.222	1.639	0.083	1.553
830	0.454	1.694	0.091	1.560
852	0.412	1.658	0.118	1.550
859	0.147	1.560	0.089	1.512
863	0.433	1.648	0.124	1.538
880	0.457	1.630	0.137	1.522
881	0.341	1.603	0.142	1.524
902	0.447	1.599	0.166	1.508
920	0.457	1.578	0.217	1.508

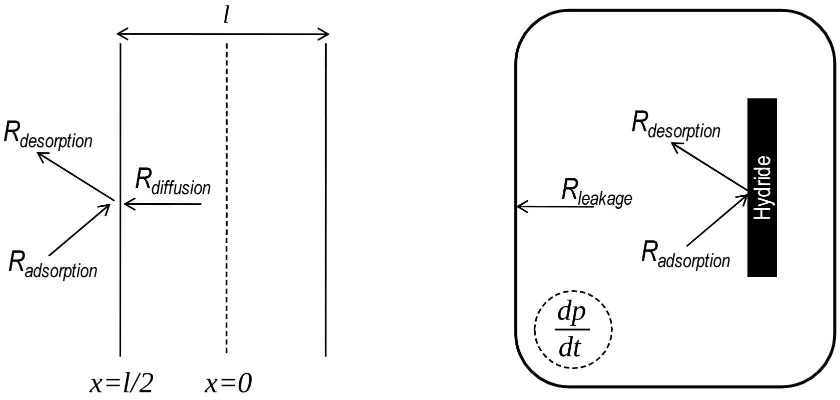

Figure 4.5: Conservation of hydrogen: Left: at the hydride surface Right: inside the vessel.

$$\frac{V}{RT}\frac{dp}{dt} = \left(R_{des} - R_{ads}\right) S_d - \frac{1}{2} R_{leak} S_v \tag{4.4}$$

The diffusion and leakage terms in the above equations are divided by a factor of 2 since they correspond to flux of hydrogen atoms and the rates of adsorption and desorption correspond to that of hydrogen gas. V, R, T, S_d, and S_v are vessel volume (1.95×10^{-5} m^3), gas constant, temperature, disk surface area (3.56×10^{-4} m^2), and vessel surface area ($\sim1.6\times10^{-3}$ m^2), respectively. The left hand side of Equation 4.4 is experimentally measured. The leakage term is also known since it was measured in Section 4.1.1. At each time, the slope $\frac{dp}{dt}$ was read from the curves in Figure 4.4 and input to Equation 4.5. Subsequently the flux (net rate of desorption) at the hydride surface as a function of time, corrected for hydrogen leakage from the vessel, could be calculated using experimental data. The actual pressures measured as a function of time (not corrected for leakage) were input to R_{leak} since they represent the actual driving force.

$$J_{des} = \frac{1}{S_d}\left(\frac{V}{RT}\frac{dp}{dt} + \frac{1}{2} R_{leak} S_v\right) \tag{4.5}$$

Figure 4.6 shows the net rate of hydrogen desorption from the surface as a function of hydrogen gas pressure (rather than time). The linearity of these plots indicates that the H_2 desorption flux can be described by an equation of the form:

$$J_{des} = K\left(p_{eq} - p\right) \tag{4.6}$$

where p_{eq} is the equilibrium pressure (Table 4.1) and K is a constant.

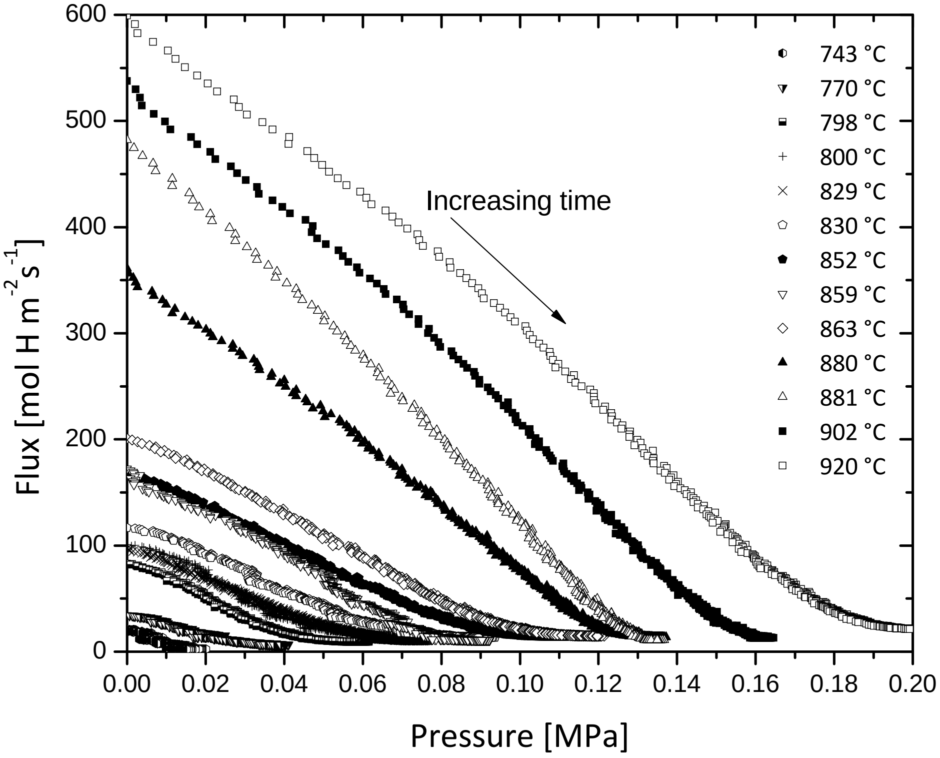

Figure 4.6: Evolution of the net hydrogen flux versus hydrogen gas pressure in the vessel during the dehydriding process.

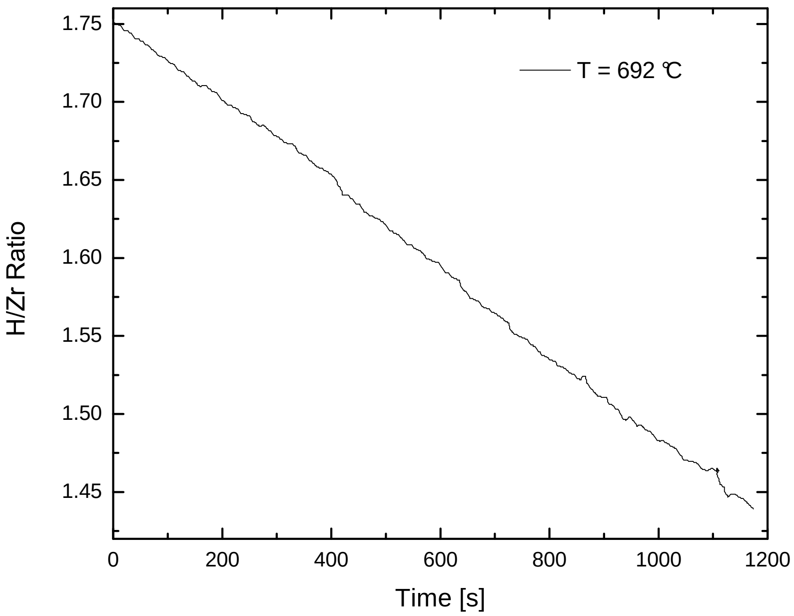

Figure 4.7: Reduction of the H/Zr ratio determined from mass loss of hydrided zirconium at 692 °C.

4.2.2 Thermogravimetric experiments

A typical graph showing the change in the hydride content as function of time during the TGA (thermogravimetric analysis) is shown in Figure 4.7 for the experiments performed on zirconium samples. The rate of mass loss is constant over a considerable extent of the δ-$ZrH_{1.6\pm x}$ region. Very similar results with linear mass-loss behavior were observed in the Zircaloy TGA experiments.

4.2.3 Analysis of the experimental data

The surface reaction obeys zeroth order kinetics, as no influence of surface concentration on the rate of dehydriding is observed. Figures 4.6 and 4.7 clearly show concentration-independent rate constants for both the desorption and adsorption processes.

Inapplicability of second order surface kinetics and the evidence of change in surface hydrogen concentration during the dehydriding process is discussed in 4.3.1. Section 4.3.2 outlines the steps taken to investigate the possibility of bulk diffusion limited kinetics and its invalidity for this case. The lack of dependence of the rate of mass loss on the H/Zr ratio is a characteristic of a zeroth-order desorption process. When coupled to an adsorption step that obeys first-order kinetics, the net desorption flux is expressed by:

$$J_{des} = R_{des} - R_{ads} = k_{des} - k_{ads} p \tag{4.7}$$

Equation 4.7 has the same form as Equation 4.6, from which the rate constants are identified as:

$$k_{des} = K p_{eq} \qquad k_{ads} = K \tag{4.8}$$

The K values obtained from linear fits to the lines in Figure 4.6 provide the two rate constants as functions of temperature. From the pressure-buildup experiments in Figure 4.8, the desorption rate constants from all three experiments (pressure-buildup, two TGA) are plotted in Arrhenius fashion. The agreement among the three data sets is excellent. The desorption rate constant was determined through a linear fit and is presented along with the standard error in regression as:

$$k_{des} \left[\mathrm{mol\,H.m^{-2}s^{-1}} \right] = \exp\left(27.0 \pm 0.9 + \frac{-205 \pm 8 \left[\mathrm{kJ.mol^{-1}} \right]}{RT\,[\mathrm{K}]} \right) \tag{4.9}$$

where the activation energy is in kJ/mol and T is in Kelvin. Based on the pressure buildup data, Figure 4.9 depicts the adsorption rate constant as a function of temperature where k_{ads} is expressed by:

$$k_{ads} \left[\mathrm{mol\,H.m^{-2}s^{-1}MPa^{-1}} \right] = \exp\left(16.7 \pm 1.6 + \frac{-86 \pm 15 \left[\mathrm{kJ.mol^{-1}} \right]}{RT\,[\mathrm{K}]} \right) \tag{4.10}$$

4.3 Discussion

Zeroth-order desorption kinetics is rare, but not unknown. Bienfait and Venables have reported this behavior for xenon adsorbed on 0001 graphite planes [69]. The same order kinetics has been reported for desorption of O_2 from oxide films on tungsten [34]. In both cases desorption leaves behind an identical layer of the material (adsorbate in case of xenon and substrate in case of tungsten oxide). However, the current system is different because the desorbing gas is supplied to the surface by diffusion in the substrate solid. Throughout the dehydriding process the hydrogen concentration in the bulk, which feeds the surface hydrogen, is constantly reduced.

A more relevant system is hydrogen on nickel and iron films, for which zeroth-order desorption kinetics was observed [53, 54]. This behavior was attributed to a

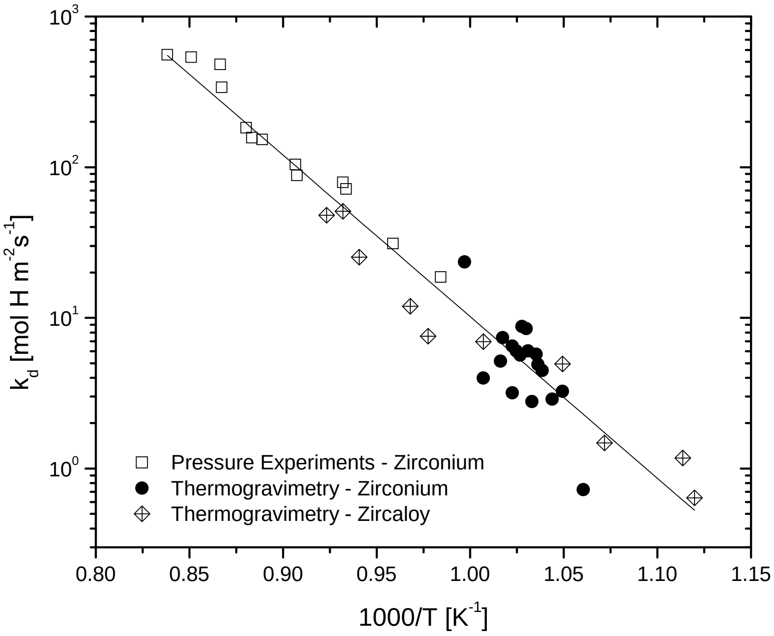

Figure 4.8: Arrhenius dependence of the desorption rate constant.

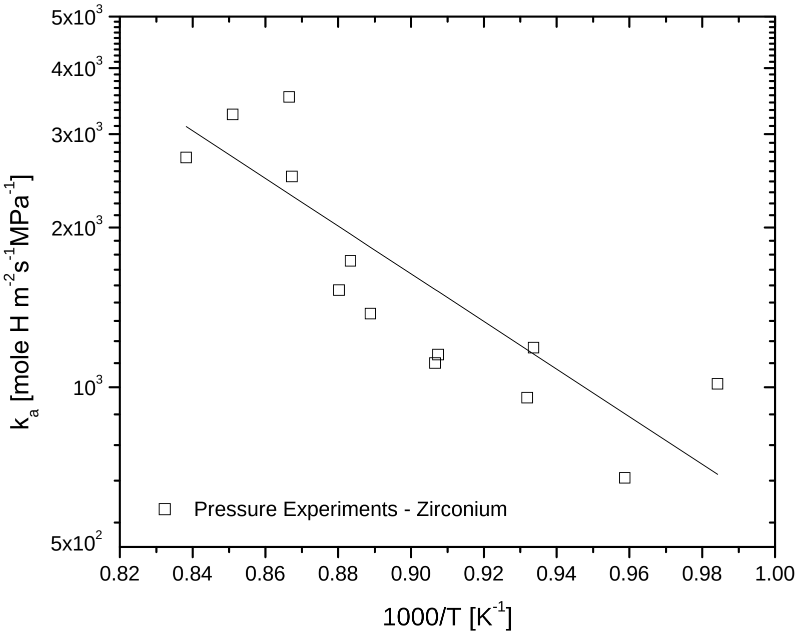

Figure 4.9: Arrhenius dependence of the adsorption rate constant determined from the pressure-buildup experiments.

precursor state of molecular hydrogen on the surface that ultimately controls the desorption rate. However, the applicability of this mechanism to the current system is questionable. The desorption activation energy of 205 kJ/mol in Equation 4.9 is much larger than the values reported in the above-mentioned studies (~25 kJ/mol) for a hydrogen molecule in a precursor state on the surface to overcome the barrier to desorption. A more likely rate-controlling step is the recombination of H atoms on the surface to form H_2, a step that requires rupture of zirconium-hydrogen bonds (Equation 4.11).

$$2\left(Zr-H\right) \xrightarrow{k_{des}} 2Zr + H_2 \tag{4.11}$$

Calorimetric experiments give the enthalpy of formation of zirconium hydride as 160 kJ/mol [21]; the magnitude of which is consistent with the measured activation energy for desorption. For this mechanism to exhibit zeroth order kinetics, the atomic adsorption sites at the surface need to be saturated. High concentration of hydrogen atoms in the bulk along with their significant mobility at high temperatures make it plausible to assume saturation of the surface sites during hydrogen desorption. Consequently this implies that the bulk-to-surface, and gas-to-surface transfer processes are fast, and the overall process is bottlenecked by the surface-recombination step. This mechanism permits establishment of a constant atomic hydrogen concentration on the surface even in the presence of desorption as H_2. Yet the above mechanism cannot hold throughout the entire process, since ultimately thermodynamic equilibrium relationship between the hydrogen gas and the hydride presented in Equation 4.1 is violated. At equilibrium the rates of desorption and adsorption are equal and therefore the net flux at the surface is zero. Setting $k_{des} = k_{ads} p_{eq}$ at equilibrium we can derive the equilibrium pressure as:

$$p_{eq}\,[\mathrm{MPa}] = 3.0 \times 10^{4} \exp\left(\frac{-119\,\left[\mathrm{kJmol}^{-1}\right]}{T\,[\mathrm{K}]}\right) \tag{4.12}$$

Equation 4.12, derived from the kinetic data, is compared to the equilibrium hydrogen pressure from Equation 4.1 in Figure 4.10.

A possible explanation for the difference between the two lines is the failure of the zeroth-order kinetic model as equilibrium is approached. Therefore the rate-limiting step at conditions close to equilibrium conditions described in Equation 4.1 is unknown and its dependence on hydrogen concentration does not obey the zeorth-order kinetics.

4.3.1 Inapplicability of second-order surface kinetics

Langmuir [36] initially proposed the simplified model describing the surface adsorption and desorption processes involved. Since then the theory has developed and extended significantly to describe a much larger range of surface phenomenon [6]. In

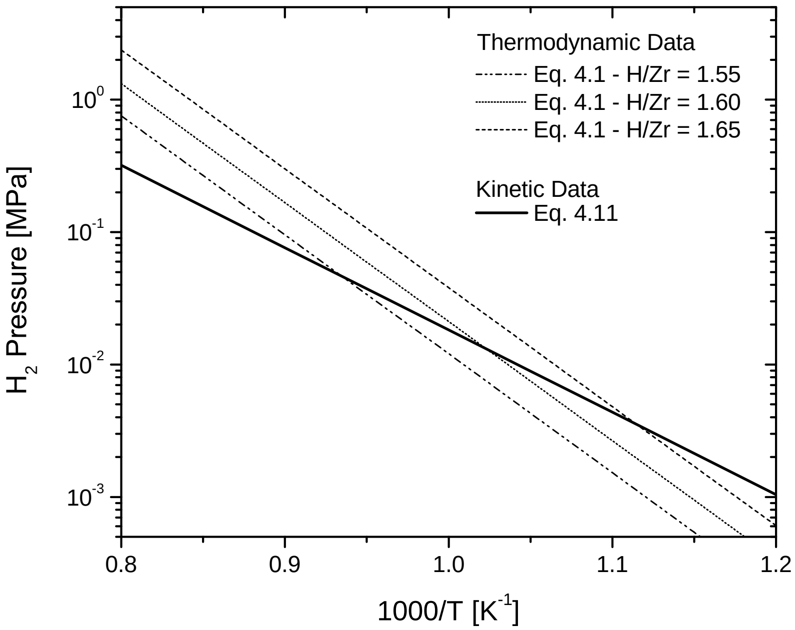

Figure 4.10: Comparison of the equilibrium hydrogen pressure over $ZrH_{1.6}$ from thermodynamic measurements with that inferred from the present kinetic data.

the case of a diatomic gas and a solid the kinetics is generally dependent on the surface concentration of adsorbed species to the second order. Typical formulation of adsorption and desorption rates are based on Equations 4.13 and 4.14. The pre-exponential term in the desorption rate is the product of the surface diffusivity of the adsorbed species, a combinatorial number, and the aereal density of the surface sites. The adsorption rate is the product of the collision rate, the sticking probability, and the coordination number of the surface sites.

$$R_{des} = k_d C^2 \exp \frac{-H_d}{RT} \tag{4.13}$$

$$R_{ads} = k_a p_{H_2} \left(1 - C^2\right) \exp \frac{-H_a}{RT} \tag{4.14}$$

In the above scenario, it is assumed that the hydrogen atom concentration in the bulk immediately beneath the surface and the adsorbed surface-hydrogen concentration are in equilibrium. The net desorption, in the case of surface-reaction-rate controlled second order kinetics, is the difference between the two above equations.

To investigate the applicability of the Langmuir model the evolution of the surface hydrogen concentration during the dehydriding process needs to be known. By applying Fick's first law, the rate of diffusion to the surface is determined as:

$$R_{diff} = -2DN_{Zr} \left.\frac{\partial C}{\partial x}\right|_{surf} \tag{4.15}$$

where N_{Zr} is the zirconium number density in δ-zirconium hydride (the number density of hydrogen lattice sites is twice that of zirconium atoms, hence N_{Zr} is multiplied by 2). Substituting for the difference between rates of desorption and adsorption from Equations 4.3 and 4.15 into Equation 4.4, yields the following:

$$\left.\frac{\partial C}{\partial x}\right|_{surf} = \frac{-1}{DN_{Zr}} \left[\frac{V}{RTS_d}\frac{dp}{dt} + \frac{S_v}{2S_d}R_{leak}\right] \tag{4.16}$$

Equation 4.16, employing the experimental results for $\frac{dp}{dt}$ and R_{leak}, could serve as the boundary condition for the transient diffusion equation (Fick's second law) during dehydriding. At the beginning of the dehydriding process the disks are assumed to have a uniform hydrogen concentration determined by the pressure at which the disks were processed (initial condition). The solution of diffusion equation (method discussed in Section 4.3.3), using the above boundary condition is shown for one of the samples in Figure 4.11 as a contour plot, where the H/Zr ratio across the half-thickness of the disk is depicted as a function of time .

The evolution in the surface hydrogen concentration alongside the change in hydrogen gas pressure inside the vessel as a function of time is shown in Figure 4.12. The evolution in surface hydrogen concentration shown in Figure 4.12 is such that it is not possible to predict the observed flux (as shown in Figure 4.6) utilizing Equations 4.13 and 4.14. This underlines the inapplicability of second order surface kinetics to describe the desorption process during the pressure-buildup experiments. The TGA results also contradict the applicability of second order surface kinetics since no sign of concentration dependence on the desorption rate (the adsorption rate is negligible throughout the TGA experiment since the dehydriding is performed under vacuum) is present. During the TGA experiment the hydrogen concentration is continuously reduced across the hydride while the net desorption flux remains constant (Figure 4.7).

4.3.2 Inapplicability of diffusion limited kinetics

In order to determine whether the desorption reaction is completely diffusion-limited, the computed pressure-buildup scenarios are compared to the experimental results. The computation assumes that the surface hydrogen concentration instantaneously equilibrates with the pressure inside the vessel according to Equation 4.1. This provides the surface boundary condition for solving the diffusion equation. The initial condition assumes that the vessel gas pressure at the onset of the dehydriding process is approximately zero. The flux at the surface is then calculated by using the hydrogen concentration gradient at the surface during the dehydriding process. The rate of change in vessel pressure could then be determined as shown in Equation 4.17. In the

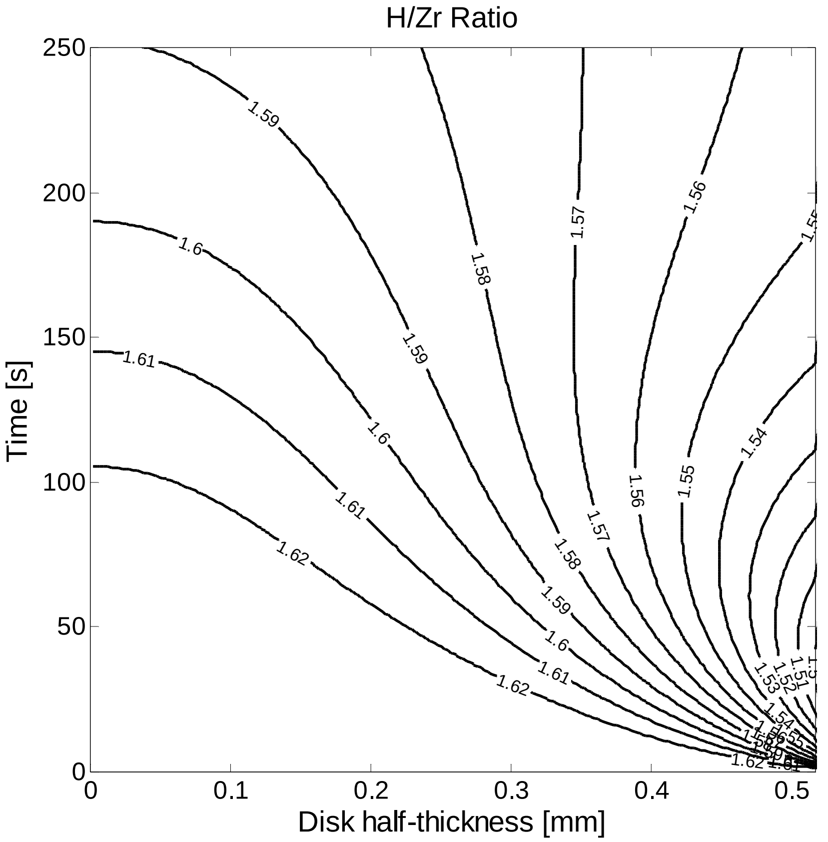

Figure 4.11: Evolution of hydrogen concentration across the disk and as a function of time during dehydriding at 880 °C with initial uniform H/Zr ratio of 1.63. The curves were obtained by solving the diffusion equation for H in the disk with Equation 4.16 as the surface boundary condition.

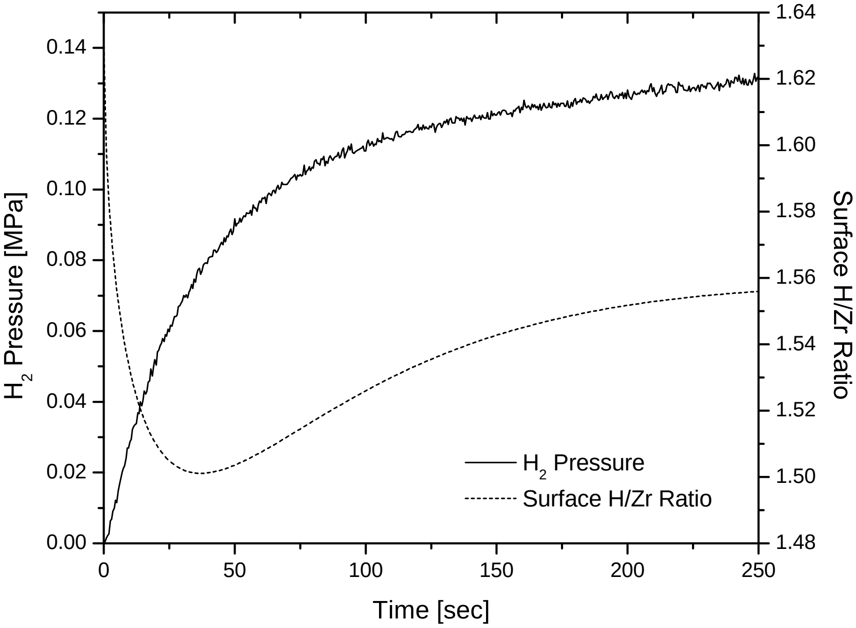

Figure 4.12: Accumulation of hydrogen gas inside the vessel and change in H/Zr ratio at the surface of hydride as a function of time during dehydriding at 880 ºC with initial uniform H/Zr ratio of 1.63.

right hand side of the equation the leakage term and the concentration gradient at the surface are known from experimental data and the solution to the diffusion equation respectively.

$$\frac{dp}{dt} = \frac{RTS_d}{V}\left[-DN_{Zr}\left.\frac{\partial C}{\partial x}\right|_{surf} - \frac{S_v}{2S_d}R_{leak}\right] \tag{4.17}$$

The solution scheme for the one-dimensional diffusion equation is discussed in Section 4.3.3. The computed pressure buildup from this diffusion-limited case deviates significantly from experimental results in two ways. The initial flux from the surface is orders of magnitude larger than what is determined experimentally in Section 4.2.1 and the equilibrium hydrogen pressure at the end of the desorption process is under- and overestimated at high and low temperatures, respectively. Also considering the TGA results, in case of diffusion limited kinetics, it is logical to expect that the surface hydrogen concentration gradient (and therefore the dehydriding rate) decreases as a function of time. This is the case when the surface hydrogen concentration is fixed (by the constant vacuum induced at the surface) and the bulk concentration is continuously decreasing. However no such observation is apparent in Figure 4.7 where the rate (the slope of the mass loss curve) is constant. Therefore the possibility of diffusion-limited kinetics is ruled out.

4.3.3 Numerical solution to the one-dimensional diffusion equation

The one-dimensional diffusion equation is a linear partial differential equation (Equation 4.18).

$$\frac{\partial C}{\partial t} = -D\nabla C \tag{4.18}$$

Discretization of this equation is done utilizing the Crank and Nicolson scheme [15], in which time is discretized with the trapezoid rule and space with central difference. This first step is shown in equation 4.19:

$$\frac{1}{\Delta t}\left(C_i^{j+1} - C_i^j\right) = \frac{-D}{2\Delta x}\left[\left(\frac{\partial C}{\partial x}\right)_{i+\frac{1}{2}}^{j+1} - \left(\frac{\partial C}{\partial x}\right)_{i-\frac{1}{2}}^{j+1} + \left(\frac{\partial C}{\partial x}\right)_{i+\frac{1}{2}}^{j} - \left(\frac{\partial C}{\partial x}\right)_{i-\frac{1}{2}}^{j}\right] \tag{4.19}$$

where i and j indicate the spatial node and time step, respectively. All terms are considered as node-centered. The equation is expanded and shuffled more:

$$C_i^{j+1} - C_i^j = \omega\left(C_{i+1}^{j+1} - 2C_i^{j+1} + C_{i-1}^{j+1} + C_{i+1}^j - 2C_i^j + C_{i-1}^j\right) \tag{4.20}$$

$$\omega = \frac{-D\Delta t}{2\Delta x^2} \tag{4.21}$$

The final form of the semi-implicitly-discretized diffusion equation is acquired and a marching procedure is performed with time, solving for the $j+1$st iterate from the known jth iterate:

$$\begin{bmatrix} 1 & -1 & 0 & 0 & 0 \\ -1 & \omega+2 & -1 & 0 & 0 \\ 0 & \ddots & \ddots & \ddots & 0 \\ 0 & 0 & -1 & \omega+2 & -1 \\ 0 & 0 & 0 & -1 & 1 \end{bmatrix} \begin{bmatrix} C_1^{j+1} \\ C_2^{j+1} \\ C_3^{j+1} \\ \vdots \\ C_N^{j+1} \end{bmatrix} = \begin{bmatrix} -1 & 1 & 0 & 0 & 0 \\ 1 & \omega-2 & 1 & 0 & 0 \\ 0 & \ddots & \ddots & \ddots & 0 \\ 0 & 0 & 1 & \omega-2 & 1 \\ 0 & 0 & 0 & 1 & -1+\frac{\xi}{C_N^j} \end{bmatrix} \begin{bmatrix} C_1^{j} \\ C_2^{j} \\ C_3^{j} \\ \vdots \\ C_N^{j} \end{bmatrix} \tag{4.22}$$

where ξ is the term incorporating the boundary condition. For instance, in case of the boundary condition discussed in Equation 4.16, ξ is:

$$\xi = \frac{-2\Delta x}{DN_{Zr}S_d}\left[\frac{V}{RT}\frac{dp}{dt} + \frac{S_v}{2}R_{leak}\right] \tag{4.23}$$

The diffusion coefficient is assumed constant over the range of hydrogen concentrations in the hydride.

4.4 Conclusions

Dehydriding of zirconium hydride has been studied in three experimental apparatuses: a pressure-buildup procedure in a closed vessel and two TGAs. The kinetic data from all three tests showed zeroth-order desorption kinetics. This was attributed to slow surface H atom recombination in conjunction with rapid re-supply of the surface from the hydrogen in the solid hydride. The adsorption step was found to be first order with respect to gas-phase hydrogen. The proposed model predicted the dehydriding kinetics over a wide range of conditions, but failed as equilibrium was approached.

Chapter 5

Incoherent Quasielastic Neutron Scattering Study of Hydrogen Diffusion in Thorium-Zirconium Hydrides

The thorium-zirconium alloy (Th:Zr = 1:2) reacts with hydrogen gas to form a monophase hydride with the hydrogen stoichiometry variable from 4 to 7 [9]. Hydrides with high hydrogen-to-metal (H/M) ratios are stable at temperatures typical of nuclear-reactor fuel operation. The presence of hydrogen in the fuel has neutronic advantages over oxide fuel, including thermally-induced hydrogen up-scattering of neutrons which provides a negative fuel reactivity coefficient at high temperatures. As discussed in Chapter 2, fuels utilizing thorium-zirconium hydrides as one of their constituents have been fabricated, irradiated, and characterized [74, 75, 67]. Normal reactor operation results in higher temperatures at the centerline of the fuel pellet than at the surface. This temperature gradient causes hydrogen redistribution by thermal diffusion (Soret effect) [46]. As was pointed out in Chapter 3, Hydrogen accumulation at the pellet periphery and the corresponding depletion at the center generates stress gradients due to expansion or contraction of the lattice as the H/M ratio changes. For the case of a reactivity insertion accident (RIA) or loss of coolant or flow throughout the core, the fuel temperature could increase significantly, forcing hydrogen redistribution or release from the fuel [66]. Therefore the diffusion coefficient of hydrogen in $ThZr_2$ hydrides is an important parameter that needs to be measured in order to predict the kinetics of the redistribution process and to model the fuel behavior under steady-state or transient-power conditions. Determination of the hydrogen diffusion coefficient in thorium-zirconium hydrides, through the means of IQNS, is the subject of this chapter.

5.1 Thorium-zirconium hydride ($ThZr_2H_x$)

The crystal structure of $ThZr_2H_x$ is cubic with a $Fd\bar{3}m$ space group. Bartscher et al. [9] have measured the lattice parameter of $ThZr_2$ hydrides and deuterides using X-ray and neutron diffraction and report the lattice parameter of the cubic unit cell as function of hydrogen or deuterium to metal ratio at room temperature. Figure 5.1 shows the lattice parameter as a function of hydrogen stoichiometry where a linear fit to the XRD data is also presented. However, the extent of uncertainty in the hydrogen and deuterium content of each compound is not reported, introducing further errors into the Vegards law model that is fitted through this data. Neutron powder diffraction experiments reveal that the hydrogen atoms are located in two different tetrahedral interstitial sites in the structure [8]. One is the 32e location, a site surrounded by one thorium and three zirconium atoms (4 sites per formula), and the other is the 96g location, a site surrounded by two thorium and two zirconium atoms (12 sites per formula). The fractional occupancy of hydrogen in the 32e and 96g sites, at room temperature and as a function of hydrogen stoichiometry, is shown in Figure 5.2. A schematic of the structure for this phase is presented in Figure 5.3.

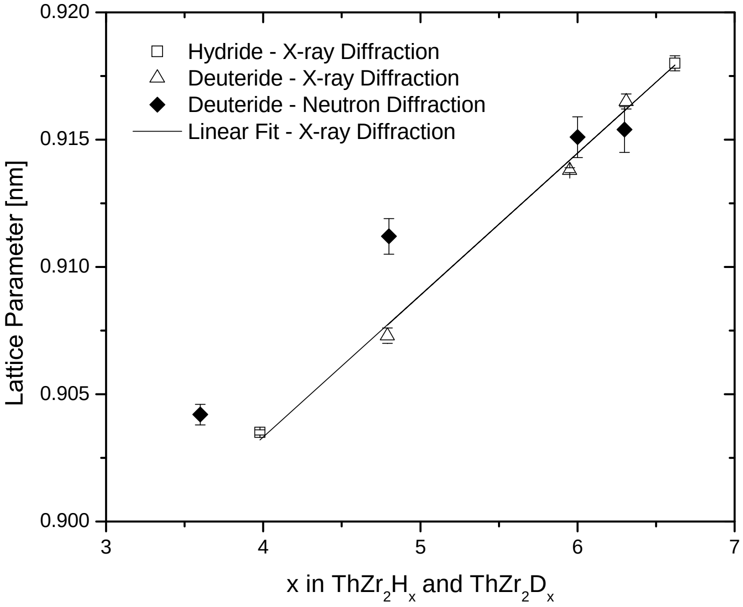

Figure 5.1: Lattice parameter as function of hydrogen/deuterium-to-metal ratio in ThZr$_2$H$_x$ and ThZr$_2$D$_x$ [9].

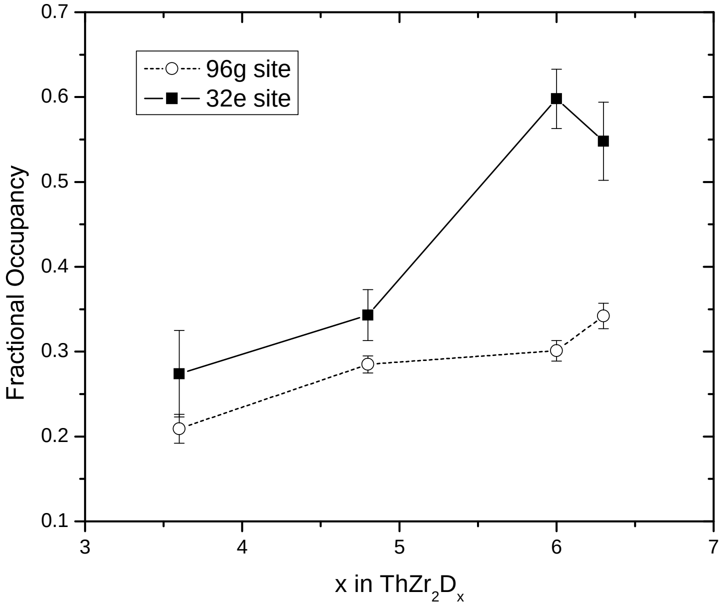

Figure 5.2: Fractional occupancy of hydrogen in the 32e and 96g sites at room temperature [8].

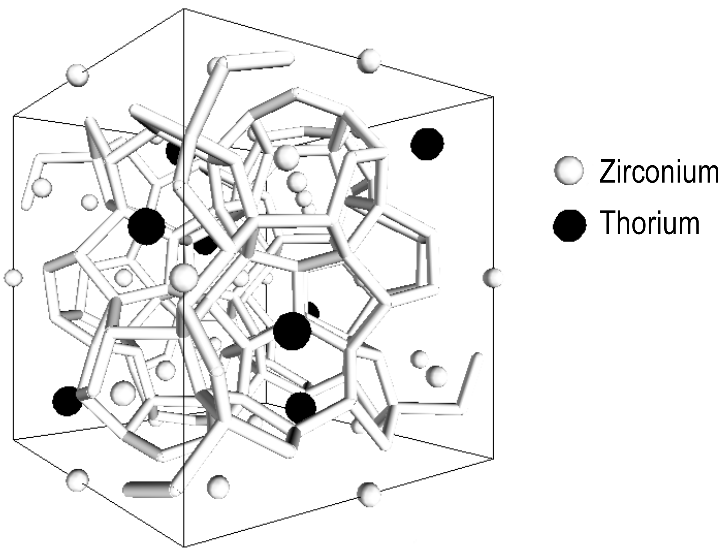

Figure 5.3: Crystal structure of $ThZr_2H_x$ (space group: $Fd\bar{3}m$). The hydrogen network is depicted in the form of polyhedra around the zirconium and thorium atoms.

5.2 Material processing

Ternary $ThZr_2H_x$ compounds exist over a wide range of hydrogen stoichiometries. Compounds of higher hydrogen content are of particular interest for thermal nuclear reactor applications since these compositions provide good neutron moderation while retaining adequately low hydrogen overpressures (thermodynamic stability). Pressure-temperature-composition equilibrium information exists for the ternary compound [9], enabling the desired stoichiometry to be selectively processed through precise control of the temperature and hydrogen gas pressure during hydriding.

Initially a $ThZr_2$ alloy was prepared by the Materials Preparation Center at Ames Laboratory starting from high-purity feedstock (99.93 at% Zr and 99.97 at% Th). The elements were mixed to the desired ratio and electron-beam melted (with 5 remelting steps) to form 15 grams of the homogeneous alloy. Examination of the Th-Zr binary phase diagram [45] implies that the melt initially solidifies into the BCC β-phase; a solid solution of thorium and zirconium. Upon cooling, if adequate time is given to reach equilibrium conditions, α-Th would start to precipitate at temperatures around 1173 K; while at temperatures below 923 K, all of the remaining β-phase would decompose into α-Th and α-Zr through a eutectoid reaction. The microstructure of the electron-beam melted metal alloy was investigated using scanning electron microscopy in the backscattering mode in Figure 5.4. Scanning electron microscopy was performed on a FEI instrument model XL30-SFEG equipped with secondary and backscatter electron detectors and an EDAX Phoenix EDS (energy dispersive X-ray spectroscopy) system. The accelerating potential during operation was 20 kV. Contrast in the electron mi-

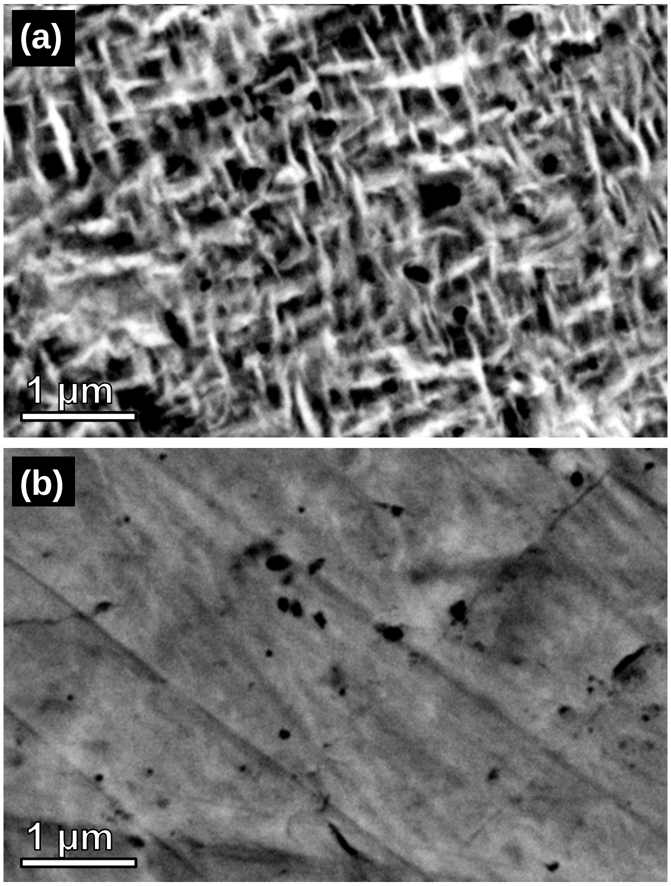

Figure 5.4: Backscattered electron image of: Top: electron beam melted $ThZr_2$ alloy, Bottom: $ThZr_2H_{5.6}$.

croscope image in the backscattering mode is a function of the difference between the average atomic number of the phases that are present. The microstructure of the metal alloy prior to hydriding, shown in Figure 5.4, is very fine; needle shape thorium grains (white phase) and spherical zirconium grains (black phase) have partially precipitated from the high temperature BCC solid solution (grey phase). EDS technique was also utilized to verify the composition of the overall alloy as shown in Figure 5.5. Due to the very fine microstructure and lack of spatial resolution, each phase could not be examined separately. Meanwhile, the EDS results confirm that the metal alloy is free of impurities and solely consists of thorium and zirconium.

Thin disks of the metal alloy (~0.5 mm) were placed in a stainless steel vessel while the temperature and H2 pressure were maintained constant for 30 minutes to achieve a uniform hydrogen concentration across the disk thickness. The hydrogen stoichiometry of the synthesized specimens was determined by X-ray diffractometry (XRD) with 80% confidence interval (Table 5.1). This was done by matching the measured lattice

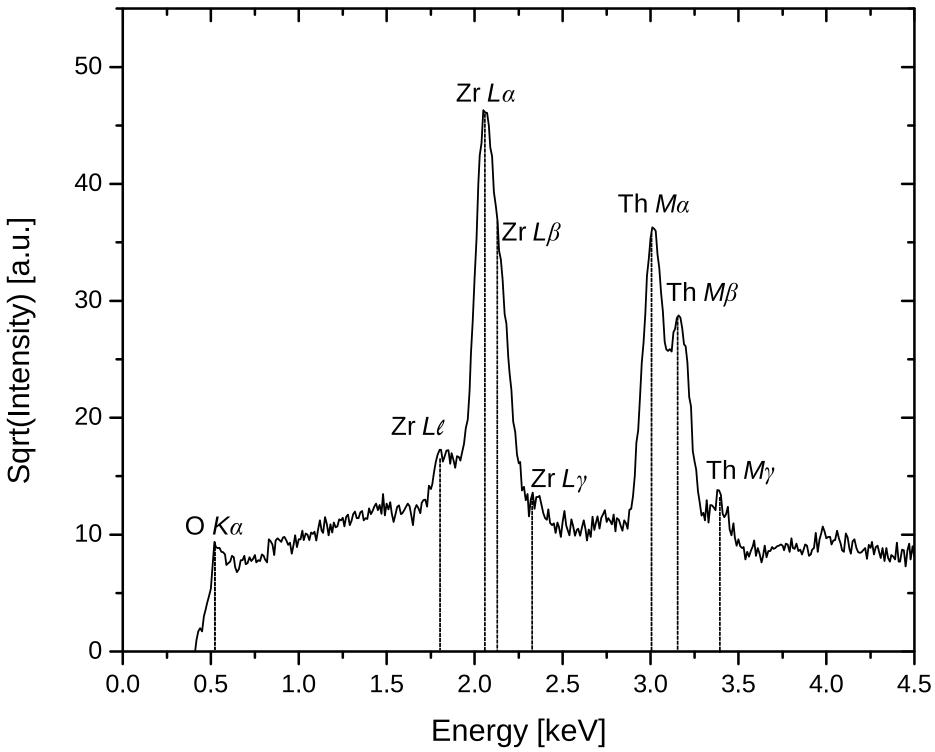

Figure 5.5: Energy-dispersive X-ray spectroscopy on electron-beam-melted $ThZr_2$ alloy from the area shown in Figure 5.4(a).

Temperature [°C]	Hydrogen Pressure [MPa]	Lattice Parameter [nm]	Hydrogen Stoichiometry
700	0.15	0.9150	6.2 ± 0.1
825	0.12	0.9119	5.6 ± 0.1

Table 5.1: Conditions for hydriding of 0.5 mm-thick alloy disks and the resulting lattice parameter and stoichiometry.

parameter with what is previously reported based on X-ray diffraction experiments on hydrides and deuterides (Figure 5.1). Hydride powders, mixed with lanthanum hexaboride (LaB_6 SRM660a) powder, were deposited on a low background silicon single-crystal sample holder using a slurry of powder mixture and ethanol to prepare the XRD samples. LaB_6 was employed as an internal standard during pattern refinement. A Phillips PANalytical X'Pert Pro instrument with a Cu Kα source was used to obtain high-resolution diffraction patterns. Results of the XRD experiment performed on $ThZr_2H_{5.6}$ mixed with LaB_6 confirm formation of a single phase hydride as well as the presence of some unknown Bragg peaks (Figure 5.6). None of the following phases (accompanied by the associated space group), corresponding to any other hydrides or metallic alloys of thorium and/or zirconium, were detected in any significant amount in the diffraction patterns: δ-$ZrH_{1.6}$($Fm\bar{3}m$), ε-$ZrH_{1.8}$ ($I4/mmm$); ZrH ($P42/n$); ThH_2 ($I4/mmm$); Th_4H_{15} ($I\bar{4}3d$); Zr ($P63/mmc$); ThZr ($Im\bar{3}m$); Th ($Fm\bar{3}m$). For the X-ray diffraction experiment, the material is crushed into a very fine powder and exposed to air resulting in the possible formation of oxide products. The unknown Bragg peaks are therefore either due to foreign contamination or oxide products. The backscattering electron image of the $ThZr_2H_{5.6}$ hydride specimen in Figure 5.4 also shows formation of a uniform monophase. Negligible extent of a second phase is also apparent in the form of black particles within the grey matrix (the black regions are not pits or wholes).

XRD and microscopy results confirm that the $ThZr_2H_x$ is the dominant phase that has formed after the hydriding and hydrogen is only present within this phase. The influence of the unknown phase on the results of the IQNS experiment can be disregarded for two reasons. First, the volume fraction of this phase is very negligible and the possible incoherent neutron scattering signal from this phase is very limited. Second and most importantly, the incoherent neutron scattering cross section for hydrogen is the second largest in the periodic table (10^5 times larger than that of oxygen), only behind gadolinium. Consequently, the incoherent neutron scattering signal measured in this experiment is dominated by the hydrogen in $ThZr_2H_x$ phase. For this same reason, the presence of thorium, zirconium, and aluminum in the metal hydride matrix is inconsequential to the measurement of hydrogen diffusion coefficient.

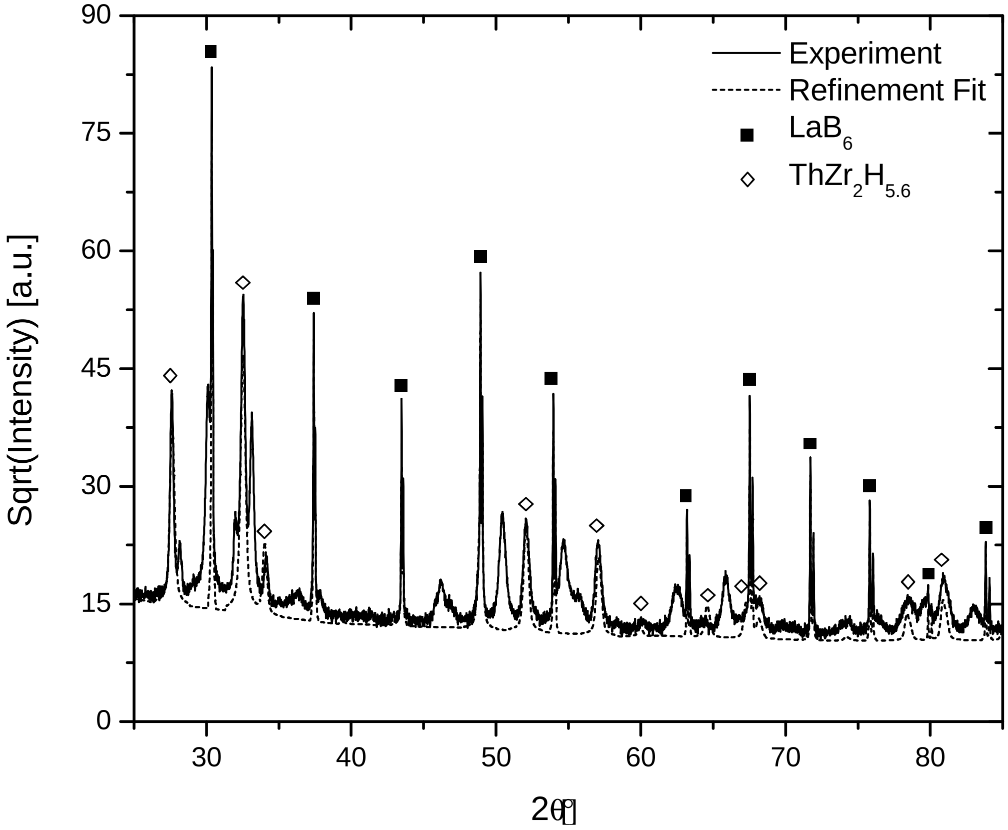

Figure 5.6: Powder X-ray diffraction pattern for $ThZr_2H_{5.6}$ and LaB_6 standard along with Rietveld refinement fit.

5.3 Experimental details

A useful review of IQNS theory and experimental techniques is provided by Hempelmann [29] and can provide background information for the following sections. For this experiment an all aluminum sample holder was utilized consisting of two 2.75″ ConFlat (CF) flanges (Al-6061-T6), an aluminum gasket (Al-1060), and aluminum nuts and bolts (Al-2024-T4). Aluminum is ideal because it is almost entirely a coherent scatterer of neutrons. Utilization of the CF flange assembly guaranteed a leak-proof container under the high-vacuum conditions of the beam chamber (10^{-4} Pa). Due to the large hydrogen content of the material, multiple scattering at low angles is of concern for thick samples. The hydride pieces were crushed into fine powder and diluted with high-purity (99.99%) aluminum powder (10vol% $ThZr_2H_x$ – 90vol% Al). The powder mixture was spread thin into a 0.5 mm thick layer held tightly between the two flanges and an aluminum plate (Al-6061-T6) with thickness of 1.94 mm (the plate was used to fill up the entire available volume). The central region (at the exterior) of the CF flanges was machined down to 1 mm thickness to minimize sample holder interaction and attenuation of the neutron beam. The final sample holder assembly is shown in Figure 5.7.

The sample was then exposed to the neutron beam at the Backscattering Silicon Spectrometer (BASIS) at the Spallation Neutron Source (SNS) located in Oak Ridge National Laboratory [41]. The incoming neutron beam of this time-of-flight (TOF) instrument has a bandwidth centered around 2082 μeV (0.6267 nm) (selected by application of the beam choppers). After the beam interacts with the sample, only the neutrons that have an energy of 2082 μeV scatter off of Si(111) crystals to be detected in a 2-D array of He-3 detectors. While offering a wide momentum-transfer range of $2\ \text{nm}^{-1} < Q < 20\ \text{nm}^{-1}$, energy transfers of up to ±200 μeV are simultaneously measured with 3 μeV (FWHM) resolution. Energy transfers are calculated as the difference between the incident neutron energy (determined from the overall time-of-flight before detection) and the fixed final energy of 2082 μeV selected by Si(111) reflections.

In this experiment, the instrument resolution function was collected at room temperature for each sample since hydrogen atoms are immobile on the time scale of the BASIS and scattering is almost purely elastic. The double-differential cross section corresponding to the scattering function was then obtained over the range of attainable momentum and energy transfers. Experimental data was collected for the two hydrides in the temperature range of 650 K to 750 K with 25 K steps. The maximum temperature was limited by the integrity of the aluminum sample holder, while for temperatures lower than 650 K the limit is the extent of quasielastic broadening as it approaches the resolution of the instrument. This range is ideal since temperatures between these two limits span that of proposed LWR hydride fuel discussed in Chapter 3. Data collection took place over a period of 6 hours for each experimental temperature to achieve good statistics. The incoherent scattering function that upon its convolution with the resolution function corresponds to the measured intensities was

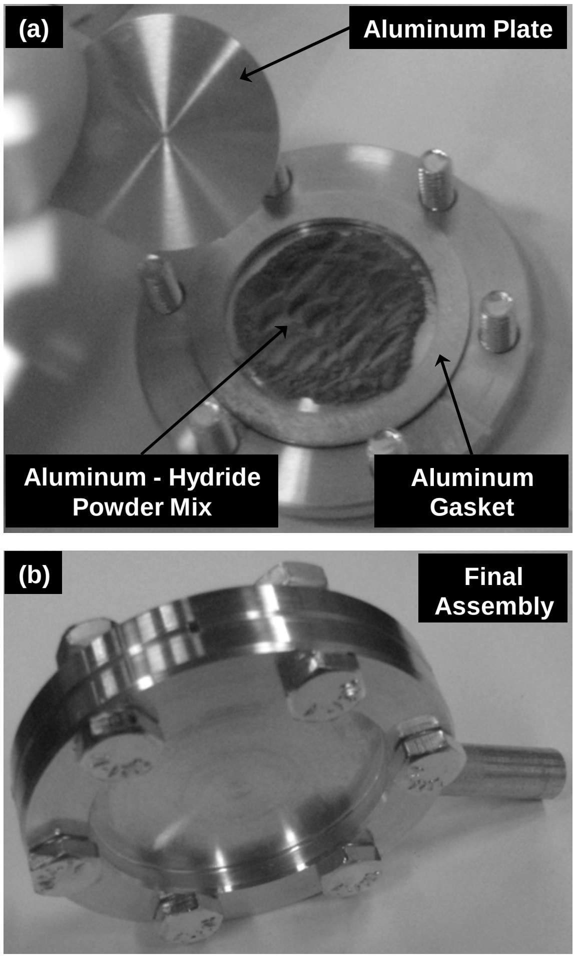

Figure 5.7: Top: Sample holder during assembly, Bottom: final configuration.

Table 5.2: Diffusion parameters and average jump lengths for hydrogen in thorium-zirconium hydride.

Material	$D_\circ$ [10^{-7} m^2/s]	E_a [meV]	$< l >$ [nm]
$ThZr_2H_{5.6}$	6.1 ± 4.8	460 ± 50	0.24 ± 0.01
$ThZr_2H_{6.2}$	1.2 ± 0.9	335 ± 50	0.27 ± 0.02

extracted from the data using the DAVE software package [1]. No correction was made for multiple scattering at low angles since this effect is minimal for the thin samples.

5.4 Results

Quasielastic linewidth broadening of the spectra from $ThZr_2H_{5.6}$ is shown in Figure 5.8. Even though the experiment has probed a relatively narrow temperature range, the change in the linewidth broadening is readily apparent. Broadening values were obtained using fits of the spectra with a Lorentzian quasielastic term, an elastic term, and a background term.

The isotropic Chudley-Elliott model [13] was applied in order to analyze the broadening of the incoherent scattering function (a Lorentzian function) at different temperatures. According to this model, the quasielastic linewidth (Λ) as a function of momentum transfer (Q) at each temperature is given by Equation 5.1.

$$\Lambda(Q) = \frac{6\hbar D}{l^2}\left(1 - \frac{\sin(Ql)}{Ql}\right) \tag{5.1}$$

where $\hbar$, D, and l are Planck's constant, the diffusion coefficient, and the average jump distance, respectively. Equation 5.1 is spatially averaged since a single-jump mechanism, representing an average of all possibilities, is assumed. Fitting the model to the experimental data in Figure 5.9 shows excellent agreement between the two. Values for the diffusion coefficient and the jump distance were extracted from the data at each temperature through the fitting process. The Arrhenius dependence of the hydrogen diffusion coefficient and the atomic jump distance are shown in Figures 5.10 and 5.11 respectively, and in Table 5.2.

5.5 Discussion

5.5.1 Hydrogen atom jump vector

Although a large momentum-transfer range was probed, details regarding exact jump vectors could not be obtained due to the short H atom jump distances. As discussed in Section 5.1, multiple jump scenarios exist based on the location of the H-atom inside the lattice. These possibilities are summarized in Table 5.3 along with the

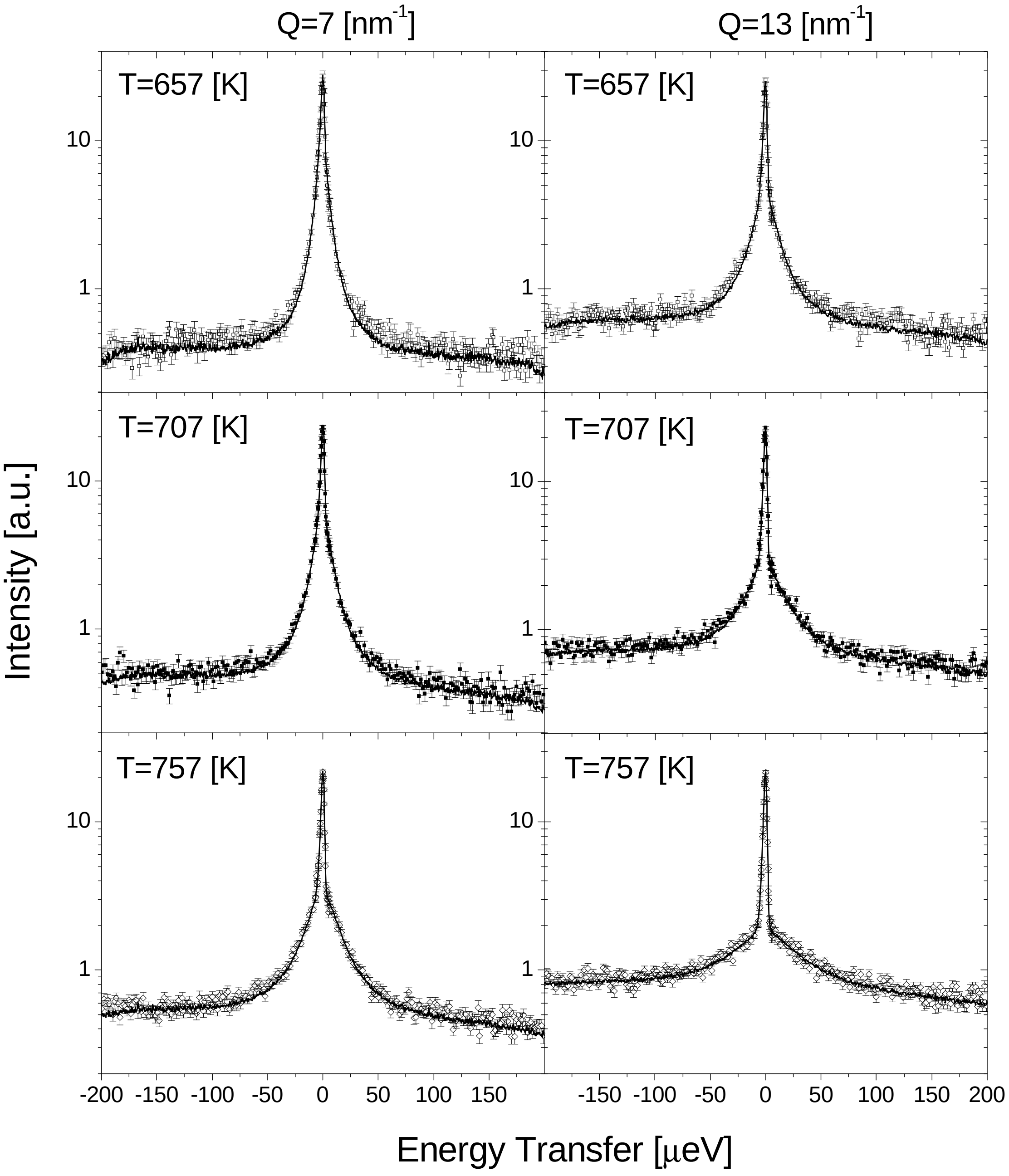

Figure 5.8: Quasielastic spectra for $ThZr_2H_{5.6}$ at different temperatures and scattering momentum transfers.

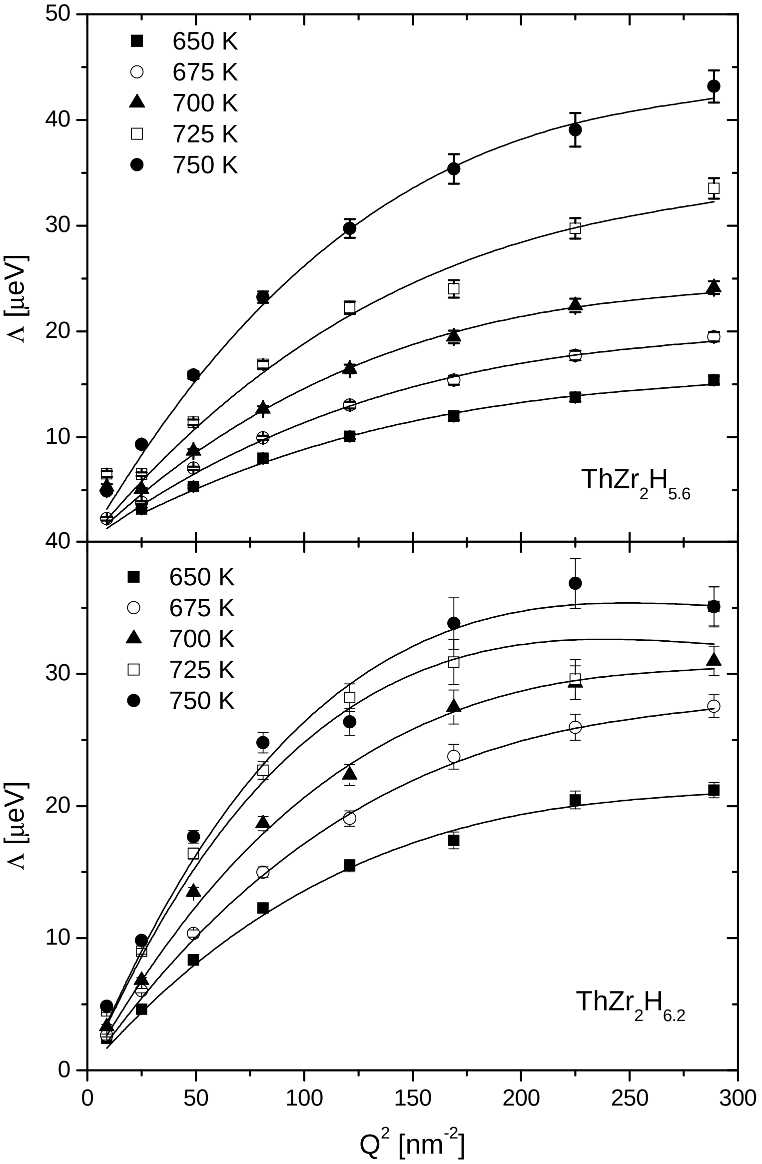

Figure 5.9: Quasielastic linewidths (HWHM) as a function of Q^2 for $ThZr_2H_{5.6}$ and $ThZr_2H_{6.2}$.

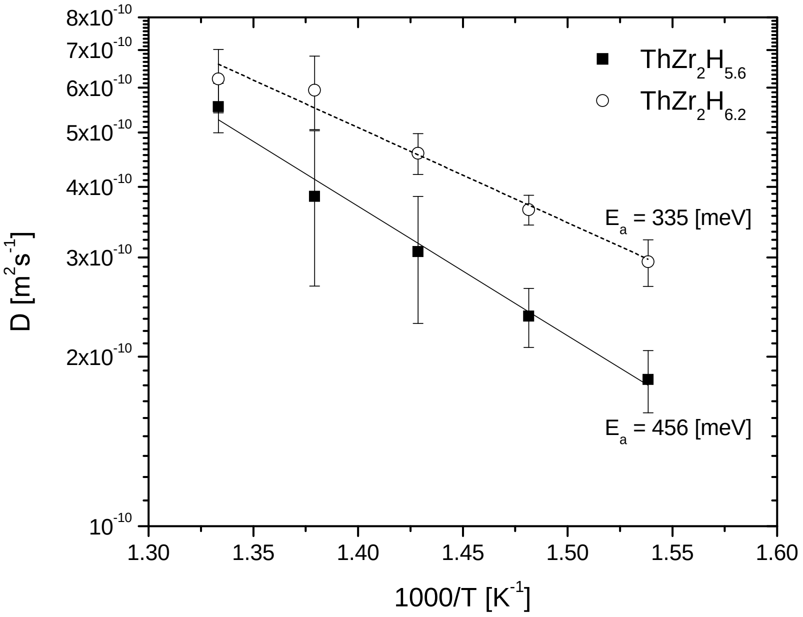

Figure 5.10: Hydrogen diffusion coefficient in $ThZr_2H_{5.6}$ and $ThZr_2H_{6.2}$.

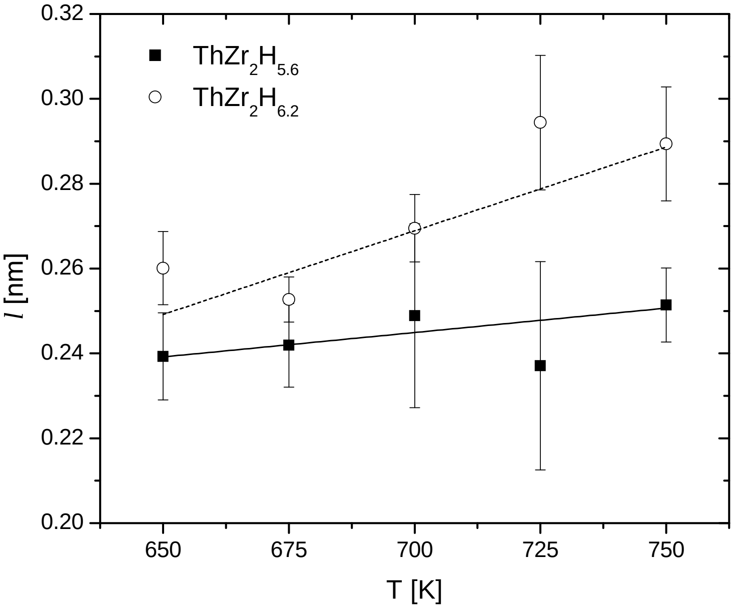

Figure 5.11: Hydrogen atom jump distances in $ThZr_2H_{5.6}$ and $ThZr_2H_{6.2}$..

Table 5.3: Routes and associated H-atom jump distances.

Initial Position	End Position	Coordination Number of the Jump	l [nm]
96(g)	32(e)	1	0.139
	96(g)	2	0.146
	96(g)	1	0.165
	96(g)	2	0.228
	32(e)	2	0.235
	96(g)	4	0.243
	32(e)	1	0.245
	96(g)	2	0.252
	96(g)	1	0.291
32(e)	96(g)	3	0.139
	96(g)	6	0.235
	96(g)	3	0.245
	32(e)	3	0.248

spacing between each of the two atomic sites. The distances are calculated from the structure and the lattice parameter of $ThZr_2H_{5.6}$ (0.912 nm). Based on a survey of a large number of stable hydrides, Switendick argues that the minimum H-H distance is no less than 0.21 nm [63]. Specifically for the space group hydrides, Shoemaker et al. [55] suggest that no two adjacent tetrahedral hydrogen atom sites (i.e., sharing a common triangular face) can simultaneously accommodate hydrogen atoms. Neglecting distances less than 0.2 nm in table 3, the average jump distances are in agreement with experimental values in Table 5.2.

The extent of error specified for each data point in Figure 5.11 corresponds to one standard deviation in a normal distribution. Assuming that the true value of the jump distance is bound within this error window, the only possible jump path in Table 5.3 for the two highest temperature points in the $ThZr_2H_{6.2}$ sample is between two 96g sites with the spacing of 0.29 nm. This finding suggests a preferred path for hydrogen diffusion in this sample at high temperatures even though large momentum transfer regimes were not investigated. This change in the diffusion path at high temperatures is accompanied with a change in activation energy of diffusion that is associated with the specific jump vector. Consequently, this results in deviations from the simplified Arrhenius model fitted to the diffusion data in Figure 5.10.

The average jump distance is the probability-weighted sum of all possible jump distances. The fitted lines to the data in Figure 5.11 portray a direct relationship between average jump distance and the temperature. If the probability associated with each jump path is not a function of temperature, then the average jump distance is linearly proportional to the lattice parameter at each temperature. Therefore the coefficient of thermal expansion (CTE) could be estimated from the data in Figure 5.11 using Equation 5.2:

$$\alpha = \frac{d}{dT}\ln(l) \tag{5.2}$$

The values extracted for CTE from Figure 5.11 are 3×10^{-4} K^{-1} for $ThZr_2H_{5.6}$ and 1.5×10^{-3} K^{-1} for $ThZr_2H_{6.2}$. These values observed based on increase of the average jump distance with temperature are orders of magnitude larger than what is typically detected from other hydrides (~ 2.5×10^{-5} K^{-1} for zirconium hydride [78]). This result implies that the probability associated with each different jump is indeed a function of temperature where the probability for jump between two sites with larger spacing becomes more favorable with increasing temperature. This implication is consistent with the statements in the previous paragraph where deviations from simple Arrhenius behavior are expected.

5.5.2 Activation energy and pre-exponential term for hydrogen diffusion

The microscopic three-dimensional Einstein diffusion equation is described in Chapter 3 (Equation 3.4) and for interstitial hydrogen atoms can be expanded as follows:

$$D = \frac{1}{6}l^2\eta v \exp\left(\frac{-E_a}{kT}\right) \tag{5.3}$$

where v is the vibrational frequency and η is the product of the number of adjacent jump sites and the probability that the site is currently unoccupied by another hydrogen atom. Assuming that v is equivalent for both hydrides, the difference in the observed pre-exponential factors can be explained by differing values of l and η. For large H/M ratios, hydrogen atoms have a slightly larger average jump distance. The probability of vacant adjacent interstitial site is one minus the fractional occupancy of available hydrogen sites. Although many interstitial sites for H atoms exist (see section 5.1), the criterion set by Shoemaker indicates that the maximum H/M ratio is < 7. If so, η for $ThZr_2H_{5.6}$ is 1.75 times larger in $ThZr_2H_{6.2}$. Thus, the larger pre-exponential factor for the lower stoichiometry hydride is expected.

The dissimilar activation energies for hydrogen diffusion (E_a) in the two hydrides can be explained qualitatively by inspection of the pressure-temperature-composition equilibria [9]. The partial molar enthalpy of hydriding at different hydrogen-to-metal ratios is shown in Figure 5.12. A rather complex relationship between the partial molar enthalpy of hydriding and hydrogen concentration in the hydride exists, implying that the fractional occupancy of the possible hydrogen sites and the bonding strength at each site are complex functions of hydrogen concentration. The fractional occupancy of the 96g and 32e sites are shown in Figure 5.2 and indeed show a nonlinear variation with hydrogen concentration at room temperature. In the meantime it is possible to discern a decreasing trend in (absolute value) with increasing H/M ratio in Figure

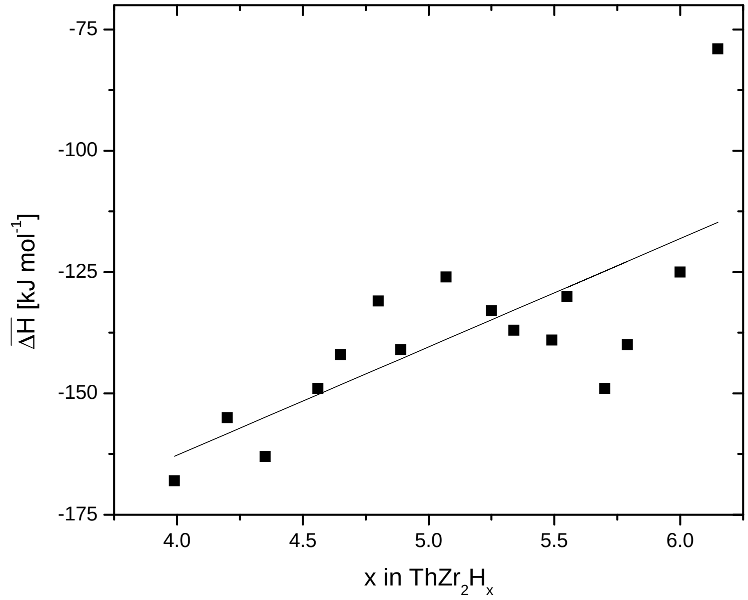

Figure 5.12: Partial molar enthalpy of hydriding as a function of x in $ThZr_2H_x$ [9].

5.12. This trend suggests a reduction in the strength of the average hydrogen-metal bond as the hydrogen content of the hydride increases. This implies that H atoms in the lower stoichiometry hydride are more tightly bonded and require larger activation energies to overcome the jump barrier than in the higher hydride. This implication is in agreement with what is observed experimentally.

5.6 Conclusions

Quantification of hydrogen diffusivity in Th-Zr hydrides is of great interest to design and optimize hydride fuel fabrication processes and to model fuel behavior under steady state and transient power conditions. In order to measure interstitial hydrogen diffusion, quasielastic broadening of the incoherent-neutron-scattering signal from ternary thorium-zirconium hydrides has been determined over the temperature range 650 K to 750 K. This temperature range is typical of hydride nuclear fuel under steady state reactor operation. The measurement was done over a wide range of energy and momentum transfers, simultaneously and rapidly, using the time-of-flight backscattering spectrometer (BASIS) at the Spallation Neutron Source at ORNL. The isotropic Chudley-Elliott diffusion model accurately predicts the measured variation of the quasielastic Lorentzian linewidth broadening as a function of momentum transfer. Using this data the pre-exponential term and the activation energy of hydrogen diffusion in two Th-Zr hydrides could be quantified applying a simplified Arrhenius model.

Although the hydrogen jump distance is small and the probed momentum transfer range (corresponding to distance in reciprocal space) was limited, the spatially-averaged jump distances of hydrogen atoms extracted from the isotropic Chudley-Elliott model are in agreement with the structural information. The difference in the average activation energy for hydrogen atom jump at different hydrogen concentrations is also coherent with the available thermodynamic information. Meanwhile, recognizing the complex structure of Th-Zr hydrides where multiple hydrogen atom sites and jump paths with different bonding strengths and activation energies are present, deviations from the simplified Arrhenius behavior is expected over larger temperature ranges.

Chapter 6

Compatibility of Liquid-Metal-Bonded Hydride Fuel in Contact with Unoxidized and Oxidized Zircaloy

A significant disadvantage of hydride fuels compared to oxides is its high fission-product swelling rate [47], which could cause premature pellet-cladding interaction (PCI). Application of hydride fuels in LWRs [32] requires Zircaloy cladding. Zircaloy is desirable from a neutronics standpoint and exhibits adequate waterside corrosion behavior under LWR operating conditions. However, Zircaloy is a getter for hydrogen, so the cladding could be severely embrittled by transfer of hydrogen from the fuel. In order to overcome this potential shortcoming, a fuel-cladding gap large enough to avoid gap closure during service is needed. To prevent the increase in fuel temperature that accompanies an increase of gap thickness, the gap is filled with a liquid-metal (LM) alloy. The LM could be the eutectic lead-bismuth alloy (Bi-44wt%Pb, mp = 126 °C) or a ternary alloy of lead, bismuth, and tin (Pb-33wt%Sn-33wt%Bi, mp = 120 °C). Replacing helium in the gap with LM has been demonstrated for full-length oxide fuel rods [73]. Since the LM thermal conductivity is two orders of magnitude higher than that of helium conventionally used as the gap filler, the temperature drop across the gap is negligible irrespective of its thickness. The remaining challenge is to prevent transfer of hydrogen from the fuel to the cladding. From a thermodynamic standpoint, hydriding of the cladding is inevitable; ultimately the system evolves towards the equilibrium where the activities of hydrogen in the fuel, the liquid metal and Zircaloy are the same. The focus of this chapter is to investigate the effectiveness of the liquid metal, possibly coupled with a thin zirconia layer, as a kinetic barrier to hydrogen transfer between hydride fuel and cladding.

6.1 Experimental setup

A disk of Zircaloy-2 was sandwiched between disks of hydride fuel and stainless steel (SS316). The $(U_4Th_2Zr_9)H_{1.5}$ hydride used for the compatibility experiments consists of three phases: α-U, δ-$ZrH_{1.6}$, and $ThZr_2H_7$ (Figure 6.1). The details of the fabrication and characterization of this fuel are discussed in Chapter 2. The arrangement was submerged in LM inside a stainless steel cell. Force was exerted on the assembly by application of a torque screw (Figure 6.2) using a digital torque meter, thereby permitting control of the contact pressure. The contact pressure was also affected by joint friction. In order to accurately determine the contact pressure, the torque was calibrated against the force using a load cell at experimental temperatures.

Contact was be made between the fuel and cladding in all of the samples except one. The contact pressures were 50 and 120 MPa, which are below the 240 MPa yield stress of Zircaloy [28]. For one of the samples, a gap of 25 μm in thickness between the hydride and Zircaloy was established using thin platinum wires. Table 6.1 summarizes the sample conditions. Different oxide layers were grown on the surface of three of the Zircaloy disks by exposing the samples to air at high temperatures. Table 6.2 summarizes the conditions used during oxide growth in air.

Subsequently the cells were placed in a bath of LM contained in a stainless steel ves-

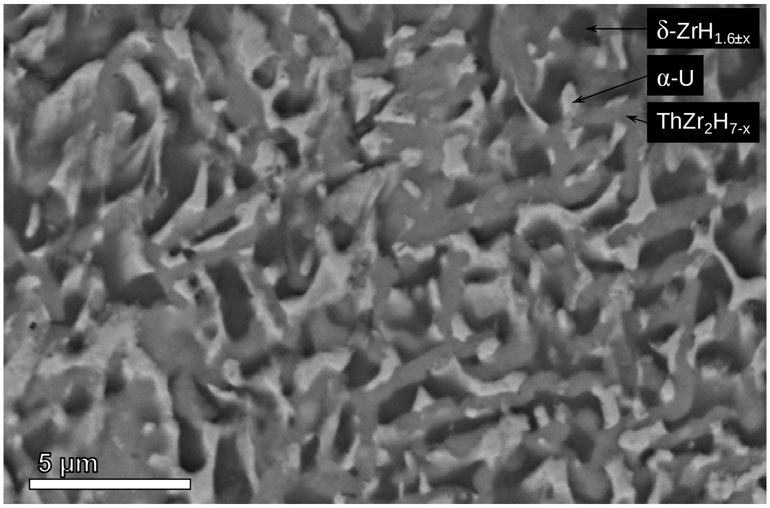

Figure 6.1: SEM (backscattering mode) image of $(U_4Th_2Zr_9)H_{1.5}$ consisting of α-U, $ThZr_2H_7$, and δ-$ZrH_{1.6}$ appearing as the brightest to the darkest phase respectively.

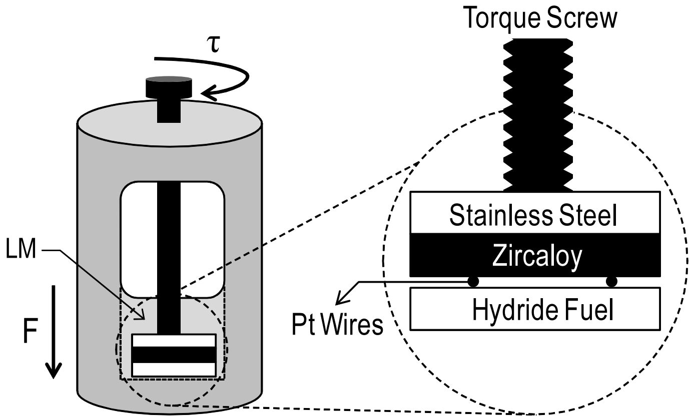

Figure 6.2: Cell setup for hydride and Zircaloy placed in contact and submerged in LM. The Pt wires are removed to simulate a closed fuel-cladding gap.

Table 6.1: Summary of the sample conditions for the compatibility tests.

Sample ID	Temperature [°C]	Oxide Layer	Contact Pressure [MPa]
1	375	N	no contact
2	375	N	50
3	375	N	120
4	375	Y	50
5	375	Y	50
6	375	Y	50

Table 6.2: Summary of the sample conditions during oxide growth.

Sample ID	Growth temperature [°C]	Growth duration [hr]	Air pressure [MPa]	Oxide layer thickness [µm]
4	350	24	10	0.9 ± 0.1
5	500	24	10	3.2 ± 0.6
6	600	8	0.1	2.7 ± 0.2

sel and heated to 375 °C under helium at 1 atm. Consecutive cycles of helium pressure and vacuum were also induced initially to remove any bubbles from the liquid metal. The pressure and temperature conditions were maintained for a period of one month to assess the compatibility between Zircaloy and hydride fuel. Upon completion of the compatibility tests, each sample was sectioned, mounted in epoxy and polished to a fine finish; no etching was performed. The interface between the fuel and cladding was investigated using a scanning electron microscope (SEM) with an accelerating potential of 20 kV.

As discussed earlier, the goal of this investigation was to determine the possibility and extent of hydride formation in the cladding. While very few techniques are capable of directly detecting hydrogen in materials, SEM could be useful in this case assuming hydrogen precipitates a new and distinct phase. Contrast in the electron microscope image, especially in the backscattering mode, is a function of the average atomic number of the phases present, thereby permitting the hydride to be distinguished from the metal. In addition the cladding was examined for signs of cracking caused by hydriding of the Zircaloy.

6.2 Results

6.2.1 Unoxidized Zircaloy

A liquid-metal-filled gap (~25 µm) was maintained between the fuel and the cladding for sample 1 using platinum wires wrapped around the hydride. The liquid metal exhibited good wetting of both surfaces, and was completely free of voids or bubbles (Figure 6.3). The solidified LM consisted of tin (appears dark in the image), bismuth, and the hexagonal Pb_3Bi phases (appearing bright in the image). No sign of hydride precipitation or cracking was observed in the Zircaloy for sample 1. Fuel cracking occurred during extraction of the sample from the steel cell after the completion of the compatibility experiment.

Interface between the fuel and the cladding for sample 2 (50 MPa contact pressure) and sample 3 (120 MPa contact pressure) are very similar; all the LM has been squeezed out of the gap and direct contact between the cladding and fuel was made. Severe cracking of the cladding at the interface is apparent, implying that Zircaloy has

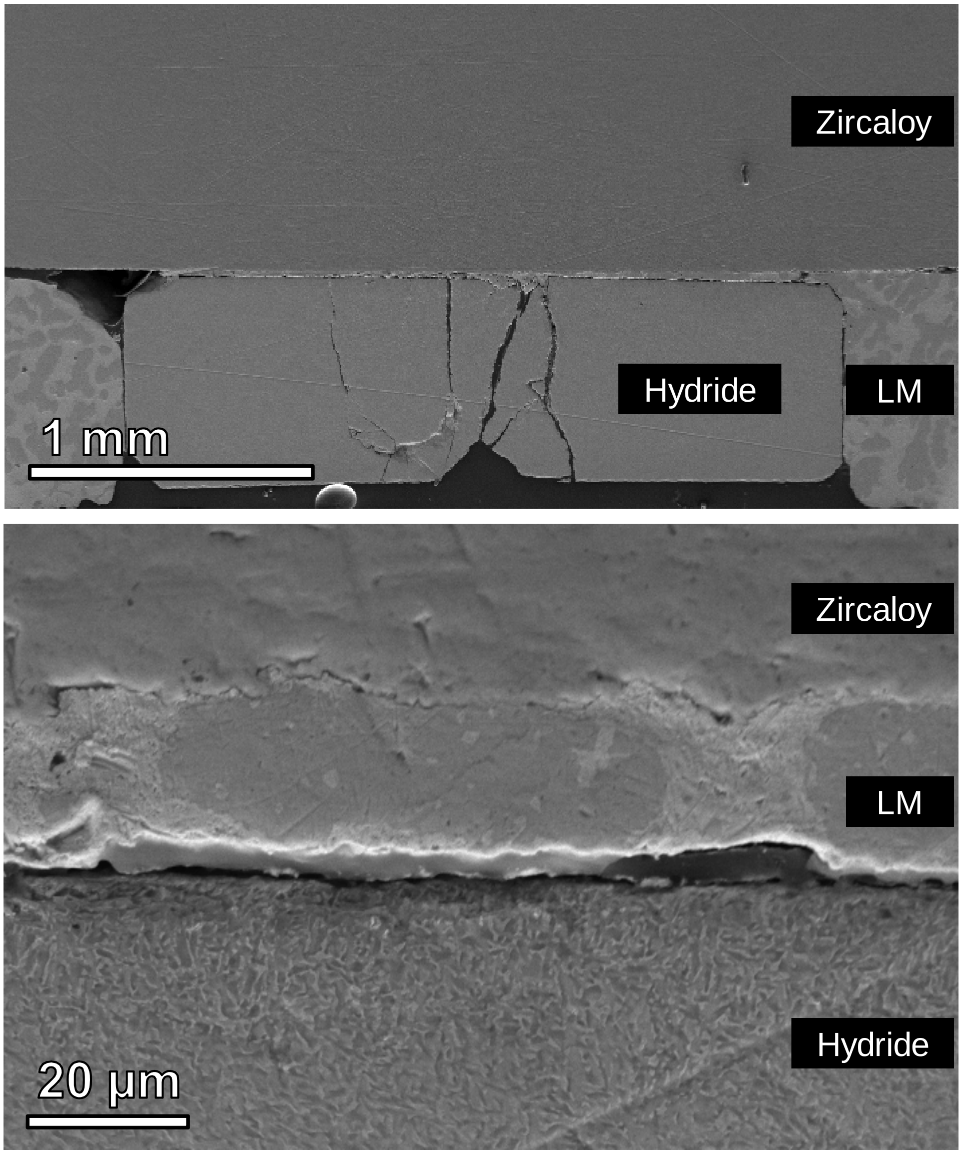

Figure 6.3: LM-filled hydride-Zircaloy interface for sample 1 at different magnifications (secondary electron image).

undergone hydriding (Figure 6.4). No distinct hydride phase could be distinguished in the cladding, even though hydrogen embrittlement has occurred.

6.2.2 Oxidized Zircaloy

The results for the Zircaloy specimens with oxidized surfaces (samples 4, 5 and 6) were identical; no sign of hydride formation or cracking of the Zircaloy was observed. Although the contact pressure during these experiments was 50 MPa, the gap between the fuel and the cladding was never completely closed (at least in the areas that were investigated) due to surface roughness. Therefore hydrogen transport through the gaseous phase would have been possible. The characteristics of the interface between Zircaloy with oxide layer and hydride fuels is shown in Figure 6.5 for sample 4.

6.3 Oxide layer characteristics

The nature of the black oxide grown on the surface of Zircaloy disks was investigated prior to testing by X-ray diffractometry and scanning electron microscopy coupled with energy dispersive X-ray spectroscopy (EDX). During X-ray diffractometry (from the bare surface of oxidized Zircaloy disks) all the samples exhibited quite similar diffraction patterns. Rietveld refinement of the obtained diffraction patterns showed that the oxide consisted mainly of the monoclinic baddeleyite with trace amounts of cubic zirconia (Figure 6.6). Formation of tetragonal zirconia was rejected since the major reflections from these phases were missing. The backscattering electron images of the oxide layers on the three oxidized Zircaloy specimens are shown in Figure 6.7. Formation of a distinct layer underneath the oxide layer is apparent in this mode. The contrast from this layer is similar to that of Zircaloy, except slightly brighter; implying that the average atomic-number (Z) density in that phase is comparable or slightly higher than that of Zircaloy phase. EDX spectra from the three distinct regions in Figure 6.7(b) are shown in Figure 6.8; this shows that the unknown layer contains very little oxygen.

Oxidation of Zircaloy-4 in air was studied extensively by Steinbrück, who observed formation of zirconium nitride under the oxide layer [60]. The zirconium atomic density in zirconium nitride is almost identical to that of the hexagonal zirconium metal phase; this is consistent with the bright contrast in the backscattered electron image. Nitrogen Kα radiation at 0.392 keV is just below the detection limit of this EDX spectroscopy instrument. While the 220 reflection from zirconium nitride phase in the X-ray diffraction pattern is missing, this could be because the zirconium nitride layer is buried under the zirconia layer.

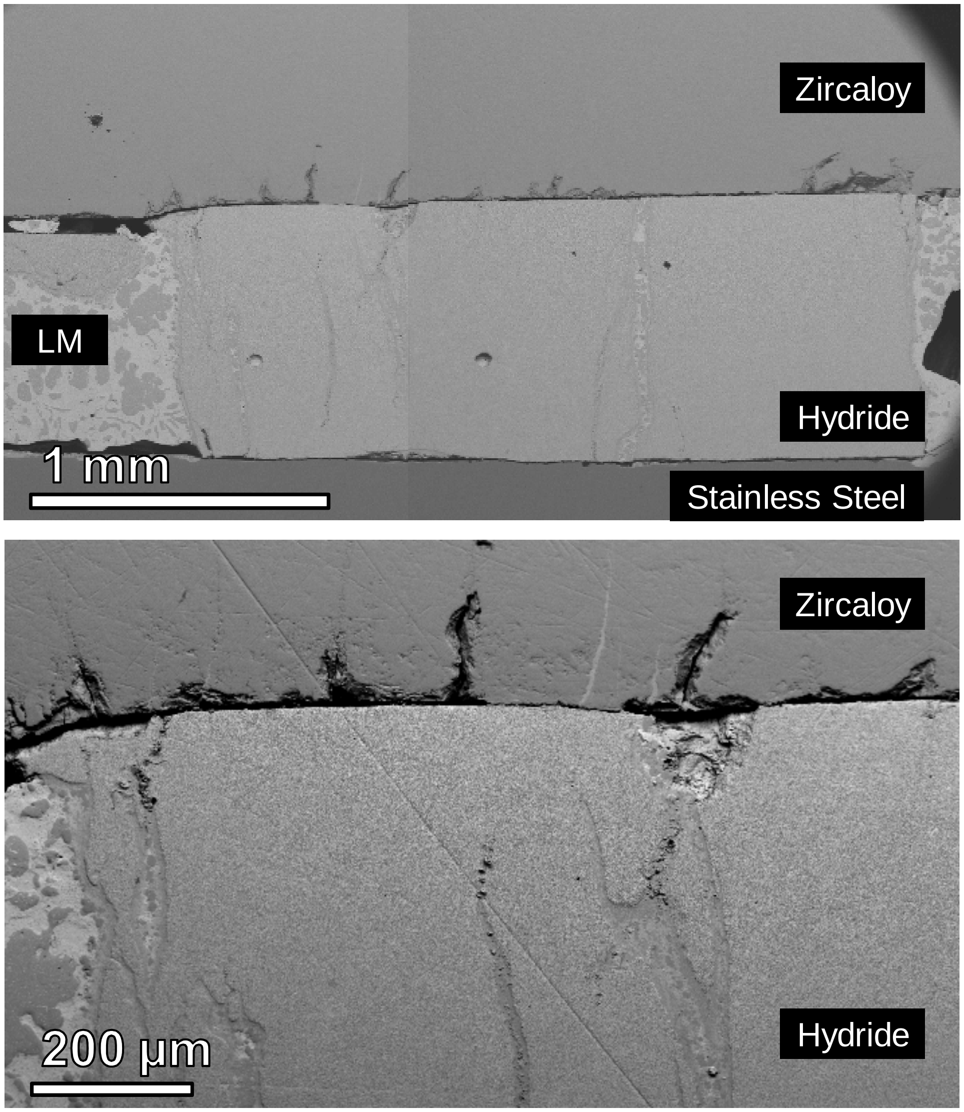

Figure 6.4: Sample 3: Top: hydride-Zircaloy interface (120 MPa contact pressure); Bottom: series of cracks forming in the cladding at the Zircaloy-fuel interface (backscattered electron image).

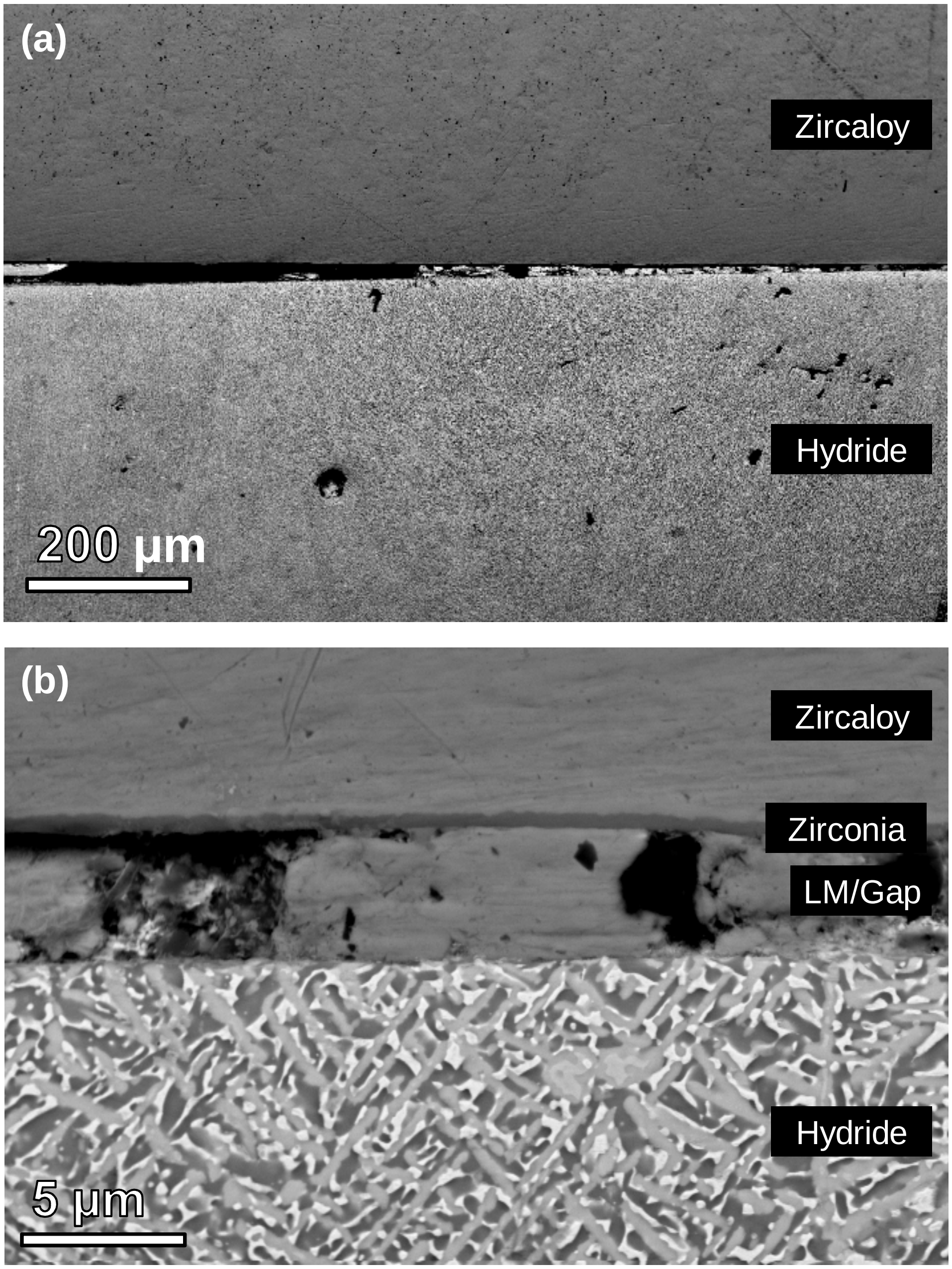

Figure 6.5: Sample 4: Top: hydride-Zircaloy interface; Bottom: Partially-LM-filled gap between the zirconia layer and the hydride fuel (backscattered electron image).

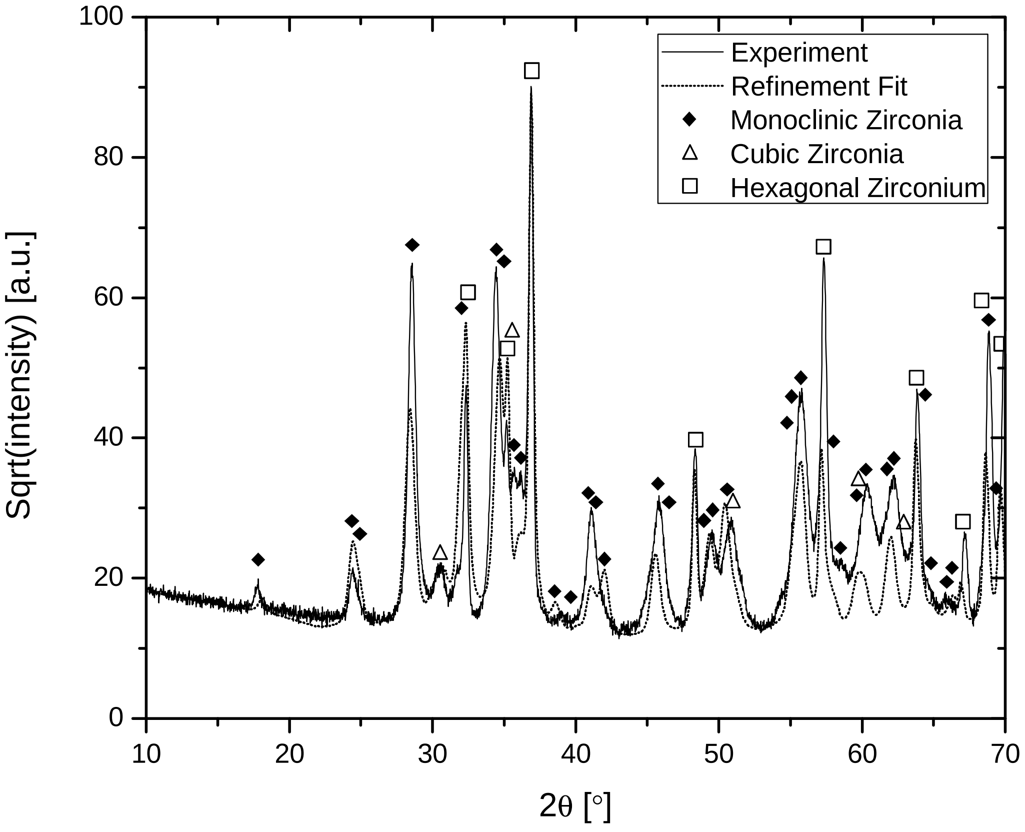

Figure 6.6: X-ray diffraction of oxide grown on the surface of Zircaloy disks at 500 °C for 24 hours under 10 MPa of air pressure along with the Rietveld refinement fit. The difference in the intensity of some of the experimental and calculated peaks for zirconia is possibly due to preferred orientation of the oxide grains.

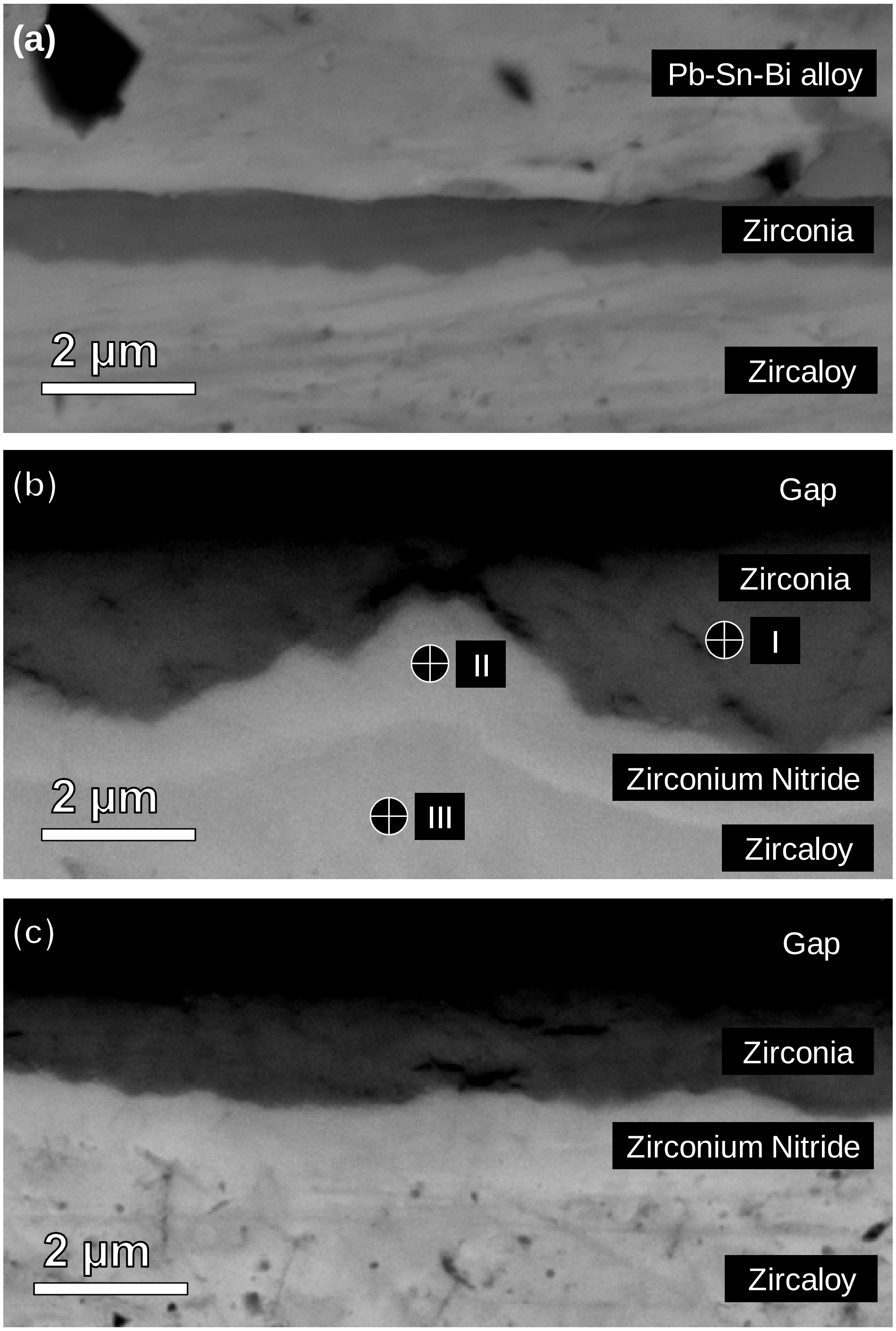

Figure 6.7: Backscattered electron microscopy of the oxide layer grown on the surface of Zircaloy after the compatibility experiments. Top: sample 4; Middle: sample 5; Bottom: sample 6.

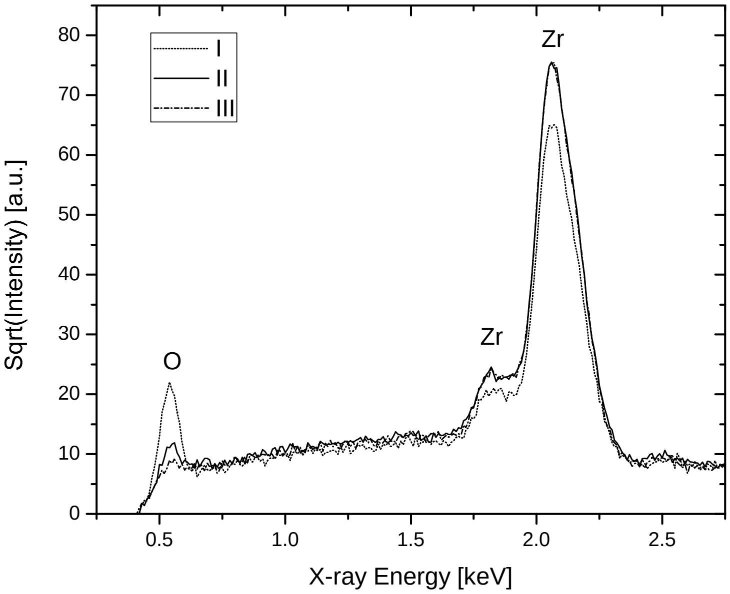

Figure 6.8: Energy dispersive X-ray spectroscopy of areas identified in Figure 6.7(b).

6.4 Conclusions

Liquid metal is a superior gap filler compared to helium gas. It provides much higher thermal conductivity and protects the cladding and fuel from corrosive gaseous fission-product species. The feasibility of utilizing liquid metal as a barrier for hydrogen transport from the fuel to the cladding was investigated over a period of one month at 375 °C (a typical fuel surface temperature during LWR operation). Hydrogen does not form any compounds with any of the constituents of the liquid metal alloy and has limited solubility in these materials. When a LM-filled gap was maintained, hydriding did not occur; either the liquid metal limits the kinetics of hydrogen transport at the fuel-LM interface or through the bulk diffusion process. In cases where contact is made between the hydride and bare Zircaloy, cladding is susceptible to hydriding and subsequent cracking. The interface (between fuel and cladding) contact pressure appears insignificant with respect to its effect on the possibility of Zircaloy hydriding. The presence of a thin, uniform oxide layer, grown on the surface of Zircaloy at high temperatures in air, appears to protect the cladding contacted by hydride fuel from hydriding. To extrapolate the results of this study to predict performance under irradiation requires further detailed investigation. However, this chapter points out that future studies should be focused on compatibility of hydride fuel and oxidized Zircaloy cladding; since clearly cracking in case of bare Zircaloy surface will occur.

Chapter 7

Future Work: Hydride Fuel-Rod Irradiation

As described in Chapter 1 this study has focused on examining the basic materials aspects of the LWR-hydride-fuel concept. The fabrication process and structural characteristics of the hydride fuel have been explained. Some basic materials properties of the hydride fuel (i.e. elastic moduli, hydrogen diffusivity) have been reported, providing the input for fuel modeling codes. Fuel behavior under various operating conditions (necessary for determining the feasibility of hydride fuel incorporation in LWRs) have been examined by modeling. One of the kinetic properties associated with the most pressing accident scenario, hydrogen desorption from the fuel in a temperature transient, has been extensively studied. Mechanisms for kinetic processes have been identified and associated rates have been quantified.

Following the roadmap provided by Crawford et al. [16], the next major phase after concept definition and feasibility is fuel design improvement and evaluation. While the former focuses on characterizing component performance or critical function of the fuel in a laboratory environment, the latter aims to shift these activities to a small-scale fuel-rod irradiation experiment. Therefore the next phase of activities will focus on irradiation under typical LWR operating conditions and post-irradiation examination of the LWR hydride fuel.

7.1 Irradiation experiment

A project was awarded by the Advanced Test Reactor National Scientific User Facility program (U.S. Department of Energy) to support irradiation testing. An irradiation spot was designated in the MIT reactor for fuel insertion, while post-irradiation examination will be conducted at Idaho National Laboratory's Hot Fuel Examination Facility (HFEF).

7.1.1 Instrumented hydride mini-fuel rod assembly

Three instrumented mini-fuel rods will be irradiated at MITR (Figure 7.1). Each mini-fuel rod consists of five uranium-zirconium hydride ($U_{0.17}ZrH_{1.6}$) fuel pellets that are clad in a 75 mm long Zircaloy-2 tube. The pellets will be prepared from a TRIGA fuel element (30wt% U, 19.7% U-235 enrichment) by diamond-bit core drilling and centerless grinding. A distribution of gap sizes will be present between the fuel and the cladding, ranging from 50 to 150 μm. Alumina spacers are placed on the top and bottom of the pellets while the entire stack is submerged in a molten eutectic lead-bismuth alloy (Bi-44wt%Pb) inside the Zircaloy cladding. The Zircaloy tube is capped off on the bottom end with a Zircaloy-2 plug (laser welded), while from the top it is laser welded to a zirconium Con Flat (CF) mini flange. A K-type thermocouple runs through the center of the fuel stack up to the midpoint. The stainless-steel-sheathed thermocouple is attached, by high-temperature brazing, to a stainless-steel CF mini flange that caps

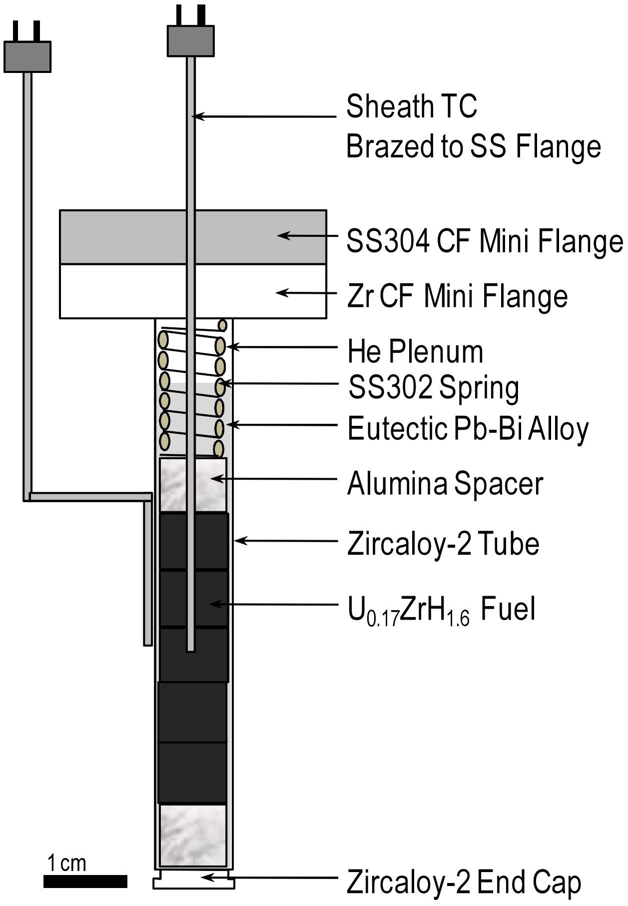

Figure 7.1: Hydride mini-fuel rod assembly for irradiation in the MIT Reactor.

off the mini-fuel rod against the zirconium flange with a copper gasket. A second thermocouple is attached to the surface of the cladding. Continuous measurement of fuel centerline and cladding outer diameter temperatures provides valuable in-pile data on fuel-centerline temperature and thermal conductivity of the fuel as a function of burnup.

7.1.2 Irradiation conditions

Each mini-fuel rod assembly will be placed inside a MITR-supplied titanium capsule that is also filled with eutectic lead-bismuth alloy. The three capsules will then be stacked on top of one another and inserted in the irradiation positions in MITR in contact with the coolant water. The instrumented capsules will be placed in either the A-1 or A-3 positions in the core (Figure 7.2).

A full-core MCNP calculation with the hydride mini-fuel elements inside the irra-

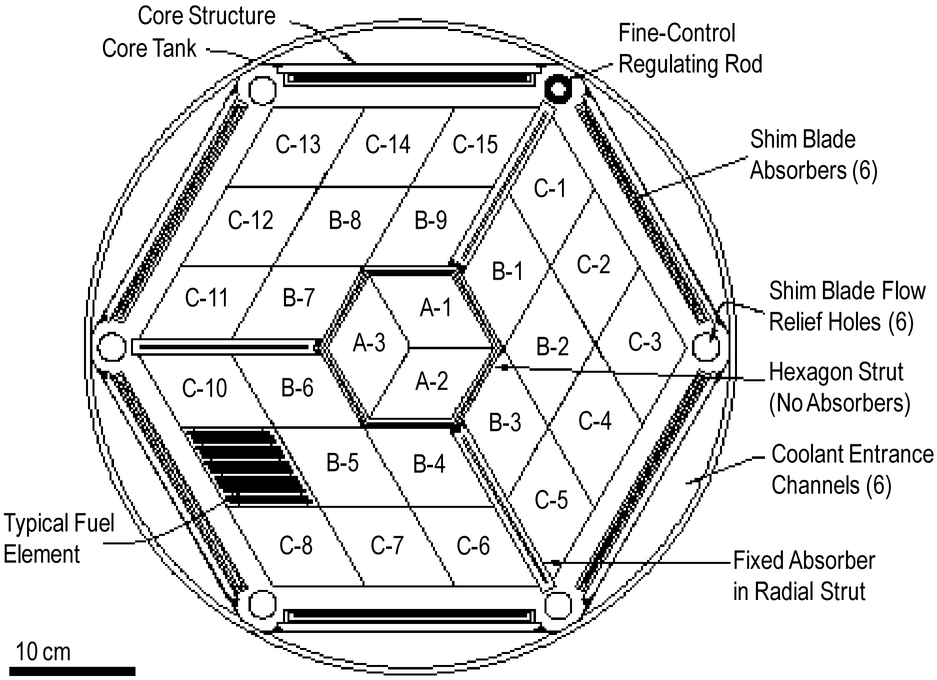

Figure 7.2: Schematic of the MIT reactor core.

diation capsules was performed to estimate the power conditions in the hydride fuel. Both the fast and thermal neutron fluxes inside the fuel are ~1.2×10^{14} cm^2/s (0.1 MeV threshold). The linear heat rates in the upper annular (with centerline TC) and lower solid portions of the fuel stack are 280 and 330 W/cm respectively. Neutron flux spectra inside the fuel are shown in Figure 7.3. The difference in the magnitude of the thermal neutron peak with that shown in Figure 1.6 is due to the variation in U-235 enrichment. The 4-fold higher enrichment of the TRIGA fuel used during this irradiation experiment reduces the thermal flux, since more neutrons are consumed during fission reactions. The power conditions are ultimately ideal for this irradiation experiment and closely replicate power and fuel temperature conditions of the proposed LWR hydride fuel.

7.1.3 Post irradiation examination plans

One mini fuel rod will be removed from the reactor core approximately every 4 months for post-irradiation examination (PIE). The PIE activities shall take place at the HFEF located in INL. Some of the standard procedures during post-irradiation examination at the HFEF that will be utilized on the irradiated specimens are neutron radiography, precision gamma scanning, and dimensional inspection. The extent and type of fission gases released will also be determined during PIE at the HFEF. In addition

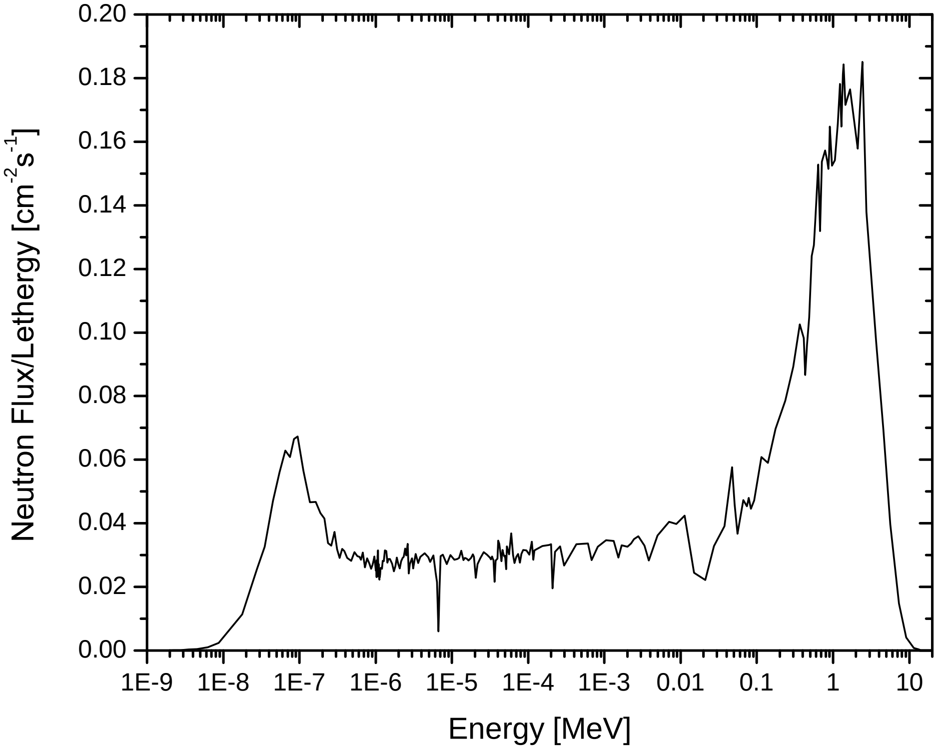

Figure 7.3: Neutron flux spectra inside the hydride fuel pellets during irradiation at MIT Reactor.

the PIE activities will involve many characterization techniques already demonstrated on as fabricated hydride fuels. Transmission and scanning electron microscopy, X-ray diffractometry, mass spectrometry, and atomic force microscopy are some of the techniques that will be utilized during PIE stage.

The extent of fission-gas release from hydride fuels and through the liquid metal alloy will be examined. Redistribution of hydrogen in the fuel and possible hydriding of the Zircaloy cladding will be investigated. It is necessary to understand the dominant mechanism of fuel swelling; whether it is due to solid fission products, fission gas bubbles, and other defects. Also the possibility of gas-bubble formation in the liquid metal bond, which would compromise the high thermal conductivity, will be studied.

7.2 Summary

In order to accommodate the necessary shift from laboratory scale to small and large scale irradiation experiments aimed at studying the feasibility of hydride fuel incorporation in LWRs, three hydride mini-fuel elements are to be irradiated at the MIT research reactor. The three-rod test matrix will provide valuable information on the burnup dependence of the irradiation effects on fuel and cladding. The physical assemblies and power conditions are designed to closely resemble LWR operating conditions.

Bibliography

[1] Data analysis and visualization environment. `http://www.ncnr.nist.gov/dave`.

[2] Energy Information Administration. `http://www.eia.doe.gov/oiaf/ieo/pdf/ieonuclear.pdf`, 2010.

[3] T.A. Badaeva and G.K. Alekseenko. Structure of Alloys of the Thorium-Uranium-Zirconium System. *Struct. Alloys Certain Systems Cont. Uranium Thorium*, page 376, 1963.

[4] N.L. Baldwin, F.C. Foushee, and J.S. Greenwood. Fission Product Release from TRIGA-LEU Reactor Fuels. Technical Report GA-A-16287, General Atomic Co., San Diego, California, Nov 1980.

[5] G. Balooch, G. Marshall, S. Marshall, O. Warren, S. Asif, and M. Balooch. Evaluation of a New Modulus Mapping Technique to Investigate Microstructural Features of Human Teeth. *Journal of Biomechanics*, 37:1223–1232, 2004.

[6] C. Bamford, C. Tipper, and R. Compton. *Comprehensive Chemical Kinetics: Simple Processes at the Gas-Solid Interface*, volume 19. Elsevier science publishers, 1979.

[7] W. Bartscher, A. Boeuf, R. Caciuffo, J. Fournier, W. Kuhs, J. Rebizant, and F. Rustichelli. Neutron Diffraction Study of Beta-UD3 and Beta-UH3. *Solid State Communications*, 53(9):423–426, 1985.

[8] W. Bartscher, J. Rebizant, A. Boeuf, R. Caciuffo, F. Rustichelli, J. Fournier, and W. Kuhs. Distribution of Deuterium in the Cubic Laves Phase ThZr2Dx. *Journal of Less Common Metals*, 121:445, 1986.

[9] W. Bartscher, J. Rebizant, and J.M. Haschke. Equilibria and Thermodynamic Properties of the ThZr2-H System. *Journal of Less Common Metals*, 136:385, 1988.

[10] R. Beck. Zirconium-Hydrogen Phase System. *Trans. Am. Soc. Metals*, 55:542, 1962.

[11] M.M. Bretscher. Transition From HEU to LEU fuel in Romania's 14-MW TRIGA Reactor. Technical Report ANL/CP-74817, Argonne National Laboratory, Argonne, IL, Jan 1991.

[12] R. Chesworth. Final results of qualification testing of triga fuel. In *International Meeting On Reduced Enrichment for Research and Test Reactors*, Petten, The Netherlands, Oct 1985.

[13] C.T. Chudley and R.J. Elliott. Neutron scattering from a liquid on a jump diffusion model. *Proceedings of the Physical Society*, 77:353, 1961.

[14] Nuclear Regulatory Commission. `http://www.data.gov/raw/1359`, 2010.

[15] J. Crank and P. Nicolson. A Practical Method for Numerical Evaluation of Solutions of Partial Differential Equations of the Heat Conduction Type. *Proceedings of the Cambridge Philosophical Society*, 43:50–64, 1947.

[16] D.C. Crawford, D.L. Porter, S.L. Hayes, M.K. Meyer, D.A. Petti, and K. Pasamehmetoglu. An approach to Fuel Development and Qualification. *Journal of Nuclear Materials*, 371:232, 2007.

[17] Smith et al. TRG Report. Technical Report ICDD, Penn State University, 1973.

[18] I. Ferguson. TRG Report. Technical Report 2438-1, United Kingdom Atomic Energy Assoc, 1976.

[19] D.P. DeWitt F.P. Incropera. *Fundamentals of Heat and Mass Transfer*. John Wiley and Sons Inc., 5th edition, 2002.

[20] M. Fratoni and E. Greenspan. Neutronic design of hydride fueled BWRs. *Nuclear Engineering and Design*, 239:1531–1543, 2009.

[21] D.R. Fredrickson, R.L. Nuttall, H.E. Flotow, and W.N. Hubbard. The enthalpies of formation of zirconium dihydride and zirconium dideuteride. *Journal of Physical Chemistry*, 67:1506, 1963.

[22] B. Fultz and J. M. Howe. *Transmission Electron Microscopy and Diffractometry of Materials*. Springer, 2nd edition, 2002.

[23] F. Ganda and E. Greenspan. Plutonium and Minor Actinides Multi-Recycling in PWR Using Hydride Fuels. In *International Conference on Reactor Physics, PHYSOR08*, Interlaken, Switzerland, Sep 2008.

[24] F. Ganda and E. Greenspan. Plutonium Recycling in Hydride Fueled PWR Cores. *Nuclear Engineering and Design*, 239:1489–1504, 2009.

[25] I. Grenthe, J. Fuger, R. Konings, R. Lemire, A. Muller, C. Nguyen-Trung, and H. Wanner. *Chemical Thermodynamics of Uranium*. OECD Publications, Paris, France, 2004.

[26] D.M. Gutowski. Kinetics of hydrogen uptake and release from zirconium hydride. Master's thesis, University of California, Berkeley, 2004.

[27] J.D. Gylfe, H. Rood, J. Greenleaf, K. Balkwill, L. Prem, and L. Goldfisher. Evaluation of zirconium hydride as moderator in integral boiling water super heat reactors. Technical Report NAA-SR-5943, Atomics International. Div. of North American Aviation, Inc., Canoga Park, California, Mar 1962.

[28] ASM Handbooks. *Properties and Selection: Nonferrous Alloys and Special-Purpose Materials*, volume 2. ASM, 2008.

[29] R. Hempelmann. *Quasielastic Neutron Scattering and Solid State Diffusion*. Oxford University Press Inc., 2008.

[30] J. Huang, B. Tsuchiya, K. Konashi, and M. Yamawaki. Estimation of Hydrogen Redistribution in Zirconium Hydride under Temperature Gradient. *Journal of Nuclear Science and Technology*, 37:887–892, 2000.

[31] Nuclear Energy Institute. `http://www.nei.org/resourcesandstats/nuclear_statistics`, 2010.

[32] Full issue. Hydride Fueled LWRs. *Nuclear Engineering and Design*, 239:1373–1570, 2009.

[33] W. James and M. Straumanis. Lattice Parameter and Coefficient of Thermal Expansion of Thorium. *Acta Crystallographica*, 9:376, 1956.

[34] D.A. King, T. Madey, and J.T. Yates. Interaction of Oxygen with Polycrystalline Tungsten. II. Corrosive Oxidation. *Journal of Chemical Physics*, 55:3247, 1971.

[35] M. Kuroda, D. Setoyama, M. Uno, and S. Yamanaka. Nanoindentation Studies of Zirconium Hydride. *Journal of Alloys and Compounds*, 368:211–214, 2004.

[36] I. Langmuir. The adsorption of gases on plane surfaces of glass, mica and platinum. *Journal of the American Chemical Society*, 40:1361, 1918.

[37] A.D. LeClaire. An assessment of measurements of the steady-state permeability of H and its isotopes through Fe, Fe-based alloys, and some commercial steels. *Defect Diffus. Forum*, 34:1, 1983.

[38] A.F. Lillie, D.T. Mcclelland, W.J. Roberts, and J.H. Walter. Zirconium Hydride Fuel Element Performance Characteristics. Technical Report AI-AEC-13084, Atomics International. Div. of North American Aviation, Inc., Canoga Park, California, Jun 1973.

[39] G. Majer, W. Renz, and R. Barnes. The Mechanism of Hydrogen Diffusion in Zirconium Dihydrides. *Journal of Physics: Condensed Matter*, 6:2935–2942, 1994.

[40] M. W. Mallett and I. E. Campbell. The Dissociation Pressure of Thorium Dihydride in the Thorium-Thorium Dihydride System. *Journal of the American Chemical Society*, 73:4850–4852, 1951.

[41] E. Mamontov, M. Zamponi, S. Hammons, W.S. Keener, M. Hagen, and K.W. Herwig. BASIS: A New Backscattering Spectrometer at the SNS. *Neutron News*, 19:22, 2008.

[42] C. San Marchi, B. Somerday, and S. Robinson. Permeability, solubility and diffusivity of hydrogen isotopes in stainless steels at high gas pressures. *International Journal of Hydrogen Energy*, 32:100, 2007.

[43] P.J. Meier. *Life-cycle assessment of electricity generation systems and applications for climate change policy analysis*. PhD thesis, Institute Fusion Technology, University of Wisconsin Madison, 2002.

[44] C.J.M. Northrup. The Hydrogen-Uranium System. *Journal of Physical Chemistry*, 79:726–731, 1975.

[45] H. Okamoto. *Th-Zr (Thorium-Zirconium), Binary Alloy Phase Diagrams, T.B. Massalski (ed)*, volume 3. ASM, 2nd edition, 1990.

[46] D.R. Olander. Fundamental aspects of nuclear reactor fuel elements. Technical Report TID-26711-P1, University of California, Berkeley. Dept. of Nuclear Engineering, Berkeley, California, Jan 1976.

[47] D.R. Olander, E. Greenspan, H.D. Garkischb, and B. Petrovic. Uranium-Zirconium Hydride Fuel Properties. *Nuclear Engineering and Design*, 239:1406–1424, 2009.

[48] D.R. Olander and M. Ng. Hydride Fuel Behavior in LWRs. *Journal of Nuclear Materials*, 346:98–108, 2005.

[49] W.C. Oliver and G.M. Pharr. An improved technique for determining hardness and elastic modulus using load and displacement sensing indentation experiments. *Journal of Materials Research*, 7:1564, 1992.

[50] T.J. Parker. Process Development and Fabrication of Zirconium Hydride Hastelloy X Clad Fuel Elements. Technical Report AI-AEC-13082, Atomics International. Div. of North American Aviation, Inc., Canoga Park, California, Jun 1973.

[51] A. Patterson. Beyond one and done. *Nuclear Engineering International*, pages 38–40, May 2009.

[52] J.H. Rust. *Nuclear Power Plant Engineering*. Haralson Publishing Company, Buchanan, GA, 1979.

[53] M.R. Shanabarger. Absolute desorption rate measurements for H2 chemisorbed on nickel. *Solid State Communications*, 14:1015, 1974.

[54] M.R. Shanabarger. The isothermal kinetics of hydrogen adsorption onto iron films observed with the chemisorption-induced resistance change. *Surface Science*, 150:451, 1985.

[55] D.P. Shoemaker and C.B. Shoemaker. Concerning atomic sites and capacities for hydrogen absorption in the AB2 Friauf-Laves phases. *Journal of LessCommon Metals*, 68:43, 1979.

[56] M.T. Simnad. TheU-ZrHx Alloy: Its Properties and Use in TRIGA Fuel. *Nuclear Engineering and Design*, 64:403, 1981.

[57] L. Simpson and C. Cann. Fracture Toughness of Zirconium Hydride and Its Influence on The Crack Resistance of Zirconium Alloys. *Journal of Nuclear Materials*, 87:303–316, 1979.

[58] A.W. Sommer and W.F. Dennison. Thermal Diffusion Of Hydrogen In Nonstoichiometric Zirconium-Dihydride. Technical Report NAA-SR-5066, Atomics International. Div. of North American Aviation, Inc., Canoga Park, California, Oct 1960.

[59] J. Spino, A.D. Stalios, H. Santa Cruz, and D. Baron. Stereological evolution of the rim structure in PWR-fuels at prolonged irradiation: Dependencies with burn-up and temperature. *Journal of Nuclear Materials*, 354:66–84, 2006.

[60] M. Steinbruck. Prototypical experiments relating to air oxidation of Zircaloy-4 at high temperatures. *Journal of Nuclear Materials*, 392:531, 2009.

[61] Sturken. Post. *Acta Crystallographica*, 13:852, 1960.

[62] X. Sun, J. Xu, and Y. Li. Hydrogen permeation Behavior in Austenitic Stainless Steels. *Materials Science and Engineering*, A11:179, 1989.

[63] A.C. Switendick. *Z. Phys. Chem., Neue Folge*, 117:89, 1979.

[64] Y. Takahashi, M. Yamawaki, and K. Yamamoto. Thermophysical Properties of Uranium-Zirconium Alloy. *Journal of Nuclear Materials*, 154:141–144, 1988.

[65] K.A. Terrani, M. Balooch, D.R. Olander, and W. Siekhaus. Liquid Metal as a Gap Filler to Protect Zircaloy Cladding from Hydride Fuel. In *Proceedings of Top Fuel 2009*, Paris, France, Sep 2009.

[66] K.A. Terrani, J.E. Seifried, and D.R. Olander. Transient Hydride Fuel Behavior in LWRs. *Journal of Nuclear Materials*, 392:192–199, 2009.

[67] K.A. Terrani, G.W. Chinthaka Silva, C.B. Yeamans, M. Balooch, and D.R. Olander. Fabrication and Characterization of Uranium-Thorium-Zirconium Hydrides. *Journal of Nuclear Materials*, 392:151–157, 2009.

[68] B. Tsuchiya, J. Huang, K. Konashi, W. Saiki, T. Onoue, and M. Yamawaki. Thermal diffusivity measurement of uranium-thorium-zirconium hydride. *Journal of Alloys and Compounds*, 312:104–110, 2000.

[69] J.A. Venables and M. Bienfait. On the reaction order in thermal desorption spectroscopy. *Surface Science*, 61:667, 1976.

[70] W. Wang and D.R. Olander. Thermodynamics of the Zr-H System. *Journal of American Ceramic Society*, 78:3323, 1995.

[71] E. Wicke and K. Otto. The Uranium Hydrogen System and the Kinetics of Hydride Formation. *Z. Phys. Chem. Neue Folge*, 31:222–248, 1962.

[72] W. Wiesenack, M. Vankeerberghen, and R. Thankappan. Assessment of UO2 Conductivity Degradation Based on In-Pile Temperature Data. Technical Report HWR-469, OECD Halden Reactor Project, Halden, Norway, Apr 1996.

[73] D. Wongsawaeng and D.R. Olander. A Liquid-Metal Bond for Improved LWR Fuel Performance. *Nuclear Technology*, 159:279, 2007.

[74] T. Yamamoto, H. Suwarno, H. Kayano, and M. Yamawaki. Development of New Reactor Fuel Materials: Hydrogenation Properties of U-Th-Zr Alloys and Neutron Irradiation Effects on their Hydrides. *Journal of Nuclear Materials*, 247:339–344, 1997.

[75] T. Yamamoto, H. Suwarno, F. Ono, H. Kayano, and M. Yamawaki. Preparation, analysis and irradiation of hydride U-Th-Zr alloy samples for a new fuel. *Journal of Alloys Compounds*, 271-273:702–706, 1998.

[76] S. Yamanaka, K. Yamada, K. Kurosaki, M. Uno, K. Takeda, H. Anada, T. Matsuda, and S. Kobayashi. Thermal Properties of Zirconium Hydride. *Journal of Nuclear Materials*, 294:94–98, 2001.

[77] S. Yamanaka, K. Yamada, K. Kurosaki, M. Uno, K. Takeda, H. Anada, T. Matsuda, and S. Kobayashi. Characteristics of Zirconium Hydride and Deuteride. *Journal of Alloys Compounds*, 330-332:99–104, 2002.

[78] S. Yamanaka, K. Yoshioka, M. Uno, M. Katsura, H. Anada, T. Matsuda, and S. Kobayashi. Thermal and Mechanical Properties of Zirconium Hydride. *Journal of Alloys and Compounds*, 293-295:23–29, 1999.

[79] M. Yamawaki, H. Suwarno, T. Yamamoto, T. Sanda, K. Fujimura, K. Kawashima, and K. Konashi. Concept of hydride fuel target subassemblies in a fast reactor core for effective transmutation of MA. *Journal of Alloys Compounds*, 271-273:530, 1998.

[80] J.M. Zuo and J.C. Mabon. Web-based electron microscopy application software: Web-emaps. `http://emaps.mrl.uiuc.edu/`, 2004.

Appendix A

MCNP Analysis

The power distribution across the uranium-zirconium hydride ($U_{0.31}ZrH_{1.6}$) fuel is unknown and it is intended to determine the steady state power profile during the reactor operation. The power profile determines the distribution of temperature across the cylindrical pellet. Temperature gradients across the fuel in turn affects the chemical potential gradient for hydrogen migration and redistribution due to the Soret effect (Chapter 3). Therefore the concentration of hydrogen and overall density of the material across the fuel is susceptible to change under steady state conditions. However the effect of hydrogen redistribution, temperature gradient and density change across the fuel are minimal on power distribution across the fuel pellet as discussed in Section 3.3.3; although they have been taken into account.

The fuel pellet is assumed to be 1 cm in diameter placed inside Zircaloy cladding of 0.09 cm thickness with a 70 μm liquid-metal-filled gap in between. The fuel consists of metallic uranium particles dispersed in a matrix of δ-zirconium hydride. The volume fraction of uranium in the fuel is dependent on the hydrogen concentration in the hydride phase however and average value of 19% is an accurate approximation. 5% U-235 enrichment is assumed for the uranium. The liquid metal consists of a ternary alloy of lead-tin-bismuth (Pb-33wt%Sn-33wt%Bi). The pitch-to-diameter ratio of the fuel assembly is assumed to be fixed at the value of 1.2.

The steady state temperature and hydrogen concentration profiles for the uranium-zirconium hydride fuel operated at linear heat rate of 300W/cm are shown in Figure 3.3. The lattice parameter of δ-zirconium hydride phase varies as function of hydrogen to zirconium ratio as shown in Equation A.1 [77].

$$a\,[\text{nm}] = 0.4706 + 0.004382C \tag{A.1}$$

where C is the hydrogen-to-zirconium ratio. The variation in the expansion of lattice parameter due to the temperature gradient is neglected. Using this information an MCNP code is generated with the fuel divided into 10 radial shells of constant thickness. Appropriate temperature, density, and cross sections tables are specified for each shell. The cell is assumed to have reflective boundary conditions. The power (F6) and flux (F4) are tallied in each shell with a fine energy bin distribution defined for the latter. In order to generate results with adequate statistical significance the code is set up to run 3000 histories each containing 3000 neutrons. The standard deviation of the power in the innermost shell is largest since it has the smallest volume. Standard deviation of the results varies as the inverse square root of number of runs. The MCNP code is included as follows:

```
SINGLE PIN
c Cells
1 1 -8.2399 -1 -20 30 vol=3.142 tmp=7.30e-8 imp:n=1
2 2 -8.2397 -2 1 -20 30 vol=9.425 tmp=7.28e-8 imp:n=1
3 3 -8.2393 -3 2 -20 30 vol=15.708 tmp=7.23e-8 imp:n=1
4 4 -8.2387 -4 3 -20 30 vol=21.991 tmp=7.16e-8 imp:n=1
5 5 -8.2378 -5 4 -20 30 vol=28.274 tmp=7.07e-8 imp:n=1
6 6 -8.2367 -6 5 -20 30 vol=34.558 tmp=6.96e-8 imp:n=1
7 7 -8.2354 -7 6 -20 30 vol=40.841 tmp=6.83e-8 imp:n=1
8 8 -8.2337 -8 7 -20 30 vol=47.124 tmp=6.68e-8 imp:n=1
9 9 -8.2318 -9 8 -20 30 vol=53.407 tmp=6.52e-8 imp:n=1
```

```
    10 10 -8.2296 -10 9 -20 30 vol=59.690 tmp=6.34e-8 imp:n=1
    11 11 -8.2 -11 10 -20 30 vol=8.858 tmp=6.11e-8 imp:n=1 $gap
    12 12 -6.56 -12 11 -20 30 vol=124.859 tmp=5.88e-8 imp:n=1 $clad
    13 13 -0.7092 -13 14 -40 50 12 -20 30 vol=373.2896 tmp=4.95e-8 imp:n=1 $water
    14 0 13:-14:40:-50:20:-30 imp:n=0 $void
    c Surfaces
    1 cz 0.05 $fuel shell 1
    2 cz 0.1 $fuel shell 2
    3 cz 0.15 $fuel shell 3
    4 cz 0.2 $fuel shell 4
    5 cz 0.25 $fuel shell 5
    6 cz 0.3 $fuel shell 6
    7 cz 0.35 $fuel shell 7
    8 cz 0.4 $fuel shell 8
    9 cz 0.45 $fuel shell 9
    10 cz 0.5 $fuel shell 10
    11 cz 0.507 $gap
    12 cz 0.597 $clad
    13 px 0.7164 $right of water box
    14 px -0.7164 $left of water box
    40 py 0.7164 $ top of water box
    50 py -0.7164 $ bottom of water box
    20 pz 200 $top of pin
    30 pz -200 $bottom of pin
    c Data
    m1 40000.12c 1.0 92235.85c 0.0155 92238.85c 0.2945 1001.12c 1.5061 $fuel shell 1
    m2 40000.12c 1.0 92235.85c 0.0155 92238.85c 0.2945 1001.12c 1.5097 $fuel shell 2
    m3 40000.12c 1.0 92235.85c 0.0155 92238.85c 0.2945 1001.12c 1.5171 $fuel shell 3
    m4 40000.12c 1.0 92235.85c 0.0155 92238.85c 0.2945 1001.12c 1.5281 $fuel shell 4
    m5 40000.12c 1.0 92235.32c 0.0155 92238.32c 0.2945 1001.12c 1.5432 $fuel shell 5
    m6 40000.12c 1.0 92235.32c 0.0155 92238.32c 0.2945 1001.12c 1.5625 $fuel shell 6
    m7 40000.12c 1.0 92235.15c 0.0155 92238.15c 0.2945 1001.12c 1.5863 $fuel shell 7
    m8 40000.12c 1.0 92235.15c 0.0155 92238.15c 0.2945 1001.12c 1.6150 $fuel shell 8
    m9 40000.11c 1.0 92235.84c 0.0155 92238.84c 0.2945 1001.11c 1.6489 $fuel shell 9
    m10 40000.11c 1.0 92235.84c 0.0155 92238.84c 0.2945 1001.11c 1.6881 $fuel shell 10
    m11 82000.42c 1.0 50000.65c 1.0 83209.65c 1.0 $gap fill
    m12 40000.11c 1.0 $clad
    m13 1001.72c 2 8016.74c 1 $water
    prdmp 3000 3000 3000
    KCODE 3000 1 100 3000
    KSRC 0 0 0 MODE n PRINT
    F6:n 1 2 3 4 5 6 7 8 9 10
    F4:n 1 2 3 4 5 6 7 8 9 10
    e4 1.0000E-11 1.0000E-10 5.0000E-10 7.5000E-10 1.0000E-09 1.2000E-09 1.5000E-09 2.0000E-09 2.5000E-09 3.0000E-09 4.0000E-09 5.0000E-09 7.5000E-09 1.0000E-08 2.5300E-
08 3.0000E-08 4.0000E-08 5.0000E-08 6.0000E-08 7.0000E-08 8.0000E-08 9.0000E-08 1.0000E-07 1.2500E-07 1.5000E-07 1.7500E-07 2.0000E-07 2.2500E-07 2.5000E-07 2.7500E-07
3.0000E-07 3.2500E-07 3.5000E-07 3.7500E-07 4.0000E-07 4.5000E-07 5.0000E-07 5.5000E-07 6.0000E-07 6.2500E-07 6.5000E-07 7.0000E-07 7.5000E-07 8.0000E-07 8.5000E-07
9.0000E-07 9.2500E-07 9.5000E-07 9.7500E-07 1.0000E-06 1.0100E-06 1.0200E-06 1.0300E-06 1.0400E-06 1.0500E-06 1.0600E-06 1.0700E-06 1.0800E-06 1.0900E-06 1.1000E-06
1.1100E-06 1.1200E-06 1.1300E-06 1.1400E-06 1.1500E-06 1.1750E-06 1.2000E-06 1.2250E-06 1.2500E-06 1.3000E-06 1.3500E-06 1.4000E-06 1.4500E-06 1.5000E-06 1.5900E-06
1.6800E-06 1.7700E-06 1.8600E-06 1.9400E-06 2.0000E-06 2.1200E-06 2.2100E-06 2.3000E-06 2.3800E-06 2.4700E-06 2.5700E-06 2.6700E-06 2.7700E-06 2.8700E-06 2.9700E-06
3.0000E-06 3.0500E-06 3.1500E-06 3.5000E-06 3.7300E-06 4.0000E-06 4.7500E-06 5.0000E-06 5.4000E-06 6.0000E-06 6.2500E-06 6.5000E-06 6.7500E-06 7.0000E-06 7.1500E-06
8.1000E-06 9.1000E-06 1.0000E-05 1.1500E-05 1.1900E-05 1.2900E-05 1.3750E-05 1.4400E-05 1.5100E-05 1.6000E-05 1.7000E-05 1.8500E-05 1.9000E-05 2.0000E-05 2.1000E-05
2.2500E-05 2.5000E-05 2.7500E-05 3.0000E-05 3.1250E-05 3.1750E-05 3.3250E-05 3.3750E-05 3.4600E-05 3.5500E-05 3.7000E-05 3.8000E-05 3.9100E-05 3.9600E-05 4.1000E-05
4.2400E-05 4.4000E-05 4.5200E-05 4.7000E-05 4.8300E-05 4.9200E-05 5.0600E-05 5.2000E-05 5.3400E-05 5.9000E-05 6.1000E-05 6.5000E-05 6.7500E-05 7.2000E-05 7.6000E-05
8.0000E-05 8.2000E-05 9.0000E-05 1.0000E-04 1.0800E-04 1.1500E-04 1.1900E-04 1.2200E-04 1.8600E-04 1.9250E-04 2.0750E-04 2.1000E-04 2.4000E-04 2.8500E-04 3.0500E-04
5.5000E-04 6.7000E-04 6.8300E-04 9.5000E-04 1.1500E-03 1.5000E-03 1.5500E-03 1.8000E-03 2.2000E-03 2.2900E-03 2.5800E-03 3.0000E-03 3.7400E-03 3.9000E-03 6.0000E-03
8.0300E-03 9.5000E-03 1.3000E-02 1.7000E-02 2.5000E-02 3.0000E-02 4.5000E-02 5.0000E-02 5.2000E-02 6.0000E-02 7.3000E-02 7.5000E-02 8.2000E-02 8.5000E-02 1.0000E-01
1.2830E-01 1.5000E-01 2.0000E-01 2.7000E-01 3.3000E-01 4.0000E-01 4.2000E-01 4.4000E-01 4.7000E-01 4.9952E-01 5.5000E-01 5.7300E-01 6.0000E-01 6.7000E-01 6.7900E-01
7.5000E-01 8.2000E-01 8.6110E-01 8.7500E-01 9.0000E-01 9.2000E-01 1.0100E+00 1.1000E+00 1.2000E+00 1.2500E+00 1.3170E+00 1.3560E+00 1.4000E+00 1.5000E+00 1.8500E+00
2.3540E+00 2.4790E+00 3.0000E+00 4.3040E+00 4.8000E+00 6.4340E+00 8.1873E+00 1.0000E+01 1.2840E+01 1.3840E+01 1.4550E+01 1.5683E+01 1.7333E+01 2.0000E+01
```